Investigating Mechanotransduction and Mechanosensitivity in Mammalian Cells

Zeinab Al-Rekabi

A dissertation submitted to the Faculty of Graduate and
Postdoctoral Studies in partial fulfillment of the requirement for the
degree of Doctor of Philosophy in Physics.

Ottawa-Carleton Institute for Physics
Department of Physics
Faculty of Science
Ottawa, Canada

Table of Contents

Chapter Five: Microtubules Mediate Changes in Membrane Cortical Elasticity during Contractile Activation……………………………….……………………………….…69

Chapter Six: Mechanotransduction Inhibited in the Presence of Nanoforce Application during Contractile Activation………..………………………..…………………..……89

List of Figures

Abbreviations

AFM	atomic force microscope/microscopy
ATP	adenosine triphosphate
BEM	boundary element method
CCD	charge-coupled device
CTF	cellular traction force
DMEM	Dulbecco's Modified Eagle's Medium
DMSO	dimeythlsulfoxide
DNA	deoxyribonucleic acid
EDTA	ethylenediaminetetraacetic acid
ECM	extracellular matrix
E	elasticity (Young's Modulus)
FA	focal adhesion
FAK	focal adhesion kinase
FBS	fetal bovine serum
fs	femtosecond
FTTC	fourier transform traction cytometry
G-actin	monomeric actin
GE	gelatin
GFP	green fluorescence protein
GTP	guanosine triphosphate
GXG	glutaraldehyde crosslinked gelatin
hMSC	human mesenchymal stem cell
HS	horse serum
kDa	kiloDalton
kPa	kilopascal
LSCM	laser scanning confocal microscopy/microscopy
μm	micrometer
μM	micromole/micromolar

mDia1	diaphanous-related formin-1
mm	milimeter
MME	mechanical microenvironment
MT	microtubule
MyoII	myosin-II
NA	numerical aperature
nm	nanometer
nN	nanoNewton
ns	nanosecond
Pa	Pascal
PA	polyacrylamide
PBS	phosphate-buffer saline
PI	proportional-integral
PMT	photomultiplier tube
ps	picosecond
PSF	point spread function
RhoA	ras homolog gene family, member A
ROCK	Rho-associated protein kinase
SEM	standard error of the mean
SD	standard deviation
SF	stress fiber
STM	scanning tunnelling microscope
TEM	transmission electron microscopy
TF	traction force
TFM	traction force microscopy

Abstract

Living organisms are made up of a multitude of individual cells that are surrounded by biomolecules and fluids. It is well known that cells are highly regulated by biochemical signals; however it is now becoming clear that cells are also influenced by the mechanical forces and mechanical properties of the local microenvironment. Extracellular forces causing cellular deformation can originate from many sources, such as fluid shear stresses arising from interstitial or blood flow, mechanical stretching during breathing or compression during muscle contraction. Cells are able to sense variations in the mechanical properties (elasticity) of their microenvironment by actively probing their surroundings by utilizing specialized proteins that are involved in sensing and transmitting mechanical information. The actin cytoskeleton and myosin-II motor proteins form a contractile (actomyosin) network inside the cell that is connected to the extracellular microenvironment through focal adhesion and integrin sites. The transmission of internal actomyosin strain to the microenvironment via focal adhesion sites generates mechanical traction forces. Importantly, cells generate traction forces in response to extracellular forces and also to activily probe the elasticity of the microenvironment. Many studies have demonstrated that extracellular forces can lead to rapid cytoskeletal remodeling, focal adhesion regulation, and intracellular signalling which can alter traction force dynamics. As well, cell migration, proliferation and stem cell fate are regulated by the ability of cells to sense the elasticity of their microenvironment through the generation of traction forces. *In vitro* studies have largely explored the influence of substrate elasticity and extracellular forces in isolation, however, *in vivo* cells are exposed to both mechanical cues simultaneously and their combined effect remains largely unexplored. Therefore, a series of experiments were performed in which cells were subjected to controlled extracellular forces as on substrates of increasing elasticity. The cellular response was quantified by measuring the resulting traction force magnitude dynamics. Two cell types were shown to increase their traction forces in response to extracellular forces only on substrates of specific elasticities. Therefore, cellular traction forces are regulated by an ability to sense and integrate at least two pieces of mechanical information - elasticity and deformation. Finally, this ability is shown to be dependent on the microtubule network and regulators of myosin-II activity.

Acknowledgements

I would like to thank Dr. Pelling and Dr. Harden for their support during these years. I am grateful for their trust and stimulating conversations. I would also like to thank Bela Joos, who is simply a delight to communicate with.

I would like to thank all the members of both the Pelling and Harden Lab. I am very grateful of being surrounded by such a lively and friendly group of people.

I would like to thank my parents and brothers (Ali and Yak) for their everlasting encouragement and motivation, without them I am nothing. To my extended family: Amu Sheikh, Amu Bu Riyadh, et al., shukran for all your support and stimulating conversations. I love you all so dearly.

I cannot forget some of the wonderful people that I met during my stay in Ottawa, Toronto and Montreal: especially Iss Anthro Tree Hugger, Sarsar MD Psycho and Amiracle OBGYN. I am very happy to have met such wonderful people…wallah kul wa7da minchan 3ndha makana khassa eb galbi.

I also would like to thank the NSERC-CREATE program for the financial support.

Lastly, I would like to give credit to this grand universe. I started out in high-school eager to understand it; however I came out only puzzled. I went into University and studied Physics in order to attempt to understand my puzzlement yet I came out even more puzzled and finally I finished my doctorate degree in Physics and I came out even dumber than before. One day I will inherit you, I guess this is not my day……

۞ إلى سويداء العين، ابي و أمي ۞

To my Eyes, Abi and Ummi

Statement of Originality

This thesis contains three major works that were carried out in the Department of Physics at the University of Ottawa between the summer of 2009 and the summer of 2013. Chapter four, five and six are the subject of papers submitted for publication.

Except where acknowledged otherwise, the work presented in this thesis is my own. I thank Dr. Pelling and Dr. Harden for their editorial assistance.

List of Publications and Presentations

Publications

Journal Articles

1. Wan F, Fischer S, Dick S, **Al-Rekabi Z**, Pelling AE, and Harden JL. Biomimetic Surface Coating from Modular Amphiphilic Proteins. *Biomaterials*. In preparation.
2. Modulevsky D, Lefebvre C, **Al-Rekabi Z**, Cuerrier C, Haase K and Pelling AE. Apple Derived Cellulose Scaffolds for 3D Mammalian Cell Culture. *Plos One*. Under Review (2013). Submission Number: PONE-D-13-47794
3. **Al-Rekabi Z,** Haase K and Pelling AE. Microtubules mediate changes in membrane nanomechanics during contractile activation. *Experimental Cell Research*. 1st Revision (2013). Submission Number: ECR-13-506.
4. **Al-Rekabi Z** and Pelling AE. Cross Talk Between Nanoscale Forces and Substrate Nanomechanics Influence Cellular Traction Dynamics. *Phys. Biol*. **10**, 066003 (2013).
5. Baset F, Popov K, Villafranca A, Guay J-M, **Al-Rekabi Z**, Pelling AE, Ramunno L and Bhardwaj R. "Femtosecond laser induced surface swelling in poly-methyl methacrylate." *Optics Exp.* **21**, 12527 (2013).

Book Chapters

1. **Al-Rekabi Z**, Tremblay D, Haase K, Leask RL, Pelling AE. Computational and Experimental Approaches to Cellular and Subcellular Tracking at the Nanoscale. Musa, S.M. ed. *Computational Nanotechnology: Modeling and Applications with MATLAB.* New York: CRC Press, pp.333-361 (2011).
2. **Al-Rekabi Z**, Harden, JL, Pelling AE. Cellular Nanomechanics in Nanomedicine. In Bartul, Z. & Trenor, J. eds. *Advances in Nanotechnology Volume 2*. New York: Nova Science Publishers, pp.275-296 (2010).

Conferences

Talks

1. **Al-Rekabi Z** & Pelling AE. M & Ms: Mechanosensitivity and Mechanotransduction in Myoblasts. ***Cytoskeleton and Bioemechanics Entanglement and Crosslinking***. APS. Boston, Massachusetts, (2012).
2. **Al-Rekabi Z** & Pelling AE. Microenvironmental Tuning of Precursor Myoblasts. ***Scanning Probe Microscopy in Modern Nanotechnology***. NERM, Postdam, NY, (2010).
3. Fischer SE, Wan F, **Al-Rekabi Z**, Dick S & Harden JL. *Self-assembling Biomimetic Coating from Modular Proteins*. ***Symposium SS: Biosurfaces and Biointerfaces***, MSR Boston, (2009).

Posters

1. **Al-Rekabi Z** & Pelling AE. Matrix Elasticity and Mechanical Force Regulates Myoblast Traction Dynamics. ***Cell Dynamics Workshop***. Elmhirst Resort, Keene, ON, (2013).
2. **Al-Rekabi Z** & Pelling AE. Matrix Elasticity and Mechanical Force Regulates Myoblast Traction Dynamics. ***Summer School in Cell Biophysics***. University of Ottawa, Ottawa, ON, (2012).
3. **Al-Rekabi Z** & Pelling AE. Microenvironmental Tuning of Precursor Myoblasts and Mechanosensitivity. ***VI McGill Biophysical Chemistry Symposium***. University of McGill, Montreal, Quebec, (2010).

Chapter One: Introduction

1.1 Motivation

The human body is extremely dynamic, as the heart beats and the lungs inflate, there are a multitude of deformations and forces. Moreover, this dynamic machine is composed of various types of individual cells that reside in different microenvironments and are exposed to various forces. However, in spite of these differences all of these individual cells within the human body have the ability to sense and respond to physical cues or signals. Fifty years ago, it was stated in a prominent text, which I paraphrase here, in order to understand how living cells work, it is important to know something about their mechanical properties (1). Research involving molecular structures and signaling mechanisms has provided insight into the many aspects of cell function and diseases; however it wasn't until the intervening decades that the mechanical properties of cells (or tissues) were quantified and linked to pathological and biological processes (2). Many elements, such as the extracellular matrix (ECM) and its' molecules and adhesion proteins, are known to act as fundamental mediators between cells and their microenvironments. In some cases, changes to the ECM composition can be viewed in part as a failure of the mechanical components of these cells (2). As an illustration, consider the chronic alveolar lung disease known as emphysema. This disease is characterized by a loss of mechanical elasticity, which is caused by both changes in the biochemistry of the ECM and forces produced by breathing during normal respiration (3). Healthy lung tissue subjected to normal deformations has been shown to possess elasticities in the range of 5-30kPa (4-6); however tissues treated with proteases, in order to mimic the progression of the disease, caused a siginificant loss in the mechanical elasticity, between 33% and 47%. In addition, mechanical properties of the ECM have been identified as an important factor in regulating the differentiation and proliferation of many cell types. Cancer progression in soft tissues for example, is typically associated with an increase in the ealsticty of the ECM due to local accumulation of a dense crosslinked collagen matrix (7, 8). Moreover, nontumorigenic mammary epithelial cells, which normally reside in a relatively soft microenvironment (0.150 kPa) in the breast, show increased proliferation, migration and augmented oncogene signaling (ERK) when cultured on much stiffer substrates (4.5 kPa) (9). Such characteristics are considered hallmarks of tumor cells and are characterized as being an integral component of a transition from a relatively quiescent to a malignant phenotype, driven by local increases in the mechanical properties of the ECM (9, 10).

The preceding paragraph described how a loss of normal ECM mechanical properties can result in diseased states in differentiated cells; however ECM mechanics can influence the fate of undifferentiated cells. For example, matrix elasticity has been shown to direct the fate of stem cells (11). Human mesenchymal stem cells (hMSCs) when cultured on substrates of varying elasticities will differentiate into different types of cells (11). If the microenvironment is soft (E~0.1-1kPa) they differentiate into neurons, if the microenvironment is of intermediate elasticity (E~8-12kPa) they lead to muscle and if the substrate elasticity is stiff (E~25-40kPa) they differentiate into bone (Fig. 1a). Not only does substrate stiffness influence the fate of stem cells but also geometry has been shown to equally influence the outcome of hMSCs. It was previously shown that nanoscale topographies stimulate hMSCs to differentiate into bone cells in the absence of osteogenic supplmenets and with efficiency comparable to that of cells cultured with osteogenic media, (12). In addition, it was recently shown that hMSCs respond to hydrogenated amorphous carbon nano-topographies with groove or grid surface structures, inducing specific changes in their microtubule (MT) organization. In particular, it was shown that grooved nano-patterns influenced stem cell alignment and elongation (13). Moreover, the group further demonstrated that the surface topography with a ratio of width:spacing of 40:30 µm induced hMSCs to acquire neuronal characteristics in the absence of differentiating agents.

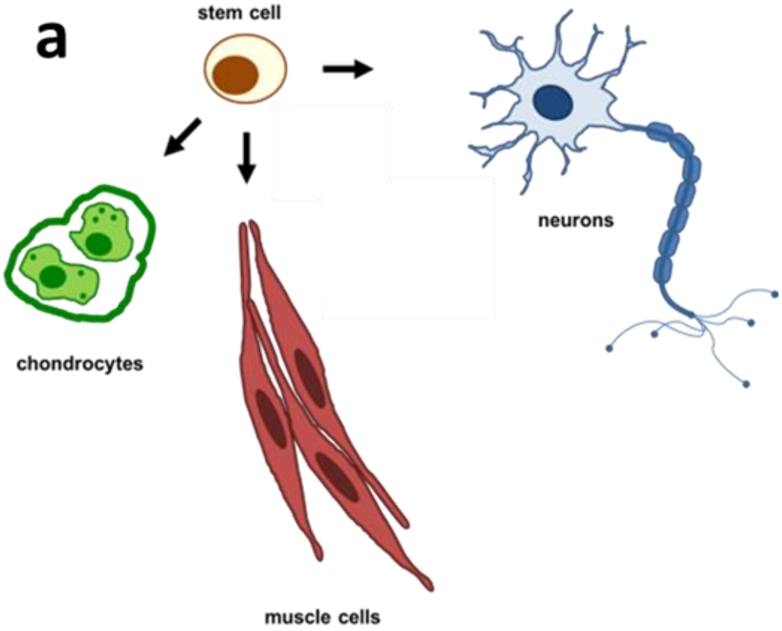

Figure 1.1a The ME governs the fate of hMSCs. A schematic showing how the selective differentiation of MSCs into specific cell phenotypes occurs simply by varying the elasticity of the substrates to which they are attached. In this visual, hMSCs differentiate into bone, muscle and neuronal cells simply by varying the elasticity of ME

In another example, it was demonstrated that for a highly structured biological process such as muscle differentiation, myoblasts optimally differentiate into multi-nucleated muscle fibers - however, only when the surrounding microenvironment mimicked that of resting tissue (14). Considering that muscle cells are being compressed and stretched during contraction, it is not suprising that they induce changes in the local mechanical properties of the microenvironment. When muscle tissue transitions from a resting to a contracted state, it exhibits about an eight-fold increase in elasticity (14-19). During contraction, muscle myoblast cells are exposed to physical forces and also changes in microenvironment elasticity, which induces their activation and eventual fusion into myotubes (myogenesis) (14, 20-24). Initially myoblasts are anchored to the substrate through FAs, where cells are actively and physically probing their surroundings. This is then followed by cell spreading, withdrawal from the cell cycle leading to cell fusion into nascent myotubes. Finally, there is an increase in the expression and assembly of the cytoskeleton and adhesions, which ultimately concludes with characteristic striations along the contractile myotube (14). Therefore, it appears that the late myogenic process is sensitive to substrate mechanics. This suggests that for myotube differentiation and striation to occur, the substrate has to mimic tissue-like stiffness (*E*~12 kPa) (14), (Fig. 1.1b).

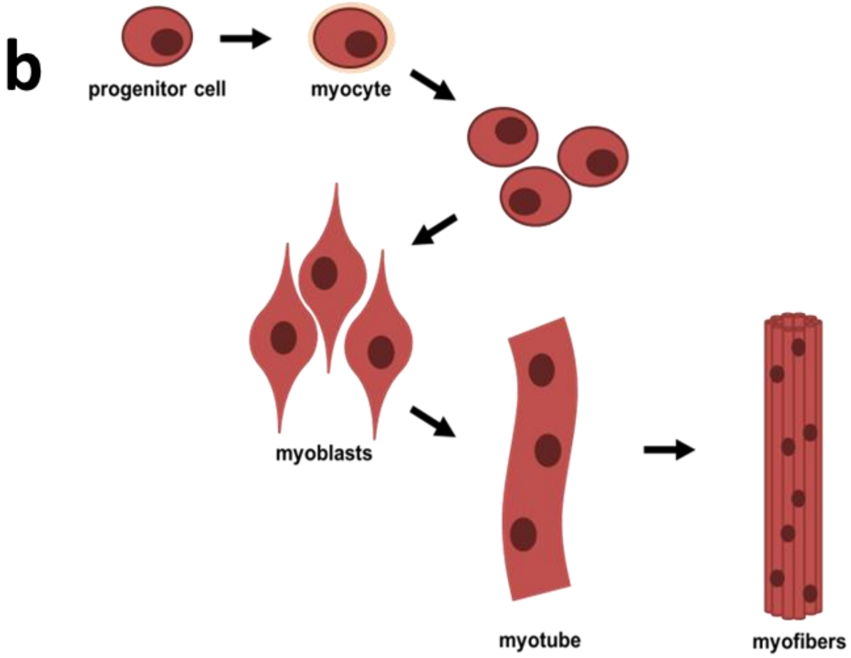

Figure 1.1b The optimal differentiation of muscle precursor cells into multi-nucleated myotubes. Myotube differentiation and striation take splace only on substrates with mechanical properties mimicking tissue-like stiffness (*E*~12 kPa).

The ability of cells to sense variations in the mechanical properties of its microenvironment presumably establishes the cells sensitivity to substrate mechanics (mechanosensitivity) and also determines the distance that cells can sense into their surrounding microenvironment (25, 26). Mechanotransduction, on the other hand, is defined as the cells ability to respond to physical external forces by converting mechanical forces into biochemical signals such as changes in intracellular calcium concentration or by activating diverse signalling pathways (27); whereby these signals can adjust cellular and extracellular structure (27). Cells attach to their surrounding microenvironment via FAs, which are dynamic protein complexes that physically link the cytoskeleton to the ECM. FAs are made up of various mechanosensitive proteins (just to name a few: vinculin, talin and zyxin; discussed in detail in appendix A)

(28). Adherent cells are physically probing the physical properties of their micronevironments, particulary the elasticity and geometry by applying tension to the ECM through the adhesion contacts (29). The magnitude of cell-substrate or cell-matrix deformations is determined by the interplay between traction forces that are applied by the cells and overall compliance of its microenvironment, which is determined by elasticity. It was previously shown that cell-induced deformation of the ECM propagates a finite distance into the matrix (30), which may contribute to the feedback mechanism that regulates cell contractility. Moreover, this is defined as changes in the cell’s ability to produce internal tension as a result of binding between myosin-II motor protein and actin cytoskeleton. Cell contractility typically helps the cell maintain a basal level of cell tension, which enables the cell to constantly and actively sense the mechanical cues in the microenvironment. Therefore, there exists a complex interplay between mechanical cues from the microenvironment and physical forces that ultimately control traction forces, FA and cytoskeletal remodeling. In an attempt to elucidate on the cell’s response to the combined behaviour of substrate mechanics and applied force, the following chapter will briefly cover the proposed hypotheses and aims for the three main studies (chapter four to six) undertaken in this thesis.

Chapter Two: Hypotheses and Objectives

2.1 Main Hypotheses and Objectives

With the above motivations in mind, three major hypotheses with their respective objectives are formulated in order to investigate the basic control of traction forces, in particular with regards to the combined effect of substrate mechanics and external force application.

Hypothesis 1: External forces and substrate mechanical properties together must influence cellular responses in cells; examined herein by measurement of traction forces. In order to test this hypothesis the following objectives were achieved:

- Objective 1: examine the effect of substrate mechanics on cell elasticity and traction forces in myoblasts.
- Objective 2: study the effect of external force application on myoblast traction forces.
- Objective 3: examine the influence of rho-kinase (ROCK) and myosin-II activity on myoblast FAs and traction forces.

Hypothesis 2: Microtubules are responsible in mediating cell elasticity and stable adhesions in cells exposed to myosin-II over-activation. In order to test this hypothesis the following objectives were achieved:

- Objective 1: examine the effect of microtubule depolymerisation and myosin-II over-activation (contractile activation) either alone or in combination on cell elasticity in mouse fibroblasts.
- Objective 2: examine the effect of contractile activation either separately or in combination on fibroblast FAs, projected areas and heights.
- Objective 3: examine the time-dependent effect of microtubule disruption and myosin-II over-activation either alone or in combination on the mechanical properties of fibroblasts.

Hypothesis 3: Cells in which myosin-II is over-activated will no longer generate an increase in traction force and FA assembly in response to an externally applied force. In order to test this hypothesis the following objectives were achieved:

- Objective 1: determine optimal substrate elasticity where fibroblasts exhibit the greatest change in traction forces when exposed to mechanical deformation.
- Objective 2: examine the effect of myosin-II over-activation on fibroblast morphology in fibroblasts.
- Objective 3: quantify how myosin-II over-activation disrupts traction force dynamics of cells when exposed to extracellular forces on substrates of optimal elasticity.

2.2 Thesis Outline

The remainder of this thesis includes four chapters which describe the experimental procedures and results relating to the hypotheses and objectives outlined above. These chapters are followed by five appended sections for those who wish to obtain further details relating to the major topics and techniques used in this thesis. Prior to describing the results, the main experimental and theoretical approaches used to test the three main hypotheses are described in chapter three. Details include a description of the two main techniques used herein – atomic force microscopy (AFM) and traction force microscopy (TFM). AFM is the technique we used to apply controlled external forces to cells, and to measure their mechanical properties. TFM was used to quantify traction forces, generated by cells, on a variety of substrates. Additional microscopy techniques (epi-fluorescense and confocal) that were also used in this thesis are explicity detailed in appendix B.

Chapters four through six highlight the series of experiments and results obtained in relation to the aforementioned hypotheses. These chapters are included as manuscripts prepared for journal publications. In all of these chapters, TFM was used as an indicator of the cellular response to applied forces. Cells were subjected to controlled extracellular forces (via AFM) on substrates of increasing elasticity. Five distinct substrates were produced with elastic moduli ranging from ~16-89 kPa. In addition, pharmacological agents were used to either inhibit or increase cellular contractility (ROCK inhibitor: Y-27632 and myosin-II inhibitor: blebbistatin or myosin-II activator: calyculin A and microtubule depolymerizer: nocodazole respectively. Also see subsections 4.2.2, 5.2.1 and 6.2.1 for details), all while performing TFM. This allowed us to investigate the influence of signaling pathways on traction forces (section 3.4 to 3.6), mechanical properties of cells, FA size, and cellular area. In these outlined chapters, we show that two distinct cell types (C2C12 mouse myoblasts and NIH3T3 mouse fibroblasts) increase the magnitude of generated traction forces in response to extracellularly applied force, however only on specific substrate elasticities. Therefore, the results from these studies reveal two interesting outcomes. First, these studies reveal the important result that cells sense and respond to both substrate mechanics and external forces, simultaneously. And second, our results demonstrate that the response depends on the regulators of cellular contractility and the microtubule cytoskeleton.

For those wishing to read further on topics involving how cells attach, sense their microenvironment, generate and transmit forces, which includes the cytoskeleton, FAs, integrins and ECMs, this information can be found in Appendix A. Additional information relating to microscopy tools that have been used in this thesis as phase contrast, epi-fluorescense and confocal microscopy can be found in Appendix B. Appendix C describes the detailed optical flow registration algorithm that was used to obtain the displacement fields of the deformed substrates. Appendix D discusses the rheological method used to demonstrate that the hydrogels used throughout the thesis behave as linear elastic solids. Finally, appendix E describes the statistical analysis employed in chapter’s four to six.

Chapter Three: Experimental and Theoretical Methods

This chapter reviews the two major techniques used to achieve the aims in chapter two in order to test the proposed hypotheses.

3.1 Atomic Force Microscopy (AFM)

In 1986, a group of researchers at IBM Zurich developed the Atomic Force Microscope (AFM) (37) as an extension of the Scanning Tunnelling Microscope (STM) (38). The STM was primarily used to measure the topographies and surface properties of conductive surfaces at atomic resolution (37), by raster-scanning the surface with an extremely sharp tip to which a bias voltage is applied.

Generally, if the material being scanned is sufficiently conductive, a tunneling current produced as a result of the quantum mechanical effect of electron tunneling through a vacuum can be measured (39). Moreover, the changes in this measured current can be directly related to changes in height between the tip and the conductive material in a highly sensitive manner. This current (I) decays exponentially with distance as

$$I \ \propto \ e^{-\frac{\sqrt{2m\Phi}}{\hbar}d}, [3.1]$$

where d is the distance of the barrier, measured in Ǻ, m is the mass of the electron, Φ is the energy barrier in eV, which depends on the applied voltage and $\hbar$ is Planck's constant divided by 2π. Considering an increase in the enrgy barrier of 2-5 Ǻ, which is the typical radius of an atom, will decrease the currents by upwards of 3 magnitudes. This means that the current measured is largely from the single atom at the end of the STM tip.

The atomic resolution achieved by the system became highly attractive for imaging biological samples. Advances in the technique to enable imaging in ambient temperature and pressure (40, 41) allowed biological samples such as DNA, enzyme complexes, bacteriophages, and lipid membranes to be imaged by STM (42, 43). However, resolution was lacking because certain biological samples are capable of conducting electrons, therefore, the currents measured from these samples are much weaker than those from metallic materials and not all regions are fully resolvable on the atomic scale (40). In order to rectify these problems, biological samples were coated with a thin conducting layer prior to imaging. On the other hand, this metallic coating could be removed from the sample and then used to produce a mask, which can then be imaged as in Transmission Electron Microscopy (TEM) (40). However, the thin metallic coating only allows for atomic resolution of the metal coating and not the sample underneath. This technique also makes it impossible to image biological samples in its natural environment. In addition, the sharp tip used can be also be detrimental to soft biological samples, which have not been further protected (40).

Conversely, the AFM makes use of a sharp tip to profile the topographical features of a sample through direct physical contact with the surface. Therefore, this eliminates the need to measure changes in tunnelling currents, and therefore facilitates the imaging of non-conductive surfaces or materials as soft biological samples. Moreover, the AFM measures the physical interaction forces between a sample and the tip (44) and may also be operated in aqueous environments with a range of temperatures. Therefore, all these properties make it possible to use the AFM as a probing tool for biological samples within their native environment (45).

3.1.1 General Instrumentation of an Atomic Force Microscope (AFM)

In principal, the AFM operates by usually having a sharp pyramidal tip raster scanning the surface of the sample. Usually, cantilevers are batch micro-fabricated from single crystal silicon or silicon-nitride and often coated with a reflective metal such as gold or aluminum (46). The probe is attached at the tip to a flexible cantilever, which is harnessed to a system of piezoelectric ceramic crystal that moves in the three dimensions. When the tip is brought close to the sample, forces between the tip and the sample lead to the deflection of the cantilever by obeying Hooke's law for small displacements:

$$F = k_c d. \, [3.2]$$

These deflections are detected using a laser spot which is reflected off the upper surface of the cantilever and onto a quadrant photodiode detector. As seen in (Fig. 3.1.1), four photodiodes are positioned symmetrically around the center and each quadrant is separated from one another by a narrow gap. The position information can be obtained from the individual signals received from the quadrants since the electrical contributions define the relative position of the light spot with respect to the gap position (47). The displacements with respect to the gap position can then be approximated by:

$$\Delta x \approx k_{QD} \frac{(v_1 + v_2) - (v_3 + v_4)}{v_1 + v_2 + v_3 + v_4}, [3.3]$$

$$\Delta y \approx k_{QD} \frac{(v_1 + v_4) - (v_3 + v_2)}{v_1 + v_2 + v_3 + v_4}, [3.4]$$

Where v_1, v_2, v_3 and v_4 are the average signal voltages of quadrants 1, 2, 3, and 4 respectively, and k_{QD} is a scaling factor which converts the relative displacements into absolute displacements, as a result of the geometry of the light spot. Thus with the spring constant (k_c), all deflection measurements (d) can be directly converted to a force (F) (48, 49).

Typically, the AFM is mounted onto a stationary stage while the scanning movement of the tip is controlled by a piezoelectric crystal. Depending on the setup of the AFM, generally the sample is held stationary while the tip scans the surface, the reverse can be possible. The desired force, also known as the set-point is set depending on the experiment, and a feedback loop corrects the piezo height in order to keep this set force constant, (Fig. 3.1.1).

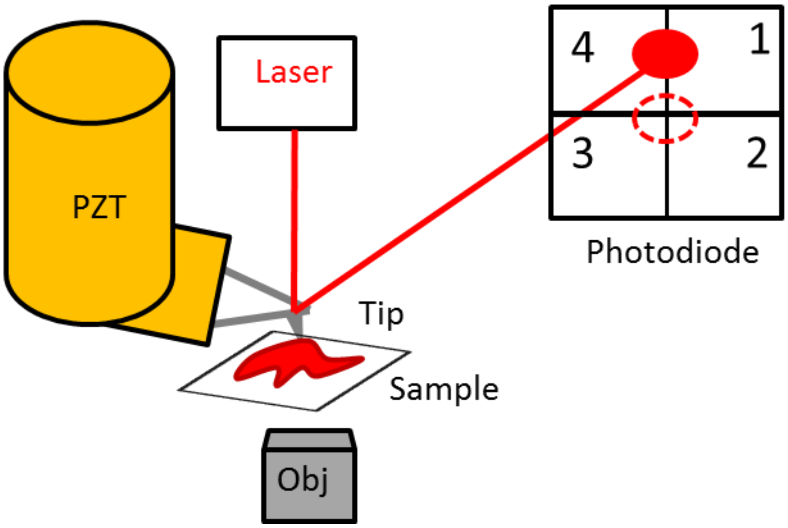

Figure 3.1.1 The main components of the AFM. (a) A schematic illustration that depicts the the main parts of an AFM which are: (1) a sharp tip mounted on a flexible cantilever, which acts as a spring, (2) a laser diode used for tracking the vertical and lateral motion of the cantilever, (3) a position sensitive quadrant photdiode, which detects the reflected laser beam from the cantilever, and (4) a piezo device for positioning and scanning the AFM cantilever tip.

The piezoelectric materials are able to create an electric field when strain is applied along an axis (direct piezoelectric effect) or to expand or contract in response to an applied electric field (converse piezoelectric effect) (50). In an AFM, the crystal used expands and contracts in response to changes in voltage detected by the photodiode such as,

$$\Delta t_{out} = d_{ij} V_{IN}. \, [3.5]$$

Here a change in thickness of the piezo crystal (Δt_{out}) is caused by an applied voltage (V_{IN}) multipled by the piezoelectric charge constant d_{ij}. This constant describes the amount of strain experienced by the crystal along both the applied electric field and the axis in which a response occurs (50).

As mentioned above, the AFM employs a feedback system that quickly and accurately adjusts for the force applied on the sample and returns it to the desired force value, which corresponds to the set-point voltage. Moreover, in other AFM modes, the set-point maybe coupled to amplitude or height rather than force. The error signal, which is the difference between the detected voltage and the set-point, is constantly minimized by the feedback loop. A closed feedback loop is often used, where in this case strain gauges are coupled to the piezo-scanner and measure the actual change in the piezo-height when there is a non-zero error signal. In order to make any corrections necessary for example from hysteresis due to piezo-expansion, the strain gauge measurements are compared to the desired change in height. Moreover, the speed and accuracy of the feedback adjustments can be controlled using the gains by the Proportional-Integral (PI) control system. The P gain directly multiplies the error signal and proportionately affects the drive signal to expand or contract the piezo. However, in such cases the set-point is often overshot because of hysteresis of the piezo, therefore the I gain dampens the response of the P gain by considering the changing discrepancy between the set-point and current values. This dramatically reduces the time it takes to return to the set-point in addition to eliminating the overshoot that occurs when the P gain is used alone (51). Ideally, the P and I gains should be maintained at as high a value as possible in order to decrease the response time; however, not so high that the piezo starts to resonate. Therefore, a feedback system is used so that the force applied by the AFM tip on to the sample can be maintained at a constant value throughout an experiment.

3.1.2 Calibration of the Cantilever

The cantilever can be modelled as a linear spring by applying Hooke's law for small deflections as in equation [3.2].

Generally the manufacturer specifies the spring constant of the cantilever, however the exact value can change because of difficulties in controlling the geometry and thickness of the microfabricated cantilevers (52). Various techniques have been employed to measure the spring constant of the cantilever; thermal noise (53), resonance frequency (54) or using the intrinsic material properties of the cantilever (55). Knowing the spring constant of the cantilever with its deflection, force can be easily calculated using Hooke's law (from equation [3.2]). The method used throughout the experiments in this thesis is called the thermal noise method (52). Here the cantilever is modelled as a harmonic oscillator with one degree of freedom, which fluctuates in response to thermal noise (53). The Hamiltonian for this system is:

$$H = \frac{p^2}{2m} + \frac{1}{2} m\omega_0^2 d^2, [3.6]$$

where d is the displacement of the oscillator, m is its mass, p its momentum and ω_0 is the resonant frequency. The equipartition theorem (53) states that the average value of each quadratic term of the Hamiltonian equation is equal to thermal energy ($^{k_bT}/_2$), where k_b is the Boltzmann factor and T is the temperature. Therefore, the equation can be written as,

$$\langle \frac{1}{2} m\omega_0^2 d^2 \rangle = \frac{1}{2} k_b T. [3.7]$$

Since the spring constant is $k = m\omega_0^2$, then substituting that above the spring constant becomes,

$$k = \frac{k_b T}{\langle d^2 \rangle} \text{ . [3.8]}$$

Besides thermal fluctuations there are other sources of noise and hence to eliminate the noise in the measurements, the measurements should be done in frequency domain, where it becomes easier to isolate the noise contributions from the peak corresponding to the resonant frequency. A Lorentzian curve is fitted to the amplitude-frequency relationship for the cantilever, which is modeled as a simple harmonic oscillator:

$$A(f) = \eta^2 + A_{DC}^2 \left(\frac{f_0^4}{(f^2 - f_0^2) + \frac{f^2 f_0^2}{Q^2}} \right), \text{[3.9]}$$

Where A_{DC} is the DC amplitude, η the background noise, Q is the quality factor and f_0 is the resonant frequency of the cantilever.

Therefore, the integral of the Lorentzian fit to the resonant frequency peak in the power spectrum measured, is equal to the mean-square displacement, in the time domain, $\langle d^2 \rangle$,which allows for the direct determination of the spring constant. This method was found to be accurate when measuring the spring constant of triangular cantilevers which is used throughout our experiments presented in this thesis and in most AFM studies (52). The values of k obtained in this manner have been shown to correspond extremely well to those obtained mathematically (53, 56).

3.1.3 Modes of Operation of the AFM

The AFM can be operated in three main imaging modes (41, 57): contact mode, tapping mode, and non-contact mode, (Fig. 3.1.3).

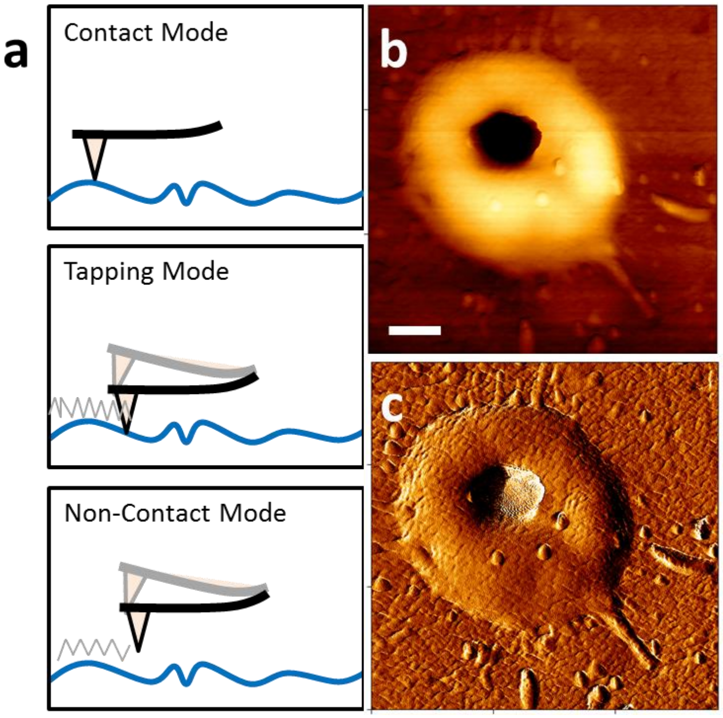

Figure 3.1.3 Imaging Modes and AFM images. (a) The three imaging modes used in AFM: contact, tapping and non-contact mode. Contact mode can be used to generate (b) the height images or (c) deflection images (an ablated surface of poly-methyl-methacrylate). The height images contain the true height information of the sample, while the deflection imaging loses that information; however it is able to generate finer details in the sample because the response of the feedback look is much faster in correcting the position of the small cantilever than that of the piezoelectric element. Scale bar: 3μm.

In *contact mode* the tip makes soft 'physical contact' with the surface of the sample, The deflection of the cantilever *d* is proportional to the force acting on the tip, via Hooke's law (Equation [3.2] from Sub-subsection 3.1.1). The tip either scans at a constant small height above the surface or under conditions of constant force; therefore, the feedback control loop is turned ON in this mode. In the constant height mode, the height of the tip is fixed, whereas in the constant force mode, the deflection of the cantilever is fixed and the motion of the scanner in the z-direction is recorded. In addition, this mode represents the repulsive regime of the intermolecular force curve. One of the primary drawbacks of the tip remaining in contact with the sample is that large lateral forces can be exerted on the sample as the tip is dragged over the specimen.

For *contact mode* imaging, it is reassuring to have cantilevers that are soft enough to be deflected by the very small forces and have high enough resonant frequencies to not be susceptible to vibrational instabilities. The disadvantage of this mode is the large lateral forces exerted by the tip to the sample can distort the image and limit the ‘atomic’ resolution.

Now, in order to overcome the issue of lateral drag forces on the sample, the *tapping mode* can be used, (58). In *tapping mode,* the cantilever is oscillating close to its resonance frequency, where an electronic feedback loop ensures that the oscillation amplitude remains constant, such that a contact tip-sample interaction is maintained during scanning. The forces that act between the sample and the tip will not only cause a change in the oscillation amplitude, but will also change the resonant frequency and the phase of the cantilever. The amplitude is used for the feedback and the initial adjustments of the piezo-scanner are recorded as a height image. Simultaneously, the phase changes are presented in the phase image. In other words, the tip makes intermittent contact with the surface. As the tip is scanned over the surface, the cantilever is driven into resonant frequencies (100s of kHz). Since the contact time is a small fraction of its oscillation period, the lateral forces are reduced dramatically. The advantages of this mode are the elimination of a large part of permanent shearing force and the reduction of damage to the sample surface even with stiffer probes. The *tapping mode* is preferred to image samples with structures that are weakly bonded to the surface, or very soft samples.

In the *non-contact mode*, the probe operates in the attractive region and the tip-sample interaction is minimized. The use of the *non-contact mode* allows scanning without influencing the shape of the sample by the tip-sample forces. In most cases, the cantilever of choice for this mode usually has higher spring constants 20-100N/m so that it does not stick to the sample surface at small amplitudes.

The cantilever oscillates above the surface of the sample at distances such that it is no longer in the repressive regime but in the attractive regime of the intermolecular force curve. The operation of the *non-contact mode* imaging is quite difficult in ambient conditions because of the existing thin layer of H_2O on the tip and the surface.

Throughout this thesis, the AFM probe is used here as a local indenter rather than a tool for topographical imaging. The AFM was also used to extract important parameters as mechanical properties of living cells. By analyzing the indentation of the tip into the sample as a function of force, the elasticity, (or Young's modulus), of the sample can be determined from so-called force-displacement curves as we will discuss in next Subsection (3.2).

3.2 Force Curve Analysis

The majority of AFM mechanical measurements on living cells rely on nano-indentation approaches which extract mechanical parameters from measured "force-displacement" curves (87). The force-displacement curve is measured by recording the force acting on the cantilever when it is moved towards and away from a sample (Fig. 3.2-1a). From this data, the force-displacement curve can provide information on adhesion (88), stiffness (89), and other properties such as the elasticity (Young's modulus) of the sample (38).

In an indentation experiment, where the measurement and quantification forces between an AFM tip and the material is performed by measuring a force-curve. In this mode, the position of the tip is not changed, the tip is brought in and out of contact with the sample and the deflection is monitored (59). Using equation [3.2] we can derive the Young's Modulus for a given geometrical cantilever used.

When performing experiments the deflection is exclusively zero because there may be stresses in the cantilever, which may deform it even if no external load exists and hence an offset d_0 must be subtracted from all deflections (59, 60) and thus equation [3.2] becomes

$$F = k_c(d - d_0)\ . \quad [3.10]$$

On very flexible substrates the tip indents the sample to some extent due to the application of the loading force and hence the indentation δ is given by the difference between the sample height and the deflection of the cantilever d ,

$$\delta = z - d\,. \ [3.11]$$

Once again, the offsets have to considered for both the height and the deflection and so I can transform equation [3.16] into the following

$$\delta = (z - z_0) - (d - d_0). \ [3.12]$$

Here d_0 is the deflection offset and z_0 is the z position at the point of contact.

We can apply the Hertz model (61), which describes the indentation of an infinitely extended sample by a simplistically shaped tip. This model generally describes the classic rigid sphere on a flat surface and is valid for indentations significantly smaller than the spherical radius of the indenter. This model was developed in the late nineteenth century by Hertz and was later extended by Sneddon (62), where he described a rigid cone indenting a soft flat surface (this model is used in this thesis for sharp tips). For the Sneddon model the indentation has to be so large that the cone apex can be considered infinitely sharp. The two most common tips used in the AFM are the conical and parabolic tips. In the case of both indenters, the loading force can be calculated from the material properties of the sample (Young's Modulus, *E* and Poisson ratio, ν), the geometry of the open angle of the tip, α and the indentation δ:

$$F_{conical} = \frac{2}{\pi} \cdot \frac{E}{(1-\nu^2)} \cdot \delta^2 \cdot tan(\alpha). \ [3.13]$$

$$F_{parabolic} = \frac{4}{3} \cdot \frac{E}{(1-\nu^2)} \cdot \delta^{\frac{3}{2}} \cdot \sqrt{R}\,. [3.14]$$

These equations relate between the force *F* that is applied to the sample and the indentation *δ* of the tip into the sample. *E* is the elasticity or Young's modulus of the sample. The other parameters in the equations are *α*, the half opening angle of the tip for a conical indentation (equation [3.13]), and *R*, the sphere radius in the case of a sphere indentation (equation [3.14]). The Poisson ratio ν can have values ranging between 0 and 0.5. Generally, a value of 0.5 is given to incompressible samples and 0.3-0.5 are the typical values used for cells. Moreover, equations [3.13] and [3.14] assume that the material is homogenous, isotropic and infinitely passive (48, 60). These assumptions are met if the cell is indented slowly enough (1µm/sec), such that viscous conditions are small and force measurements are dominated by the elastic behavior. At higher rates or cantilever speeds cells appear stiffer. It was previously shown that at speeds greater than 10µm/sec, hydrodynamic forces acting on the cantilever increased the apparent force considerably (48).

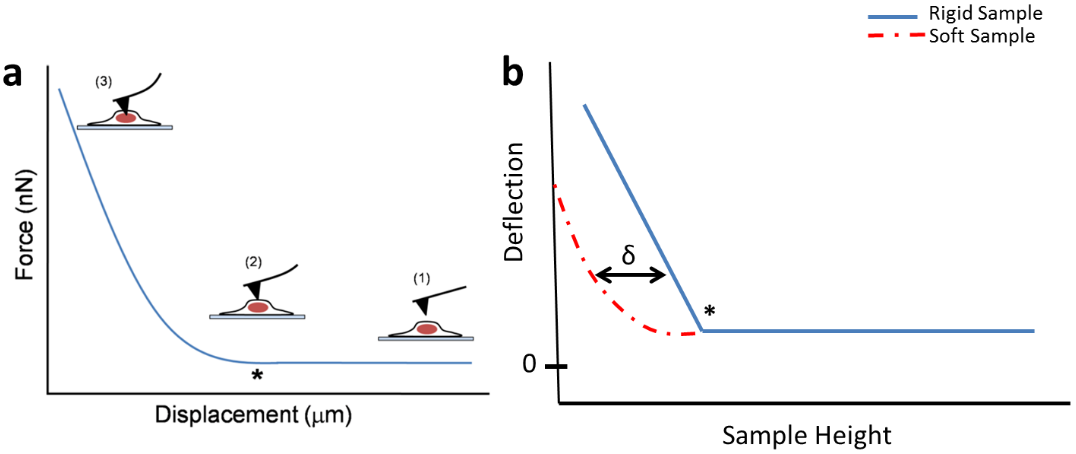

Figure 3.2-1 Typical force-curves. (a) A typical force-displacement curve measured with AFM is a record of the force acting on the AFM cantilever as it is moved (or displaced) towards and away from a living cell. (1) The AFM tip is first moved towards the cell, however because the tip and cell are not in contact there is not force acting in the cantilever. At the contact point (*), the tip touches the cell (2), the cantilever starts to deflect upwards. The tip continues indenting into the cell until a user defined set-point is reached (3) at which the tip retracts away from the cell back to its original position (1). The resulting force-displacement curve can be analyzed and mechanical properties such as the elasticity (or Young`s Moduli) can be extracted. (b) The contact point is easy to observe on a rigid sample as there is an abrupt change in slope; however on a soft sample this contact point is much more difficult to determine. The indentation depth δ is the difference between the deflections measured on a rigid versus a soft sample.

A spherical indentation differs from a conical indentation in both the contact area and indentation profile, and the two can be used to compare local versus global variations in elasticity. Spherical indentation has a much larger surface area (>10 µm^2 for a 200 nm indentation) when compared to a conical indentation where the contact surface area for a 200 nm indentation is < 100 nm^2. The elasticity values obtained using conical tips (Fig. 3.2.-2a) are usually higher than those obtained with spherical tips (Fig. 3.2-2b) (60). This is mainly due to the small contact area of the tip with the sample, where the tip is almost in direct contact with single actin filaments and is influenced by their high elasticity of around ~2GPa (63), and thus force is dissipated directly into the cytoskeleton. On the other hand, the spherical beads have a large contact area with the cell and are more highly influenced by the cell membrane and cytoplasm as it flows through the cytoskeleton in response to the applied force, and force is mainly dissipated into the cytoplasm and membrane.

Fitting of force curves measured on live cells to the Hertz model (or Sneddon model for pyramidal tips) is usually done for small indentations of <1000 nm. This is in order to minimize the contribution of the stiff substrate, to which the cell adheres, to the elasticity measurement (64) and where the geometry of the indentation matches the geometry of the indentor. Therefore, deeper indentations will usually result in increasing calculated elasticity values.

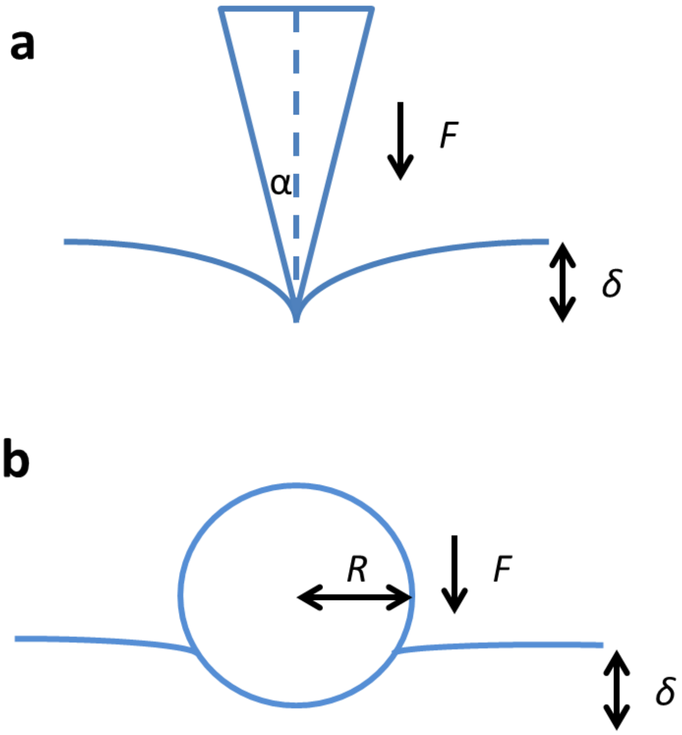

Figure 3.2-2 Conical and Spherical indenters. (a) Conical and (b) spherical indenters. The relationships between the force applied *F*, elasticity of the sample. *E* and indentation depth δ. ν is Poisson's ratio of the sample, α is half the opening angle of the conical indenter, and *R* is the radius of the spherical indenter

3.3 Methods to Detect and Measure Cellular Traction Forces (CTFs)

The idea of using deformable compliant substrates to detect and measure traction forces was first conceived by Harris and co-workers (65). Their paper laid the basic foundations for all the current methods used to quantify traction forces. Many groups were investigating the role of cell contraction; however no group in particular was able to map the forces to location on the cell body or quantify the magnitude of these tractions. Harris et al. used the notion of calculating traction based on substrate deformation to create the first method ever in investigating forces generated by locomoting cells (Fig. 3.1-1). The cell exerted forces which were translated onto deformable substrates as wrinkles. In addition, they were able quantify the size and distribution of the wrinkles caused by the adherent or locomoting cell. Therefore, this landmark development paved the way for the current methods used in measuring traction forces generated by cells. However, there were some problems with this technique as diffulty in obtaining reproducible results because of the intrinsic non-linearity of the wrinkle formation. The wrinkles form slowly and are often larger than the cell, resulting in poor spatial and temporal resolution.

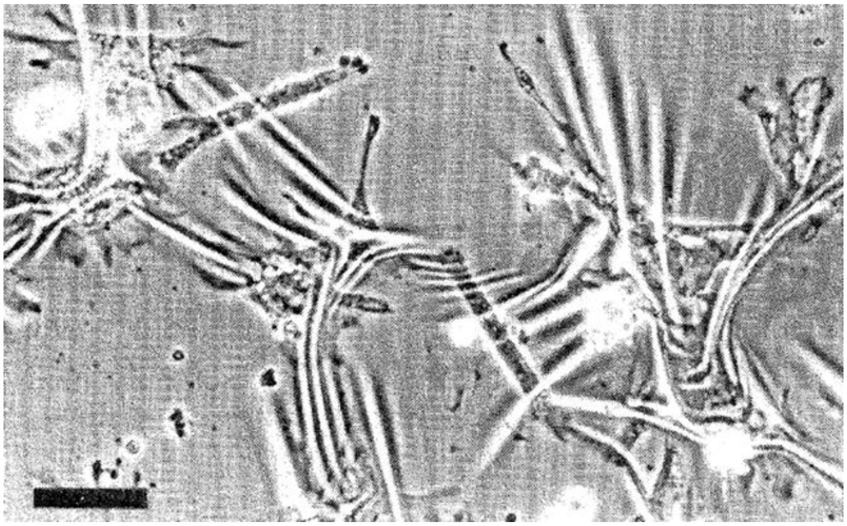

Figure 3.3-1 The `wrinkling` substrate. Harris et al. (65) developed the first technique to measure CTFs. Forces are measured based on wrinkles created in a silicon substrate due to the force exerted by adherent fibroblasts. Scale bar: 100μm.

Therefore, Lee et al. (66) modified the above method by adding 1 µm beads. In this method, traction forces are calculated based on the in-plane displacements of the beads, which are much easier to detect and track than the wrinkles in the substrate. As the cell attaches or migrates on these substrates, the cell deforms the substrate causing the beads to move from their initial positions. The 'strained' field under the cell is compared to the 'unstrained' field after the cell moves away from that region-of-interest, causing the relaxation of the bead field and so the strain field can be calculated. Therefore, utilizing micron diameter-sized beads, more accurate information of the location, magnitude and direction of the traction forces was obtained than in the previous method. The introduction of beads into compliant substrates proved much accurate in calculating forces exerted by adhering or locomoting cells, however the silicone substrate are much less useful for studying most mammalian cells. Therefore, to accurately calculate traction forces, the substrate must be tuned to match motility and force generation of a given cell type. It is very difficult to tune silicone substrates to a desired compliance for slower or non-motile cells which produce higher forces.

Polyacrylaminde (PA) substrates embedded with sub-micron sized fluorescent beads were developed to overcome this limitation (67). The compliance of the PA substrate can be tuned chemically by varying the monomer to crosslinker concentrations (68). PA gels proved to be advantageous over silicone substrates, such that over a wide range of deformations, PA gels display linear elastic behaviour. In addition, PA substrates need to be conjugated with specific cell adhesion ligands as collagen or fibronectin (69) to promote cell adhesion so this design acts as a perfect controlled scaffold for studying cellular behaviours.

Another more efficient and less expensive technique used where there is no need to functionalize the substrate using an ECM protein in order to promote cell attachment is using gelatine. Initially, gelatine was developed as a traction force assay compatible with high-resolution calcium imaging in order to investigate how calcium transients coordinate traction force generation in different regions of moving cells (70). Gelatine substrates are transparent and non-fluorescent (Fig. 3.3-2a) and most importantly highly responsive, allowing submicron bead displacements (Fig. 3.3-2b) to be detected in less than 1 sec.

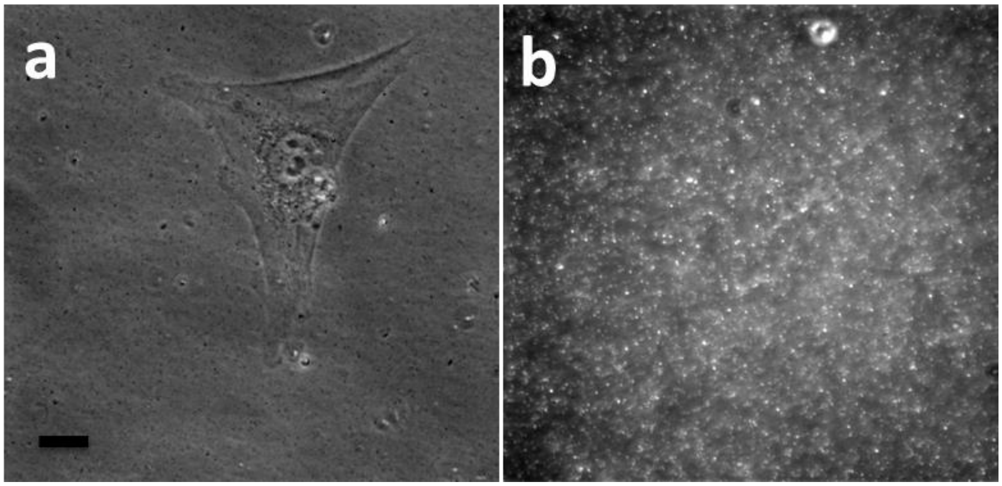

Figure 3.3-2 Simultaneous phase and fluorescence images of C2C12 myoblast cell on a ~64 kPa GXG substrate. (a) Phase contrast image of a C2C12 cell and (b) is its corresponding fluorescence image, where fidiciuary fluorescent beads (200 nm in diameter) are embedded in the GE substrate. Scale bar: 21µm.

Microposts are also employed to measure traction forces. This method was developed by Tan et al. (71) where forces can be measured at discrete locations. The group designed a substrate containing an array of evenly spaced micropillars or as the group termed it microneedles made of silicon elastomer (Fig. 3.3-3). The tips of the pillars can be coated with ECM proteins to promote cell attachment and the mechanical compliance of the posts can be tuned or altered by varying the height of the posts. Cells attach to the top of this sheets of 'needles' and because the posts are elastomeric, traction forces exerted by the cell cause the micropillars to bend. Based solely on simple bending mechanics, the force exerted by the cell on an individual post can be calculated by tracking the displacement of the tip of the post (which is fluorescently labelled) from its original position.

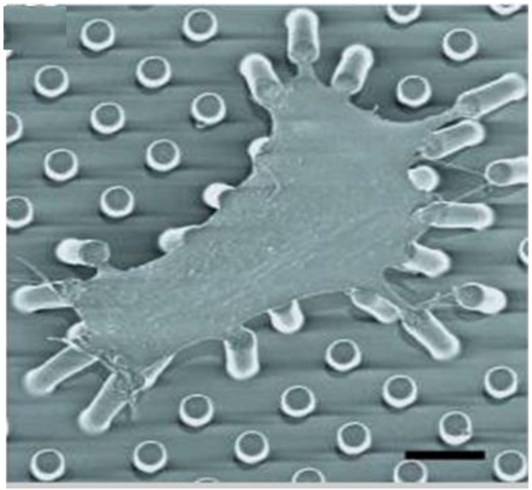

Figure 3.3-3 Smooth muscle cells cultured on arrays of posts. Tan et al. (72) developed a lithographically created microarray of posts that can be deflected by cellular force. Scale bar: 10µm.

Using this method they found some interesting results showing that two distinct adhesions exist. First, adhesions that are larger than 1 μm^2 exerted a force proportional to its area. Second, smaller adhesions appeared to exert disproportionately larger forces. The group concludes that these larger forces may be focal complexes rather than mature FAs. These results relatively agree with the findings of Beningo et al. (73) that showed that small nascent adhesions were capable of generating larger traction forces. Tan et al. (71) also examined how cell size correlates with force by reducing the number of ECM-coated pillars in a given area of interest, They found that when cell spreading was restricted, those cells exerted less traction force, however when those same cells were transfected with a constitutively active RhoA, the cells were able to exert forces. Their study showed that there is a direct link between cell morphology and biochemical changes that result in changes in contractility.

3.4 Traction Force Microscopy (TFM)

Motile and adhesive cells generate internal forces through actomyosin interactions and exert traction forces on the underlying elastic substrate or extracellular matrix (ECM). The forces exerted by the cell on the substrate are called cellular traction forces (CTFs) and are essential for cell migration, mechanical signal generation and other cellular functions. As such, CTFs are involved in numerous biological processes including inflammation, wound healing, tissue morphogenesis, embryogenesis, angiogenesis and metastasis (74). In this section, I will initially describe the method used in measuring CTFs. This involves fabricating the substrates (see sections 4.2 & 6.2) and imaging cells using epi-fluorescence microscopy (appendix B). Second, the displaced fiduciary marker beads embedded within the elastic substrate are detected using a correlation-based optical flow algorithm. And finally, a detailed discussion on the physics behind substrate deformation as a result of CTF: classical theory of small-strain and plane-stress elasticity. The main result of such an analysis is a transform expressing the displacement field of the elastic substrate as an integral over the traction field.

3.4.1 Determining Substrate Displacement Field: The Correlation-Based Optical Flow Method

A single cell of interest is selected and a digital image of the field is recorded using simultaneous phase and epi-fluorescence (aee appendix B). This yields the “strained, I_1” image. Subsequently, cell substrate attachments are disrupted using 10mM EDTA (see sections 4.2 & 6.2). The elastic strain energy in the substrate is thereby released and the beads recoil to their undisturbed positions. Without moving the microscope stage a second image is captured. This image is denoted as the “unstrained or null, I_0” image.

This section is summarized from Marganski et al. (75). We start with the recorded images I_1 and I_0 that show the distribution of fiduciary marker beads in the strained and null substrate. These images are loaded into large matrices of N_x columns by N_y rows:

$$I_k \equiv \begin{bmatrix} P_k(1,1) & P_k(2,1) & \ldots & P_k(n_x-1,1) & P_k(n_x,1) \\ P_k(1,2) & P_k(2,2) & \ldots & P_k(n_x-1,2) & P_k(n_x,2) \\ \vdots & \vdots & \vdots & \vdots & \vdots \\ P_k(1,n_y) & P_k(1,n_y) & \ldots & P_k(n_x-1,n_y) & P_k(n_x,n_y) \end{bmatrix}, [3.15]$$

where the subscript k = 0 or 1 and $P_k(x,y)$ is the intensity at the pixel (x, y).

Deformation of the substrate by cultured cells was determined relative to the relaxed substrate, I_0, based on pattern recognition using cross-correlation algorithm. Briefly, a force-loaded bead image, I_1, was first divided into small square areas or correlation windows (C). The computer program then tries to match the bead pattern in each small square of the force-loaded or strained image, I_1 ((u, v) are some pixel coordinates in I_1) against the pattern in different regions of the null-force image, I_0 ((x, y) are some pixel coordinates in I_0), searching for a best match. Deformation vectors were then drawn from the position in the null-force image to the position in the force-loaded image with the best match (Fig. 3.4).

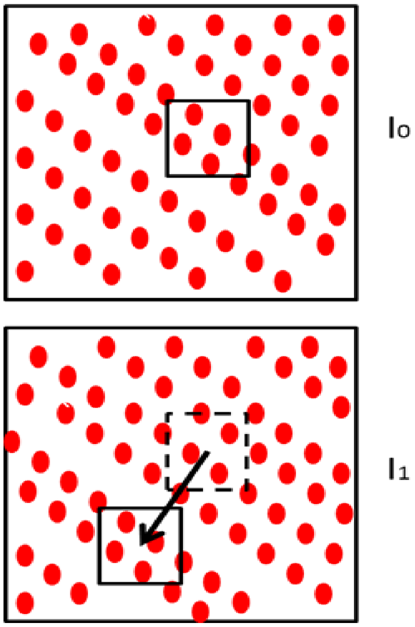

Figure 3.4 Correlation-based optical flow. Basically pixel intensity patterns are compared between two images I_0 and I_1 to compute a motion field. The method first defines a reference window in I_0 (solid outline). Then similar patches within I_1 are examined, starting with a window (dotted outline) centered at the exact pixel coordinates as the reference window. After finding the window (solid outline) within I_1 that has an intensity pattern most similar to the reference window, a displacement vector is constructed that starts form the center of

the dotted outline terminating at the center of the solid outline. This vector gives an estimate of the local substrate motion.

Hence, for fluorescent images of substrates, which usually have a very high contrast, we can measure the optimal image similarity in the proximal regions of (x, y) in I_0 and the nearby region of (u, v) in I_1,

$$R(x,y,u,C) \equiv \frac{\sum_{\delta_x}\sum_{\delta_y} P_0\left(x+\delta_x, y+\delta_y\right) P_1\left(u+\delta_x, v+\delta_y\right)}{\left(\sum_{\delta_x}\sum_{\delta_y} P_0^2\left(x+\delta_x, y+\delta_y\right)\right)^{1/2}\left(\sum_{\delta_x}\sum_{\delta_y} P_1^2\left(u+\delta_x, v+\delta_y\right)\right)^{1/2}}, \quad [3.16]$$

In the above expression, the summations extend over the values δ_{x} and δ_{y} within the correlation window.

The degree of match was scored with a normalized cross-correlation equation, which yielded a value of 1 for a perfect match and 0 for no similarity. No vector was assigned if this value fell below a user-defined threshold. In regions where the deformation was larger than one pixel, additional vectors were generated at a progressively shortened distance from each other to provide a higher density data. The size of the square, the distance for the pattern search and the threshold for positive identification were determined empirically, in order to generate an optimal set of vectors that match visual assessment of substrate displacement when the null and force loaded images were displayed in quick succession.

The correlation window (square) in I_0 is centered at the point (x, y), which is also considered as a fixed reference, (Fig. 3.4a). Fig. 3.4b depicts a dashed box centered at the same location as the fixed reference window ((u, v) = (x, y)). Now the substrate has moved and the features enclosed in this dashed box are different. The second window I_1 (solid box) has been translated to a new location with centre (u^*, v^*), where the normalized function $R(x,y,u,C)$ is maximized. The vector from the centre of the dashed window to the centre of the solid window provides a good estimate of the local substrate motion.

Among several significant parameters in the correlation-based optical flow, the size of the of the correlation window C is the most significant. The value of C is determined by matching it with the density of the fiduciary marker beads by trail and error. If C is too small in size, this means that few marker beads were included within the correlation window and the search for a matching pattern in I_1 will fail. If the value of C is too large then we lose resolution because any small movements within the correlation window will be ignored when calculating the cross-correlation coefficient.

There are additional steps that are taken into consideration when obtaing the displacement field as local search implementation, sub-pixel resolution correcting correspondence failures and correcting for image registration artifacts. Detailed steps can be found in (75) and as a summary in appendix C.

3.5 The Fundamental Theory in Elastodynamics

In the previous section, we covered the method used to measure substrate deformation: optical flow registration algorithm (also see appendic C for details). Here, we cover the physics used to measure the traction forces from the recorded displacements of the fiduciary marker beads.

3.5.1 Mechanical Equilibrium

Let us consider a surface element in the shape of a tiny triangle with area vector $d\boldsymbol{S} = (dS_x, dS_y, dS_z)$. This triangle and its projections on the coordinate planes form together a body in the shape of a tetrahedron. Since we aim to prove the existence of the stress tensor, we cannot assume that it exists. What we know is that the forces acting from the inside of the tetrahedron on the three triangular faces in coordinate planes are vectors of the form $d\,\boldsymbol{F}_x = \boldsymbol{\sigma}_x dS_x,\ d\boldsymbol{F}_y = \boldsymbol{\sigma}_y dS_y$ and $d\boldsymbol{F}_z = \boldsymbol{\sigma}_z dS_z$. Denoting the force acting from the outside on the skew face by $d\boldsymbol{F}$, and adding a possible volume force $\boldsymbol{f}dV$, the equation of motion for the small tetrahedron becomes $dM\,\boldsymbol{w} = \boldsymbol{f}dV + d\boldsymbol{F} - \boldsymbol{\sigma}_x dS_x - \boldsymbol{\sigma}_y dS_y - \boldsymbol{\sigma}_z dS_z$, where $\boldsymbol{w}$ is the acceleration of the tetrahedron and $dM = \rho dV$ is its mass, which is assumed to be constant. The signs have been chosen in accordance with the inward direction of the area projection $dS_x,\ dS_y$ and dS_z. If we make the tetrahedron progressively smaller, the body force term and the acceleration term will vanish faster than the surface terms. In the limit of a truly infinitesimal tetrahedron, only the surface terms remain, so we end up with $dF = \boldsymbol{\sigma}_x dS_x + \boldsymbol{\sigma}_y dS_y + \boldsymbol{\sigma}_z dS_z$. This shows that the force acting on an arbitrary surface element may be written as a linear combination of three basic vectors, one for each coordinate axis. Using this *Cauchy's stress hypothesis*, the force can be written in matrix form:

$$d\boldsymbol{F} = \boldsymbol{\sigma} \cdot d\boldsymbol{S}. [3.17]$$

The nine elements of the stress tensor $\{\sigma_{ij}\}$ make up a single geometric object, which was first introduced by Cauchy in 1822, therefore using index notation, we can write it as

$$dF_i = \sum_j \sigma_{ij} d\, S_j. [3.18]$$

If we include a volume force density f_i, then the total force on a body of volume V with surface S becomes

$$F_i = \int_V f_i dV + \oint_S \sum_j \sigma_{ij} d\, S_j\,. [3.19]$$

Using Gauss' mathematical theorem ($\int_S p d\boldsymbol{S} = \int_V \nabla p dV;$ for an arbitrary function $p(\boldsymbol{x})$), the above can be written as a single volume integral

$$F_i = \int_V f_i^* dV, [3.20]$$

where

$$f_i^* = f_i + \sum_j \nabla_j \sigma_{ij}\,, [3.21]$$

is the *effective force density*. Now, in mechanical equilibrium, the total force on any body must vanish, for if it does not then the body will start to move. So the general condition here is that $\boldsymbol{F} = 0$ for all volumes *V*. Hence, we arrive at *Cauchy's equilibrium equation*,

$$f_i + \sum_j \nabla_j \sigma_{ij} = 0. [3.22]$$

In spite of its simplicity, these partial differential equations govern mechanical equilibrium in all kinds of continuous matter: solid, fluid or whatever.

3.5.2 Hooke's Law

Consider an ideal massless elastic spring obeying Hooke's law. If a relaxed spring of length L is fixed at one end and pulled in the other direction with a force F, its length is increased to $L + x$ (Fig. 3.5.2a); therefore, by Hooke's law,

$$F = kx, [3.23]$$

where k is the *spring constant*.

Real springs are physical bodies of mass, shape and internal molecular structure. Almost any solid material fixed at one end and pulled at the other, will behave like a spring, of course when the pull is not too strong. This means that the interatomic forces are approximately elastic when atoms are displaced slightly away from their original positions (Fig. 3.5.2a).

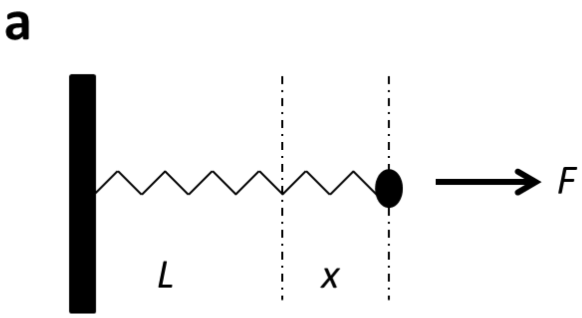

Figure 3.5.2a Hooke`s Law. A spring anchored at the left and pulled towards the right by a force F will be stretched by the amount $x = Fx$.

Here the force F, which is needed to extend the length of a real string by a small amount x must be proportional to the area, A, of the string cross-section. The reason being is that if we attempt to bundle N such strings roughly together to make a thicker string of area NA, the total force will have to be NF in order to get the same change in length. This means that the quantity we should use is not the force F but the normal stress or tension $\sigma_{xx} = \frac{NF}{NA} = \frac{F}{A}$. For a smaller piece of the string of length $L' < L$, the uniformity implies that it will be stretched proportionally less, $\frac{x'}{L'} = \frac{x}{L}$. This means that the absolute change of length x is not the parameter of interest but rather the relative longitudinal extension or strain $u_{xx} = x/L$..

Putting everything together, we get

$$E = \frac{stress}{strain} = \frac{\sigma_{xx}}{u_{xx}} = \frac{F/A}{x/L} = k\frac{L}{A}, [3.24]$$

where E, a material parameter is called the *Young's Modulus*.

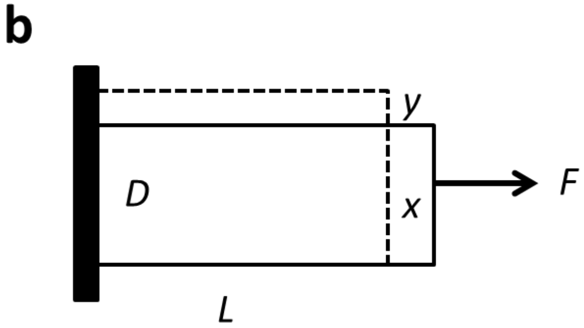

Figure 3.5.2b Possion`s ratio. A string normally contracts in the transverse directions when pulled at the ends.

Normal materials will contract in directions transverse to the direction of extension (Fig. 3.5.2b). If the transverse size, D of a string changes by y, the transverse strain becomes of the order $u_{yy} = y/D$, and will be negative for a positive stretching F. In linear materials, the transverse strain is also proportional to F. The negative of this ratio is called *Poisson's ratio*,

$$\nu = -\frac{u_{yy}}{u_{xx}}, [3.25]$$

another parameter characterizing isotropic materials.

To determine the form of the most general linear relationship between stress and strain in an isotropic material, we note that in such a material there are no internal directions which can be used to construct a linear relation between tensors σ_{ij} and u_{ij}. In that case only two tensors can appear in the relation: one is the strain tensor u_{ij} itself, another is the Kronecker delta δ_{ij} multiplied with the trace of the strain tensor $\sum_k u_{kk}$. This is the only possible factor, because the trace is the only scalar quantity that can be formed from a linear combination of the strain tensor components. Therefore, we conclude the most general strictly linear relation between stress and strain tensors in an isotropic material to be

$$\sigma_{ij} = 2\mu u_{ij} + \lambda\delta_{ij}\sum_k u_{kk}\,, [3.26]$$

which is the general representation of Hooke's law for arbitrary isotropic materials. The coefficients λ and μ are material constants, called *elastic moduli* or *Lamé coefficients*. The coefficient λ has no special name, whereas μ is called shear modulus, since it controls the magnitude of shear (off-diagonal) stresses. The *Lamé coefficients* are directly related to the elasticity and Poisson's ratio.

3.5.3 Strain Tensor

Under the action of applied forces, solid bodies exhibit deformation to some extent, for example they can change in shape and volume. The deformation of a body has been described mathematically elsewhere (76), so only the end result is presented for the general strain tensor is,

$$u_{ij} = \frac{1}{2}\left(\nabla_i u_j + \nabla_j u_i + \sum_k \nabla_i u_k \nabla_j u_k\right). [3.27]$$

The strain tensor contains all the information about geometric changes in the displacement. It must, however, be emphasized that the above strain tensor for finite deformations can be simplified into an expression valid only for small displacement gradients. Thus for small displacements, the strain tensor becomes:

$$u_{ij} = \frac{1}{2}\left(\nabla_i u_j + \nabla_j u_i\right). [3.28]$$

3.5.4 Equilibrium Equation of an Elastic Medium Bounded by a Plane

By inverting Hooke's law and Cauchy's strain tensor into the effective force we get,

$$f_i^* = f_i + 2\mu \sum_j \nabla_j u_{ij} + \lambda \nabla_i \sum_j \mathrm{u}_{jj}$$

$$= f_i + \mu \sum_j \nabla_j^2 u_i + (\lambda + \mu)\nabla_i \sum_j \nabla_\mathrm{j} \mathrm{u}_j \;\; [3.29]$$

Rewriting this in vector notation, we arrive at the *Navier's equation of equilibrium*, also called the *Navier-Cauchy equilibrium equation*,

$$\boldsymbol{f} + (\lambda + \mu)\nabla\left(\nabla \cdot \boldsymbol{u}(\boldsymbol{x})\right) + \mu \boldsymbol{\nabla}^{\mathbf{2}} \boldsymbol{u}(\boldsymbol{x}) = 0. [3.30]$$

In mechanical equilibrium, the total force on any body must vanish, for if it does not then the body will start to move ($\boldsymbol{f} = 0$) for all volumes *V*, hence the above equation of equilibrium becomes:

$$(\lambda + \mu)\nabla\left(\nabla \cdot \boldsymbol{u}(\boldsymbol{x})\right) + \mu \boldsymbol{\nabla}^{\mathbf{2}} \boldsymbol{u}(\boldsymbol{x}) = 0, [3.31]$$

where $\boldsymbol{u}(\boldsymbol{x})$ is the three-dimensional displacement vector and ν is the Poission's ratio of linearly elastic material.

3.6 Measuring Traction Force Microscopy (TFM)

Traction Force Microscopy (TFM) is the most wide-spread technique for investigating cellular traction forces (67, 77, 78). This method measures the surface displacement with either a single particle or optical flow based approach between two successive images. In most studies submicron fluorescent fidicuary beads (200 nm in diameter) are embedded in polyacrylamide or similar polymer based substrates with typical elasticities ranging from ~ 1-100 kPa (68). To record cell surface deformations, cells are initially seeded on the substrate material and allowed to spread and migrate. After some time, a first image is recorded via optical microscope, where paired fluorescence and phase image is recorded. Typically, this contains both the cell of interest and the fluorescent beads, which are recorded simultaneously. For absolute measurement, the cells are detached from the surface involving cleaving proteases as trypsin or calcium release as EDTA to disrupt all cell-substrate attachments, Without moving the microscope stage another image is captured serving as the reference image (‘*null image*’). The two-dimensional full-field displacements are then determined from the set of the two images by using the optical flow registration algorithm developed by Micah Dembo (LIBTRC) and discussed in depth in section 3.4.1 and appendix C, (67, 79).

In order to determine the cell-induced surface traction forces from the recorded displacement data, the Boussinesq formulation is utilized. The Boussinesq theory describes the displacement equilibrium solutions for an isotropic elastic material bounded on one side by an infinite plane with applied forces at its free boundary (surface) via equilibrium equation [3.31].

The details of the derivation in formulating the solution is given by Landau and Lifshitz (76), as only the end result is presented here. The displacement field $\boldsymbol{u}(\boldsymbol{x})$ in the semi-infinite half-space at a given position p, $\boldsymbol{u}_{p\alpha}$ as a result of traction stresse $P_\beta(r)$ exerted over the surface may be expressed as:

$$u_{p\alpha} = \iint G_{\beta\alpha}(\boldsymbol{m}_p - \boldsymbol{r})P_\beta(\boldsymbol{r})dr_1 dr_2, \text{[3.32]}$$

where α and β denote the directions along the Cartesian axes, $\boldsymbol{m}_p$ denotes the position vector at p and the surface forces $P_\beta(\boldsymbol{r})$ at a location $\boldsymbol{r}$ is expressed as

$$P_\beta = F\delta(r_1)\delta(r_2), \text{[3.33]}$$

where F is the concentrated surface force. The integration is confined within the spread area of the cell, since the traction forces were exerted only at cell-substrate contact points. The nine functions,$G_{\beta\alpha}(\boldsymbol{m}-\boldsymbol{r})$, derived by Boussinesq, define the displacement of the substrate in the direction α at location $\boldsymbol{m}$, in response to a concentrated force acting at location $\boldsymbol{r}$ and in the direction β. The thickness of the gelatine-based substrates for this analysis is assumed to be infinite as compared to the maximal displacement of the fiduciary marker beads. The actual equations are as follows:

$$G_{11} = \frac{1+\nu}{2\pi E}\left(\frac{2(1-\nu)r - x_3)}{r(r-x_3)} + \frac{(2r(\nu r - x_3) + x_3^2)x_1^2}{r^3(r-x_3)^2}\right) \; [3.34a]$$

$$G_{21} = G_{12} = \frac{1+\nu}{2\pi E}\left(\frac{((2r(\nu r - x_3) + x_3^2)x_1 x_2)}{r^3(r-x_3)^2}\right) \; [3.34b]$$

$$G_{31} = G_{13} = \frac{1+\nu}{2\pi E}\left(\frac{x_1 x_3}{r^3} + \frac{(1-2\nu)x_1}{r(r-x_3)}\right) \; [3.34c]$$

$$G_{22} = \frac{1+\nu}{2\pi E}\left(\frac{2(1-\nu)r - x_3)}{r(r-x_3)} + \frac{(2(\nu r - x_3) + x_3^2)x_2^2}{r^3(r-x_3)^2}\right) \; [3.34d]$$

$$G_{23} = G_{32} = \frac{1+\nu}{2\pi E}\left(\frac{x_2 x_3}{r^3} + \frac{(1-2\nu)x_2}{r(r-x_3)}\right) \; [3.34e]$$

$$G_{33} = \frac{1+\nu}{2\pi E}\left(\frac{2(1-\nu)}{r} + \frac{x_3^2}{r^3}\right) \; [3.34f]$$

The Boussinesq theory predicts that at or near the surface of an incompressible substrate $(\nu = 0.5)$, there is negligible coupling of the in-plane displacements to the out of plane tractions.

A maximum likelihood analysis is then applied to calculate the resulting traction forces. To begin this analysis, the cell is first descretized by dividing into quadrilaterals with the use of an algorithm (LIBTRC). The values of the *x* and *y* components of the traction force at each node of this mesh is then determined by maximizing the total Bayesian likelihood of the predicted marker displacements, defined as $exp[-(\chi^2 + \lambda C^2)]$, in conjunction with the following constraints:

1. There can be no forces outside the cell boundary.

2. There can be no net force.
3. There can be no net torque.
4. Finally, there must be minimal complexity.

In the equation χ^2 measures the deviation of the calculated substrate displacement from the actual measurement, while C^2denotes the complexity of the given traction map, and λ is an empirical parameter. Beginning with $\lambda = 0$ followed by progressively larger values of λ, the distribution of the traction stresses that maximizes the Bayesian likelihood is determined. As λ increases, the relative weight of complexity in determining the likelihood increases while the relative weight of deviation, as reflected by χ^2, decreases. This eventually leads to a threshold point where the deviation becomes unacceptably large. The traction stress distribution just before this point represents the distribution of the minimal complexity that satisfies the Boussinesq equations with an acceptable error.

An alternative measurement to determine the traction forces is known as the Fourier Transform Traction Cytometry (FTTC) (80). Instead of dealing with fluorescent microbeads directly, the Boundary Element Method (BEM) explained in sections 3.4 to 3.6 and appendix C, and the FTTC rely on the similarity in area contrast between a pair of images to identify substrate deformation. In the FTTC technique, the optical flow is constructed not on a pixel basis, but rather in an average sense of a small window. For instance, on a 1024x1024 pixel image, the typical window size used is 64x64 pixels. Butler et al. (80) divided each image into overlapped windows with a constant distance, such as 16 pixels, between successive windows. One window in the ‘unstrained’ image is matched to that in the ‘strained’ image provided that these two windows give the highest cross-correlation. The FTTC method like the method described above also starts by using a grid on the ‘unstrained’ image in order to estimate the movement of these grid points.

The main advantage of the BEM over the FTTC approach is that the former is more flexible, as the displacement is not restricted to be between two fixed windows. Moreover, the difference between FTTC and BEM lies in the method of calculating the generated traction forces exerted by cells on deformable substrates. Butler et al. (80) make use of the property that through a Fourier Transform (FT), a convolution equation becomes a simple multiplication. A traction force is obtained in three steps. Initially the FT is carried out on the displacement field. Second, the FT of the traction force at each wave number is obtained. And finally, an inverse FT operation on the whole field is carried out, which gives the traction forces. Therefore, Butler et al. developed an approach for performing the inverse calculations in Fourier space and they noted that the Fourier transform of the Green's tensor is diagonal and invertible without regularization to the problem as in the BEM (80). Moreover, the group was able to tackle the problem successfully without explicit regularization. Their approaches dictate that both the forces and displacements be set on grids or meshes, which can be viewed as an implicit form of regularization since the high frequency components have been truncated and thus limits the level of perturbation in traction forces due to noises. Therefore, the main disadvantage of the BEM is that it performs an explicit regularization, which comes with a higher computational cost, however one gains more control with the ability to impose effects of noises.

The BEM approach was used for measuring the traction force data throughout this thesis primarily because it was already well-documented and more importantly it was open to the public. In addition, it contains an extremely user-friendly interface with an available manual; whereas the FTTC does not.

3.7 Chapter Conclusion

In this chapter, the major tool as the AFM was introduced to reader. This was followed by an in-depth description of the theoretical basis for measuring the deformations of the elastic substrates and calculating the generated traction forces exerted by cells on deformable substrates. The next three chapters describe three chapters describe in detail the thre e major studies.

Chapter Four: Cross Talk between Nanoscale Forces and Substrate Nanomechanics Influence Cellular Traction Dynamics

The material in chapter six has been published in Physical Biology ("Cross talk between matrix elasticity and mechanical force regulates myoblast traction dynamics” by Z. Al-Rekabi and A.E. Pelling *Phys. Biol*. **10**, 066003 (2013)).

Abstract

Growing evidence suggests that critical cellular processes are profoundly influenced by the cross talk between extracellular nanomechanical forces and the material properties of the cellular microenvironment. Although many studies have examined either the affect of nanomechanical forces or the material properties of the microenvironment on biological processes, few have investigated the influence of both. Here, we performed simultaneous atomic force microscopy (AFM) and traction force microscopy to demonstrate that muscle precursor cells (myoblasts) rapidly generate a significant increase in traction when stimulated with a local 10 nN force. Cells were cultured and nanomechanically stimulated on hydrogel substrates with controllable local elastic moduli varying from ~16-89 kPa, as confirmed with atomic force microscopy. Importantly, cellular traction dynamics in response to nanomechanical stimulation only occurred on substrates that were similar to the elasticity of working muscle tissue (~64-89 kPa) as opposed to substrates mimicking resting tissue (~16-51 kPa). The traction response was also transient, occurring within 30 seconds, and dissipating by 60 seconds, during constant nanomechanical stimulation. The observed biophysical dynamics are very much dependent on rho-kinase and myosin-II activity and likely contribute to the physiology of these cells. Our results demonstrate the fundamental ability of cells to integrate nanoscale information in the cellular microenvironment, such as nanomechanical forces and substrate mechanics, during the process of mechanotransduction.

4.1 Introduction

The complex cellular microenvironment gives rise to many dynamic and time-variant physical and biochemical cues, which ultimately regulate a multitude of biological processes (25, 27, 81-85). In-vivo, extracellular mechanical forces as well as the physical properties of the extracellular matrix (ECM) both influence cellular physiology. The conversion of this physical information into a cellular response is now understood to be critical in many biologically relevant pathways (25, 27, 81). Extracellular nanoscale forces (~0.01 – 100 nN) have been shown to influence numerous signalling pathways both in-vivo and in-vitro (35, 36, 86-96). Such nanoscale forces can arise through stretch/compression of the microenvironment, fluid shear stress or localized forces occurring at adhesion sites, which have been shown to result in cytoskeletal remodelling, changes in cellular orientation and alignment, alterations in gene regulation and determining cell fate (35, 36, 86-96). Therefore it is important to understand how physical forces are generated and transmitted through living cells. In recent years, the atomic force microscope (AFM) has emerged as one important tool for investigating how cells regulate their nanomechanical properties and respond to nanomechanical stimuli (97-99). The AFM has been employed to quantify the local nanomechanical properties of living cells and demonstrate their intimate link to numerous physiological and pathological processes (99-105).

It is also now evident that substrate elasticity has a significant influence on many physiological and pathological processes (81-85). Cells sense substrate elasticity by physical probing of the microenvironment through the interplay of actomyosin contractility and focal adhesion/integrin dynamics. This gives rise to traction forces, which are key indicators of cellular responses to substrate elasticity and physical stimulation (83, 85). Therefore, cells display an exquisite ability to integrate diverse physical cues (including but not limited to nanomechanical forces and material properties) during the regulation of numerous physiological pathways. In-vivo, the cellular microenvironment is highly dynamic, possessing physical properties that can also vary in time. It has also been demonstrated that gradual and sudden changes in microenvironment elasticity has a significant impact on the development and maturation of embryonic cardiomyocytes and during the differentiation of human mesenchymal stem cells (106, 107).

Muscle contractions are ubiquitous in-vivo and simultaneously produce physical forces and changes in the local mechanical properties of the microenvironment. When muscle tissue transitions from a resting to a contracted state, it exhibits an ~8 fold increase in elasticity (14-19). During contraction, muscle satellite/myoblast cells are exposed to physical forces, and changes in microenvironment elasticity, which induces their activation and eventual fusion into myotubes (myogenesis) (14, 20-24). While mechanical stretch has been shown to induce remodelling of the cytoskeleton, myoblasts are able to maintain a significant amount of adhesion and contract with the microenvironment during large-scale cytoskeletal depolymerisation (108). The results suggest that myoblasts generate a significant amount of traction in-vivo. A model cell line employed to study the effects of mechanical stimuli on myogenic differentiation are C2C12 mouse myoblasts. These cells readily form contractile myotubes and mechanical stimulation drives changes in gene expression, proliferation, fusion and differentiation (20-24). Traction forces generated by C2C12 cells vary significantly during myotube formation and differentiation (14, 109, 110) and myogenesis proceeds optimally on substrates that mimic the elasticity of resting muscle tissue (~12 kPa) (14). Conversely, the onset of the early myogenic process occurs during physical activity in working muscle tissue that has a higher elasticity (~38-97 kPa) than resting tissue (15-19). Therefore, the early and late myogenic processes, which can be separated by a period of days (111, 112), are clearly sensitive to, and dependent on, large differences in microenvironment elasticity.

In this study, we hypothesized that myoblasts will generate an increase in traction forces in response to nanomechanical stimulation only in a microenvironment that mimics contracted muscle tissue. Therefore, our objectives were to combine atomic force microscopy (AFM) and traction force microscopy (TFM) to directly measure the generation of traction forces by myoblasts in response to changes in substrate elasticity and controlled nanomechanical stimulation. We examined the cross talk between changes in local substrate nanomechanics, nanomechanical stimulation and the regulation of muscle myoblast traction dynamics. Biocompatible gelatine substrates were produced with five distinct elastic moduli (~16, ~24, ~51, ~64 and ~89 kPa) as confirmed with AFM-based nanomechanical analysis and force-volume imaging. These nanomechanical properties were chosen in order to mimic the elasticity of resting (~12-39 kPa) to active (~38-97 kPa) mouse muscle tissue (14-19). The results demonstrate that mouse C2C12 myoblasts generate a dramatic increase in traction due to direct nanomechanical stimulation on substrates mimicking highly active muscle. The response was also transient, a large increase in traction arising within 30 secs but dissipating to baseline levels by 60 secs. Conversely, on softer substrates, no significant increase in traction force was observed in response to a nanomechanical stimulus. The inhibition of rho-dependent kinase (ROCK) and myosin-II impeded traction dynamics in response to mechanical stimulation altogether (83). Here, we have investigated a model system that mimics some characteristics of the mechanical dynamics arising in muscle tissue. The results reveal that C2C12 myoblasts only respond to a physical force in a stiff microenvironment. Moreover, their response is highly transient in nature. Therefore, myoblasts appear to be able to modulate their response to physical stimulation by integrating information arising from both the material properties of the microenvironment and extracellular nanomechanical forces.

4.2 Materials and Methods

4.2.1 Preparation of Glutaraldehyde Cross-Linked Gelatine (GXG) Substrates.

A sterile solution of Porcine Type-A Gelatine (GE) (Sigma-Aldrich) was made by autoclaving 3-7% GE in distilled water. A 1:200 dilution of 200 nm of fluorescent beads (Invitrogen) was added to 1mL GE and this was cross-linked with 50% Glutaraldehyde (Sigma-Aldrich) (GA) to a final concentration of 0.5%. 1ml of solution was spread evenly over the surface of a 35 mm plastic culture dish. Dishes were placed in a humidity chamber and stored in the refrigerator overnight. The next morning, any unreacted GA was then reduced with $NaBH_4$ (1 mg/mL in ice cold phosphate Buffer Saline (PBS) made immediately before use) for 1hr on ice. Plates were then rinsed with cold PBS, UV sterilized for 1 min (Spectroline UV Crosslinker Select Series) and then filled with culture media. The plates were stored in the tissue culture incubator for 4hrs prior to seeding cells and were used the next day for experiments. In some cases cells were cultured directly on 0.1% GE coated plastic dishes in order to compare their morphology and responses on a hard substrate to the data obtained on the more compliant GXG substrates.

4.2.2 Cell Culture, Staining and Imaging.

C2C12 mouse myoblast cells were maintained in a 37°C, 5% CO_2 incubator and cultured in DMEM with 10% fetal bovine serum (FBS) and 1% streptomycin/penicillin (all from Hyclone Laboratories Inc.). Experiments were performed 24 hrs after cells were plated on 3-7% GXG substrates with cell density of ~10^5 cells/cm^2. Y27632 and blebbistatin (Sigma) were stored as stock solutions in DMSO at -20ºC. Inhibition of ROCK or myosin-II was achieved by exposing cells to Y27632 (20 µM, final concentration) or blebbistatin (10 µM, final concentration) for 30min prior to experimentation respectively. Immunofluorescence staining was carried out as previously described (113) but with some small modifications. Briefly, cells cultured on GXG substrates were fixed with 3.5% paraformaldehyde and permeabilized with 0.5% Triton X-100. Cells were then quenched in 0.15M Glycine for 25 min. Actin filaments were stained with Phalloidin Alexa Fluor 488 (Invitrogen), and the nuclei stained with DAPI (Invitrogen). In some cases vinculin was labelled with a monoclonal anti-vinculin primary antibody produced in mouse (Invitrogen) and a rabbit anti-mouse IgG secondary (Invitrogen) antibody conjugated to AlexaFluor 488 fluorophore (each used at a 1:500 dilution). For experiments using vinculin, actin filaments were stained with Phalloidin Alexa Fluor 546 (Invitrogen). Following each step cells were incubated with wash buffer for 15 min (5% Horse Serum (Sigma)) in PBS. Imaging was carried out on an A1R resonant scanner confocal microscope using 60X water objective (Nikon, Canada). Confocal images were analyzed using ImageJ and are presented as maximum intensity z-projections and brightness/contrast settings were optimized to maximize fluorophore signal.

4.2.3 Atomic Force Microscopy.

An AFM (Nanowizard II, JPK Instruments, Germany) was used for all experiments with PNP-TR-50 cantilevers (Nanoworld) with spring constants of 69 ± 6 pN/nm. In order to determine the local elasticity of the cells and GXG substrates, force curves were measured at 1Hz and analyzed with the Hertz Model (114) for an indentation of 200 nm. For each GXG substrate, n = 3 plates were created and 5-15 force curves were collected at 25 random locations on each plate. In a similar manner, cell elasticity was determined by culturing cells on n = 3 plates of each GXG substrate. 24 cells were randomly chosen and 5-15 force curves were collected on each cell (over the centre of the nucleus) until 100 force curves in total were acquired. In some cases, force-volume elasticity maps of the GXG substrates were acquired in the ‘force mapping’ mode. Force curves were acquired over a 32 x 32 pixel scan area and the Young’s modulus determined as described above.

4.2.4 Atomic and Traction Force Microscopy.

Simultaneous AFM and TFM measurements were performed by mounting the AFM on a Nikon Eclipse TiE epi-fluorescence and phase contrast microscope (Nikon, Canada). TFM was performed by capturing paired phase contrast and fluorescence images (of the cell and the bead positions respectively) every 30 sec for 120 sec with a CCD camera (Photometric Cool Snap HQ^2) and a 40X, NA 0.65 objective lens. For the absolute traction measurements, the null image was obtained by removing the cell from the substrate with 10 mM EDTA. EDTA was dissolved in PBS without Ca^{2+} and Mg^{2+}, the pH was brought down to 7-8 by adding 0.02 M Acetic acid. For the differential traction measurements, TFM imaging was first carried out on a cell of interest without any mechanical stimulation (control), followed by imaging during a constant applied force (10nN) with the AFM tip directly on the centre of the cell nucleus (mechanically stimulated cells). Therefore, every cell measured possessed a built-in control. Cells were maintained at 37°C with a microscope stage petri dish heater (JPK Instruments). Tracking and registration was carried out with the well-described and commonly employed optical flow registration algorithms and LIBTRC libraries (kindly provided by Micah Dembo, Boston University) (67, 115). Traction heat maps were then generated using Origin 8.5.

4.2.5 Quantification of Focal Adhesion and Cell Size.

The average focal adhesion size was quantified for untreated cells and ROCK or myosin-II inhibited cells. After culturing cells on 3%, 7% GXG and 0.1% GE coated plastic, cells were fixed, stained and imaged with a confocal microscope for the focal adhesion protein vinculin, as described above. Post-processing was carried out in ImageJ, where FA and cell areas were segmented using available ImageJ plugins.

4.2.6 Statistical Analysis.

All values are presented as the average ± s.e.m. A one-way ANOVA test, Levene's test for equal variance, Tukey test for means comparison (significantly different or not) and two-sample t-test ($P<0.05$) were performed.

4.3 Results

4.3.1 Hydrogels with tuneable elasticity for traction force measurements.

C2C12 mouse myoblast cells were cultured on biocompatible glutaraldehyde cross-linked gelatine (GXG) substrates embedded with 200 nm fluorescent beads as fiduciary markers (Fig. 6.3.1-3a & b) similar to those that have been used previously (116). Although polyacrylamide (PA) is typically employed in TFM studies, methacrylated hyaluronic acid, gelatin and silicone have all been utilized with much success (116-119). The GXG substrates we fabricated were 500 µm thick and optically clear allowing for simultaneous phase/fluorescence imaging and AFM (Fig. 6.3.1-1a & b). Five GXG substrates were produced with an increasing amount of gelatine (3-7% w/v). We characterized the local nanomechanical properties of each gel with AFM and determined that increasing the gelatine content of each hydrogel resulted in a corresponding increase in local nanomechancial elasticity from ~16-89 kPa (Fig. 6.3.1-1c). The elasticity of the GXG substrates was tuned to mimic resting (~12-39 kPa) to active (~38-97 kPa) muscle tissue in mice (14-19). AFM force-volume imaging also revealed that the nanomechanical properties of the GXG substrates were spatially homogeneous (Fig. 6.3.1-1d & e) and mechanical loading of gels revealed a linear response to forces for small deformations (Fig. 6.3.1-2).

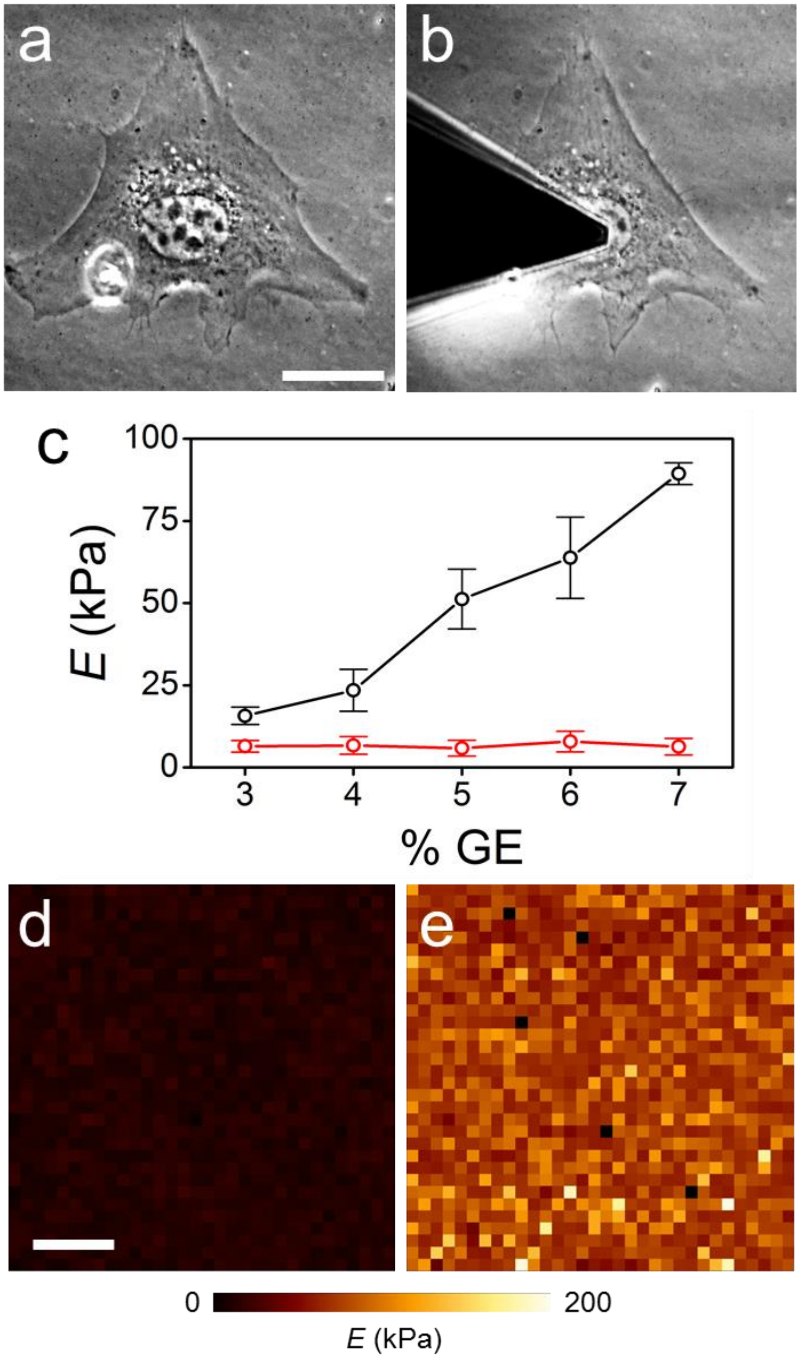

Figure 4.3.1-1: C2C12 cells cultured on tuneable hydrogels for simultaneous AFM and TFM measurements. (a) Phase contrast image of a C2C12 cell on 63.8 ± 0.534 kPa GXG substrate before nanomechanical stimulation (scale bar = 21 µm and applies to (b)), and (b) the same cell shown with an AFM tip pushing on the nucleus with a constant 10nN force. (c) C2C12 cells were seeded on five GXG substrates that were produced with an increasing amount of gelatin (3-7% w/v) allowing us to control the elasticity from ~16-89 kPa (black circles). However, the nanomechanical properties of the cell were not affected by increasing substrate elasticity and remained relatively constant at 6.65 ± 0.340 kPa (red circles). AFM force-volume

elasticity maps of (d) a soft GXG substrate (15.7 ± 2.66 kPa) and (e) a stiff GXG substrate (89.4 ± 0.679 kPa) revealed that the local nanomechanical properties of the GXG hydrogels were spatially homogeneous (scale bar = 2μm and applies to both).

Taken together, the results reveal that the GXG substrates have spatially uniform nanomechanical properties and that the average values are a good estimate of the global elasticity of the substrate. Therefore, the GXG substrates allowed us to culture C2C12 cells on substrates of varying elasticity while examining their response to nanomechanical stimuli delivered with an AFM. Finally, the local nanomechanical properties of the cells were found to be constant at 6.65 ± 0.340 kPa on all GXG hydrogels (Fig. 4.3.1-1). Importantly, many cell types have been observed to generate measurable traction forces on substrates possessing a wide range of elasticities. For example, traction forces generated by NIH3T3 fibroblasts have shown to exert ~1 kPa of traction on relatively stiff substrates (30 kPa) (77). Moreover, stem cell derived cardiomyocytes have been demonstrated to generate greater contractility on stiffer substrates (~100 kPa) than those on soft substrates (~5 kPa), (120).

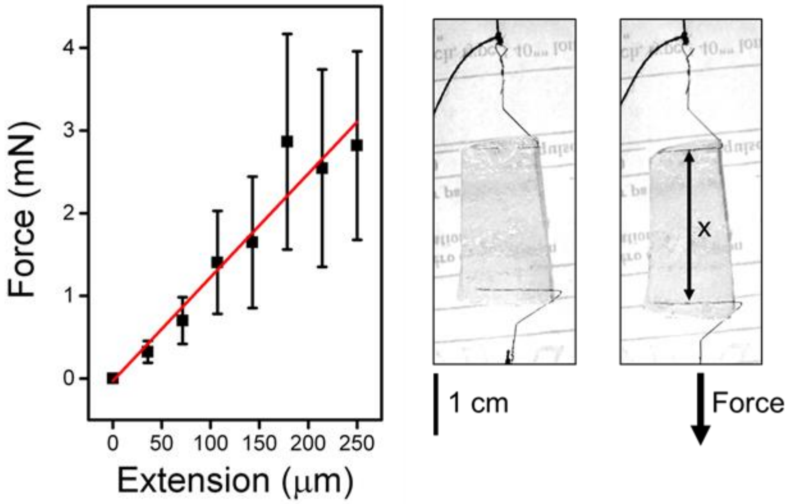

Figure 4.3.1-2 Further mechanical characterization of the GXG hydrogels. (a) A 51.2 ± 0.419 kPa GXG gel was suspended with hooks and subjected to mechanical loading producing small extensions up to 250 μm. Pre-weighed microcentrifuge tubes containing increasing amounts of water were placed on the lower hook to produce a constant downward force. The data reveals a relatively linear response to an applied force. Photos of the hydrogel (b) before and (c) after loading. The extension (x) of the gel was determined by measuring the distance between the hooks.

We found that cells grew normally and possessed similar morphological traits to cells grown on standard plastic culture dishes, such as well-defined actin stress-fibre morphology (Fig. 4.3.1-3a) Therefore, using GXG substrates, both absolute and differential TFM measurements were carried out (67, 121, 122). An absolute TFM measurement requires cells to be removed from the substrate, allowing the hydrogel to relax to an unstressed state in order to determine the total absolute traction force exerted by the cell. In a differential measurement, two subsequent images of fluorescent bead positions are acquired allowing one to calculate the change in traction force over a given time interval. Here, after a cell was chosen for study, a paired phase contrast and fluorescence image was immediately acquired and then again every 30 sec for 120 sec. This procedure was then repeated, however immediately following the initial image acquisition, the cell was exposed to a constant 10 nN force for the duration of the measurement (120 sec) delivered with an AFM cantilever. Therefore, in every case, basal and nanomechanically stimulated traction force dynamics could be compared for each cell. Following the absolute measurement (control and stimulated), the cell was dissociated from the substrate and each time point (30, 60, 90 and 120 sec) was compared to the relaxed bead positions to calculate the absolute cellular traction. In the case of a differential measurement, each time point was compared to the image at 0sec, allowing us to calculate the average change in traction, relative to an initial basal traction. Moreover, as the differential approach does not require the removal of a cell from a substrate, more cells in a sample can be examined. Generally, absolute TFM reveals a smooth traction field with many vectors pointing towards the cell centroid (67, 121) indicating the contractile nature of the cell (Fig. 4.3.1-3b). Differential TFM reveals the change in traction and yields important information about the temporal fluctuation of local traction dynamics (Fig. 4.3.1-3c).

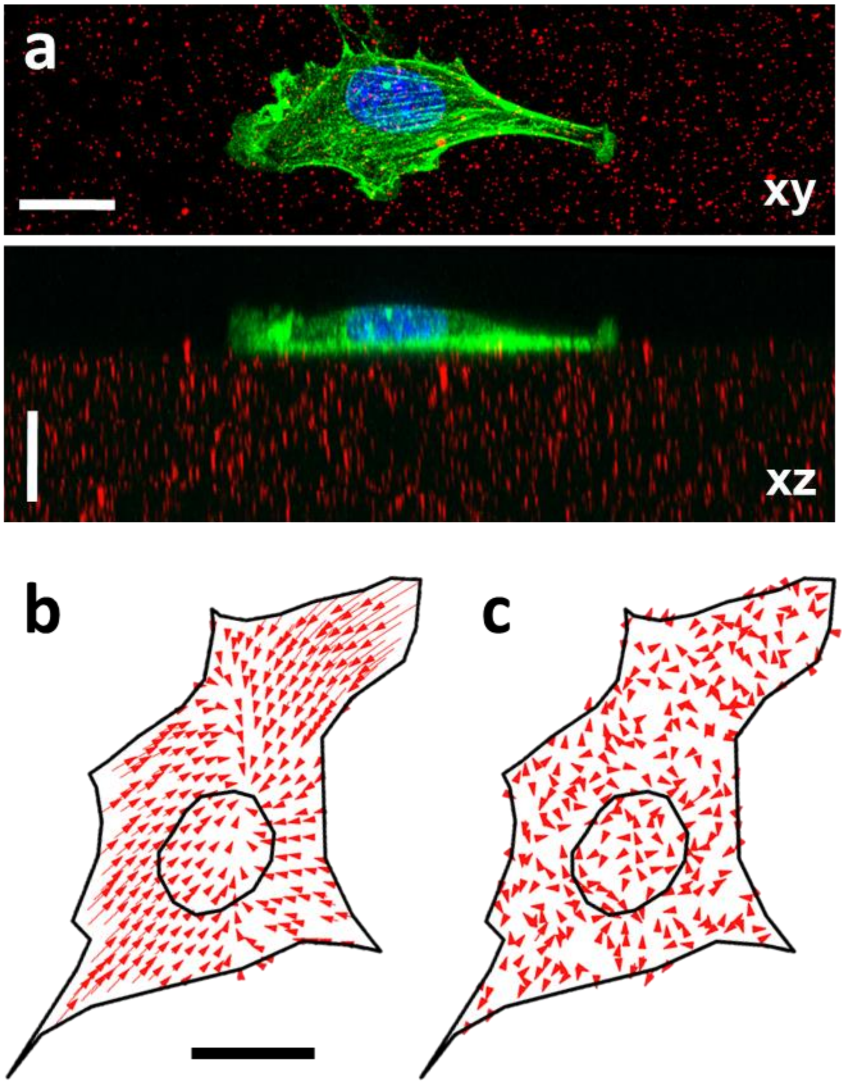

Figure 4.3.1-3: Absolute and differential traction force microscopy of C2C12 cells. (a) An XY maximum intensity projection (top, scale bar = 20 µm) and XZ orthogonal view along the long axis (bottom, scale bar = 15µm) of a fixed and stained C2C12 cell imaged with confocal microscopy on a 63.8 ± 0.534 kPa substrate (fluorescent beads (red), actin (green) and DNA (blue)). (b) For absolute TFM measurements, cells reveal a smooth traction field with many vectors pointing towards the cell centroid, indicating the contractile nature of the cell (scale bar = 30 µm and applied to (c)). (c) A 30sec differential image of the same cell reveals the change in traction over this timescale can be spatially heterogeneous.

4.3.2 Absolute traction force dynamics in mechanically stimulated cells.

To examine the change in traction in response to externally applied nanomechanical forces, samples were mounted on an inverted fluorescence/phase-contrast microscope equipped with an AFM. This allowed us to simultaneously apply a nanomechanical force to a cell while measuring absolute and differential traction dynamics. In all cases, the AFM tip was aligned over the centre of the nucleus, which generally approximates the cell centroid in non-migrating, interphase cells (114). After processing the data, an average absolute cellular traction was calculated for each interval of time (n = 9 - 15 cells for each substrate elasticity, Table 1).

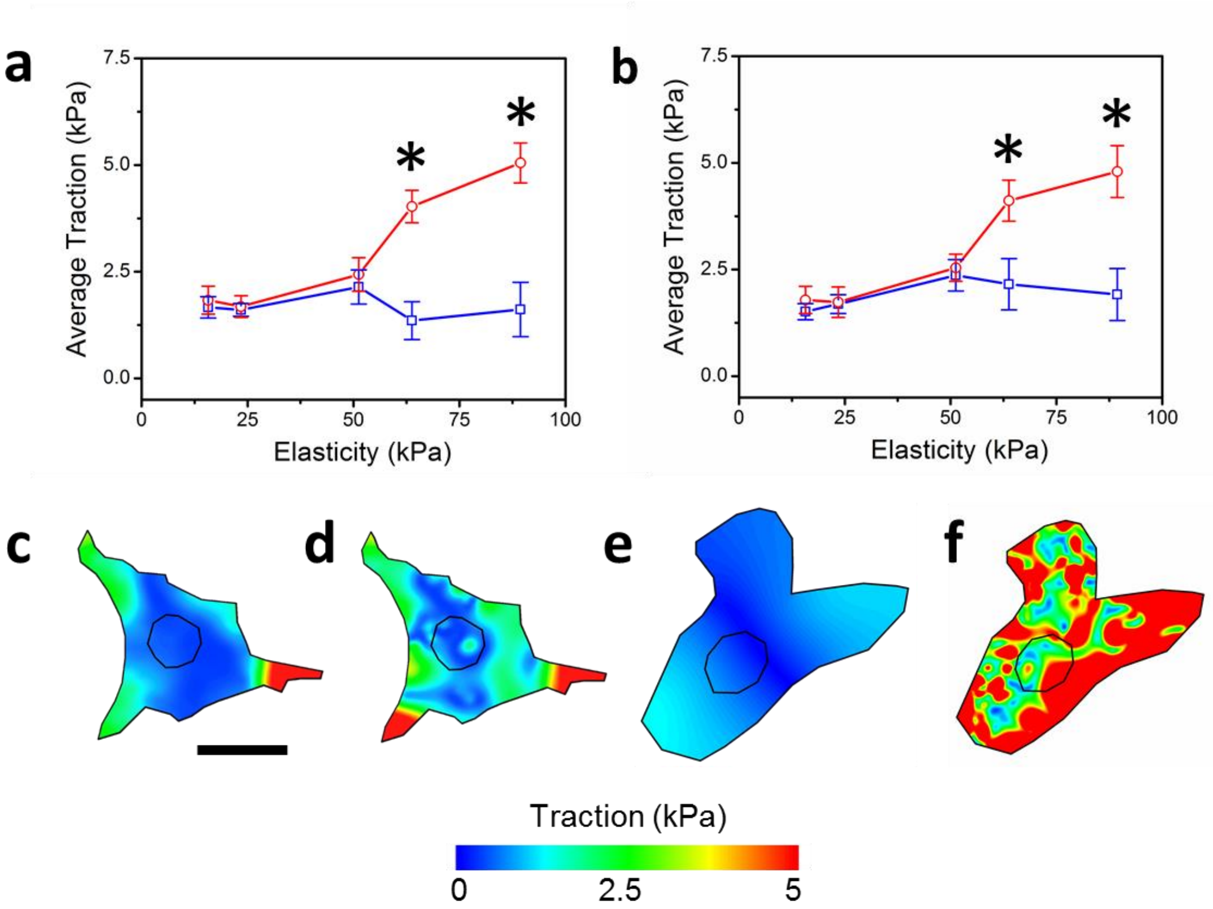

Figure 4.3.2-1: Absolute traction force dynamics on tuneable hydrogels in response to local nanomechanical stimulation. (a) The average absolute traction after 30 sec of nanomechanical stimulation as a function of substrate elasticity: blue squares (control) and red circles (10 nN). Cells clearly display an increase in traction over controls when exposed to a 10 nN force on substrates with an elasticity of 63.8 ± 0.534 kPa (P = 0.00271) and 89.4 ± 0.679 kPa (P = 0.00386). (b) The increase in traction is constant at all other time points during the measurement as shown here at the 120 sec time point (63.8 ± 0.534 kPa (P = 0.01913) and 89.4 ±

0.679 kPa (P = 0.00394)). Heat maps for a representative (c) control cell on a 15.7 ± 2.66 kPa (scale bar = 30 µm and applies to all) and (d) the same cell when exposed to a constant 10 nN force for 30 sec. Heat maps for a representative (e) control cell on a 89.4 ± 0.679 kPa substrate and (f) the same cell when exposed to a constant 10 nN force for 30 sec. A significant increase on traction is observed concomitantly with the appearance of local traction hotspots throughout the contact area. Importantly, this significant change in traction only occurred on the stiff substrates. All values are average ± s.e.m.

What becomes evident is that cells clearly display an increase in traction when exposed to a 10 nN force but only on GXG substrates with an elasticity of 63.8 ± 0.534 kPa (P = 0.00271) and 89.4 ± 0.679 kPa (P = 0.00386) (Fig. 6.3.2-1a). Moreover, the overall absolute increase in traction is significant within 30 sec and remains constant at the other time points during the stimulation (Fig. 4.3.2-1b). Heat maps of cells on 15.7 ± 2.66 kPa (Fig. 4.3.2-1c & d) and 89.4 ± 0.679 kPa (Fig. 4.3.2-1e & f) substrates reveal a relatively smooth traction field for control cells (67, 121). The application of a nanomechanical force to cells on the 63.8 ± 0.534 kPa and 89.4 ± 0.679 kPa substrates caused a significant increase in the magnitude of local traction vectors (Fig. 4.3.2-2) leading to the increase in average traction for the whole cell. The specific heat maps shown in fig. 4.3.2-1c-f present two specific cells from the absolute traction study and are only shown as representatives of all cells examined (Table1).

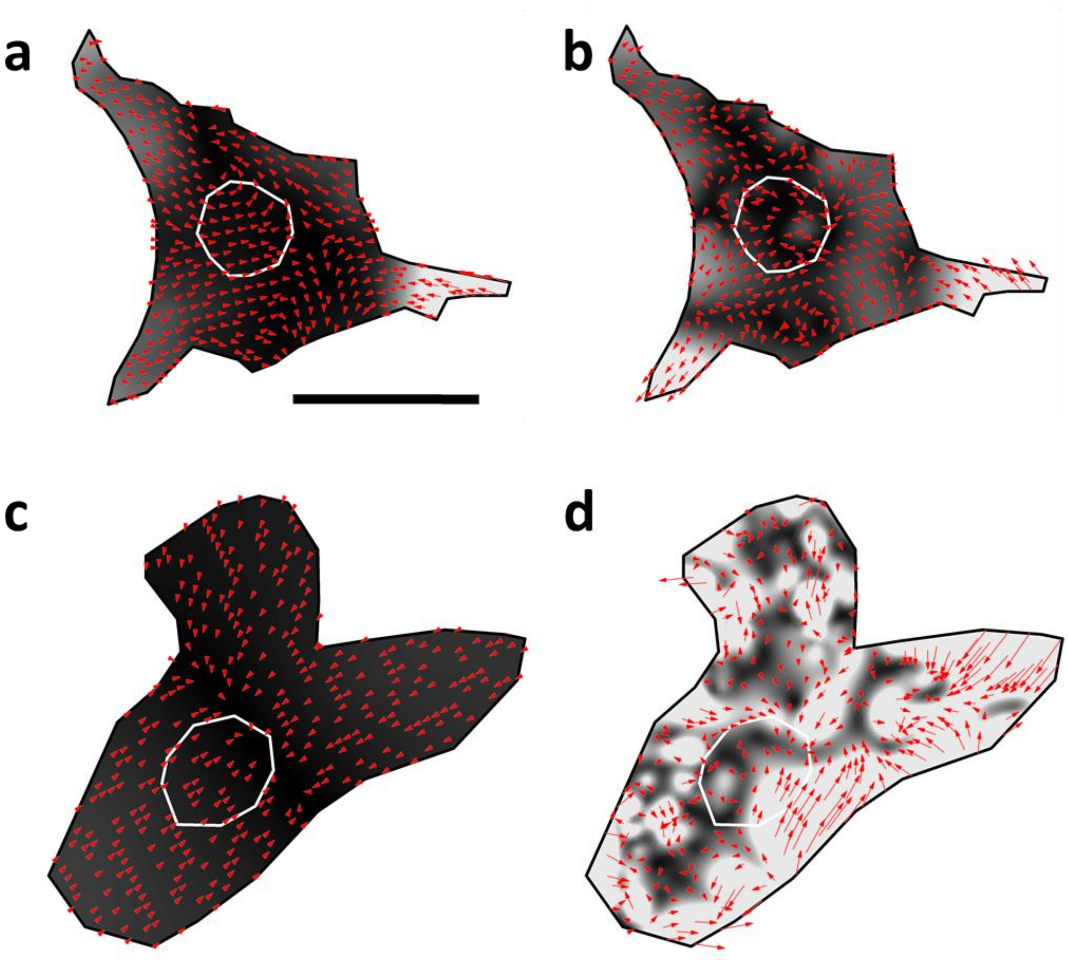

Figure 4.3.2-2. Absolute traction heat maps and vectors. Greyscale heat maps corresponding to the heat maps shown in Fig. 6.3.2-1 are overlaid with traction vector maps for comparison. Control cells on the (a) 15.7 ± 2.66 kPa (scale bar = 40 µm and applies to all) and (c) 89. 4 ± 0.679 kPa substrates possess relatively smooth traction fields that point towards the cell centroid. The application of force to cells on the (b) 15.7 ± 2.66 kPa and (d) 89.4 ± 0.679 kPa substrates only causes a significant increase in the magnitude of local vectors on the stiff substrate.

4.3.3 Differential traction force dynamics in mechanically stimulated cells.

Based on the absolute traction results, we then examined how local traction fluctuations evolve with time relative to an initial state. Therefore, we performed differential TFM (122), which does not involve the removal of the cell from the substrate. Rather, traction dynamics over time are calculated relative to an initial traction field, making the technique sensitive to fluctuations in traction as a function of time (Fig. 4.3.3). Consistent with the absolute data, differential TFM measurements (n = 9 - 20 cells for each substrate elasticity, Table 1) reveals a statistically significant increase in the average traction fluctuation after 30 sec of mechanical stimulation with a 10 nN force on the 63.8 ± 0.534 kPa (P = 0.03184) and 89.4 ± 0.679 kPa (P = 0.0218) substrates (Fig. 4.3.3a). However, by 60 sec, the average change in traction dissipates to basal levels on the 63.8 ± 0.534 kPa and 89.4 ± 0.679 kPa substrates (Fig. 4.3.3b) and for the remainder of the measurement (data not shown). Interestingly, applying a 1 nN force results in a significant increase (P = 0.00218) in traction fluctuation only on the 63.8 ± 0.534 kPa substrate after 30 sec (Fig. 4.3.3c), which also dissipates by 60 sec (Fig. 4.3.3d) and for the remainder of the measurement (data not shown). An applied force of 1 nN did not cause any other significant traction dynamics, compared to controls, at any other time or on any other substrate. Examining 30 sec traction heat maps for cells on 15.7 ± 2.66 kPa (Fig. 4.3.3e & f) and 89.4 ± 0.679 kPa (Fig. 4.3.3g & h) substrates, reveals the presence of traction hotspots. On the stiff substrates, mechanical stimulation results in the evolution of significant localized hotspots that increase the average traction fluctuation for the whole cell. However, these hotspots also tend to disappear by 60 sec and for the remainder of the measurement. The specific heat maps shown in fig. 4.3.3e-h present two specific cells from the differential traction study and are only shown as representatives of all cells examined (Table 1).

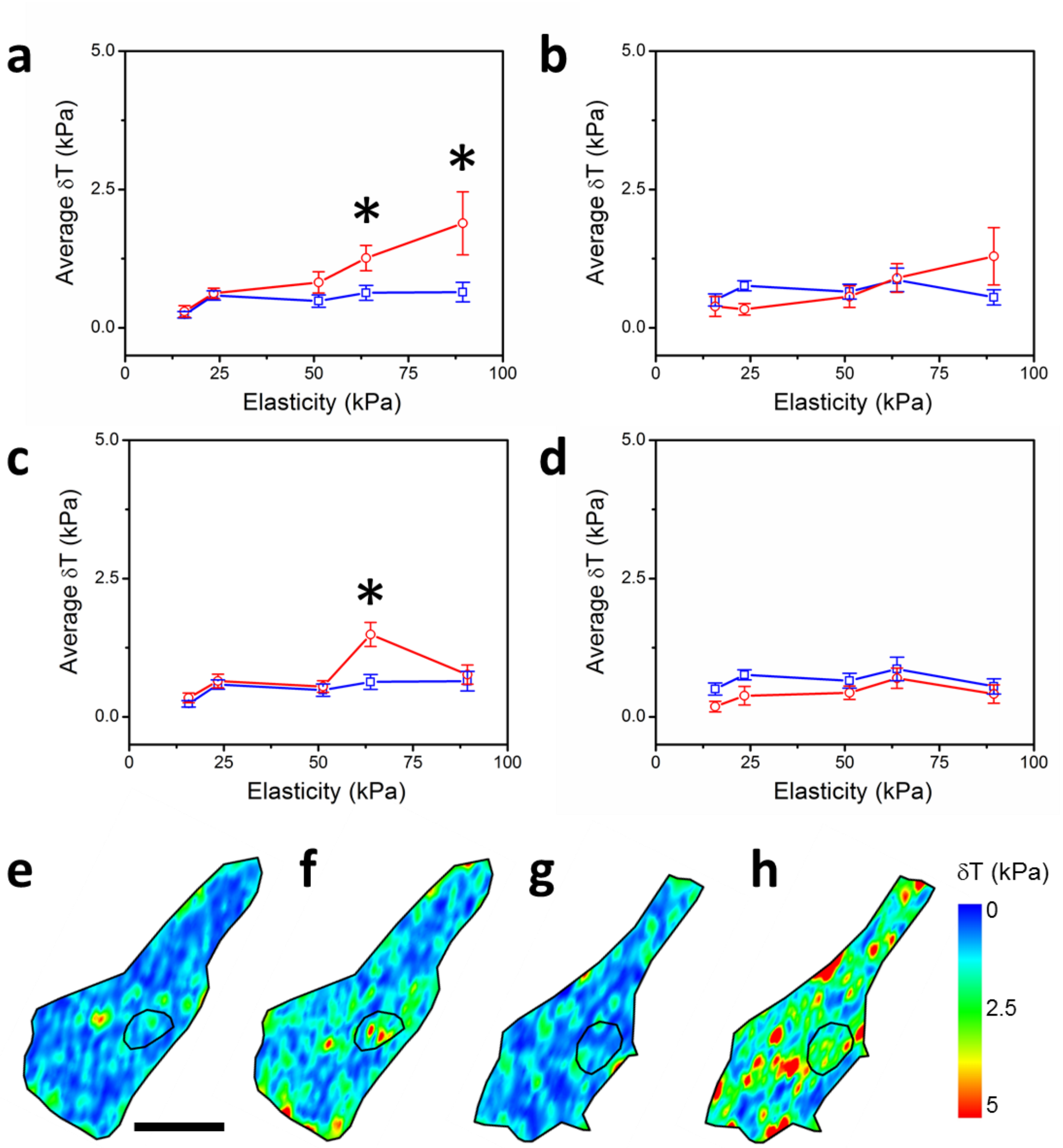

Figure 4.3.3: Differential traction force dynamics on tuneable hydrogels in response to local nanomechanical stimulation. (a) Consistent with the absolute traction data, the average differential traction reveals a statistically significant increase after 30sec of stimulation with 10nN of force on 63.8 ± 0.534 kPa (P = 0.03184) and 89.4 ± 0.679 kPa (P = 0.0218) substrates: blue squares (control) and red circles (10nN). (c) In response to 1nN of force, a significant increase in traction fluctuations was only observed on the ~64kPa substrate (P = 0.00218). By 60 sec, the average change in traction dissipates to basal levels for (b) 10nN and (d) 1 nN applied force, and remains that way for the rest of the 120sec measurement (data not shown). Heat maps for a representative (e) control cell on a 15.7 ± 2.66 kPa substrate (scale bar = 40μm and applies to all) and (f) the same cell when exposed to a constant 10nN force for 30sec. Although a small increase in traction

fluctuations and hotspots can be observed, they are not significant. Heat maps for a representative (g) control cell on a 89.4 ± 0.679 kPa substrate and (h) the same cell when exposed to a constant 10nN force for 30 sec. A significant increase on traction fluctuations are observed as well as local hotspots throughout the contact area. Again, this significant change in traction only occurred on the stiff substrate. All values are average ± s.e.m.

4.3.4 Traction force dynamics after rho-kinase and myosin-II inhibition.

Rho-kinase (ROCK) and myosin-II (MyoII) both play a major role in mechanotransduction by governing the morphology of the actin cytoskeleton, focal adhesion remodelling pathways and the dynamics of acto-myosin contractility (25, 27, 81). To investigate the role of ROCK and MyoII in governing the conversion of a mechanical stimulus into traction dynamics, we examined the effects of the ROCK inhibitor, Y-27632, and the MyoII inhibitor, blebbistatin, on cell morphology and traction dynamics. We first examined the morphology of actin stress fibres and vinculin-rich focal adhesions of untreated cells on three substrates: plastic with a surface coating of 0.1% gelatine, as well as 15.7 ± 2.66 kPa (soft) and 89.4 ± 0.679 kPa (stiff) GXG hydrogels (Fig. 4.3.4-1). In untreated cells, actin stress fibres were observed to be intact and found throughout the cell on all three substrates (Fig. 4.3.4-1a). Numerous mature, punctate focal adhesions were observed on the various substrates. As expected, ROCK (Fig. 4.3.4-1b) and MyoII (Fig. 4.3.4-1c) inhibition drastically altered the morphology and organization of the cell cytoskeleton. Stress fibres were either absent or reduced to thin fibrils on all substrates examined. Focal adhesions displayed an almost complete loss of the typical well-defined, punctate structures and a distinct decrease in average size (Fig. 4.3.4-1d), (72 - 123 FAs analyzed for each condition from a total of n = 3 cells, Table 1).

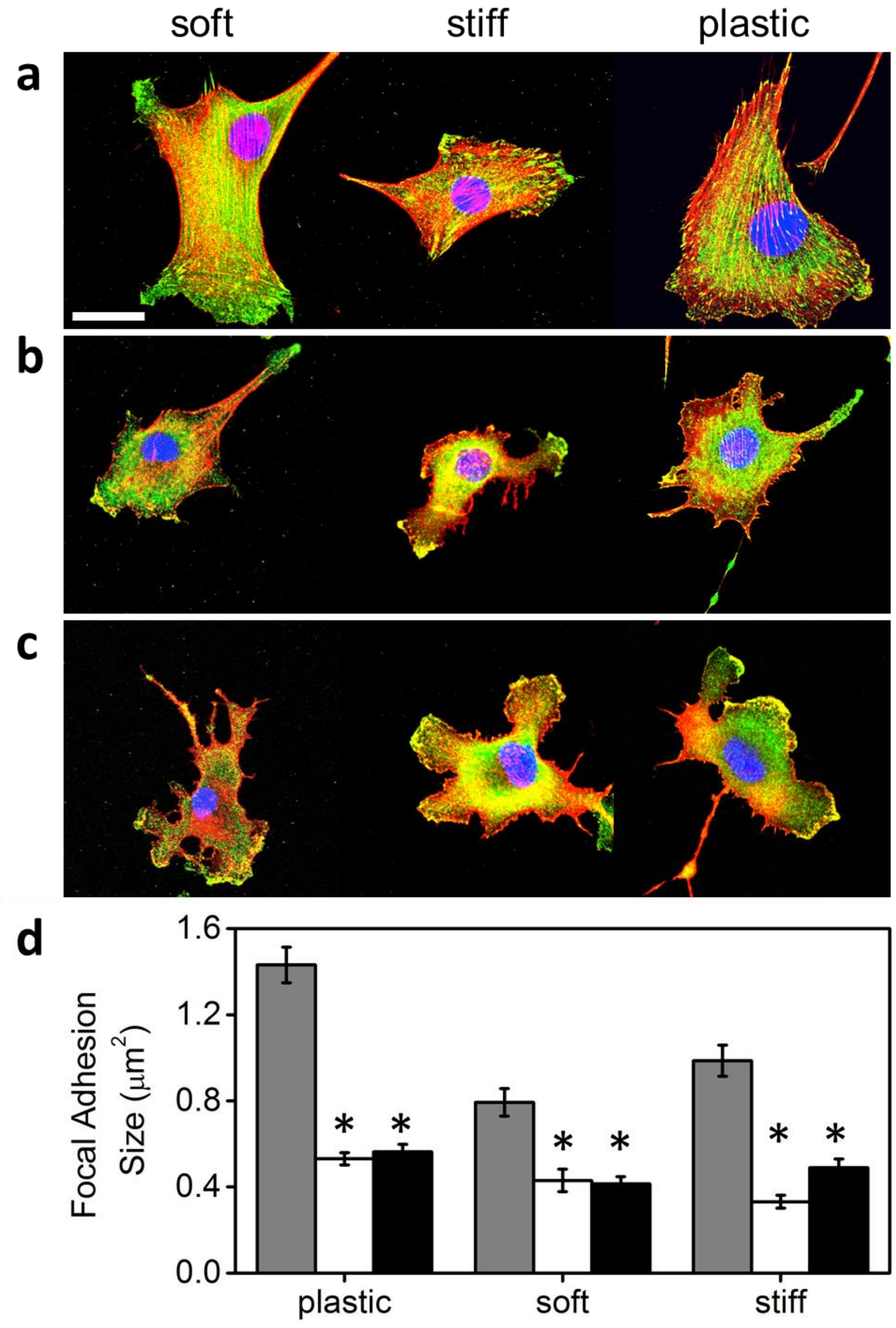

Figure 4.3.4-1: Immunofluorescent images obtained with confocal microscopy of control cells and cells after rho-kinase and myosin-II inhibition. Three substrate conditions were considered: soft (15.7 ± 2.66 kPa), stiff (89.4 ± 0.679 kPa) and plastic coated with 0.1% gelatine and a representative cell is shown for each condition. (a) Untreated cells on all three substrate stained for actin (red), vinculin (green) and DNA (blue).

Actin stress fibres were observed to be intact and found throughout the cell on all three substrates. Numerous mature, punctate focal adhesions were also observed. Cells pre-treated for 30min with Y27632 and blebbistatin are shown in (b) and (c) respectively. Both conditions altered the morphology and organization of the cell cytoskeleton. Stress fibres were either absent or reduced to thin fibrils on all substrates examined. Focal adhesions displayed an almost complete loss of the typical well-defined, punctate structures. (d) FA sizes were quantified and revealed that ROCK (white bars) and myosin-II (black bars) treatment causes FAs to decrease significantly in size relative to control cells (grey bars) on stiff ($P = 1.46927 \times 10^{-13}$ and $P = 3.64546 \times 10^{-9}$, respectively), soft ($P = 1.03214 \times 10^{-4}$ and $P = 2.65115 \times 10^{-7}$ respectively) and plastic ($P = 1.76682 \times 10^{-20}$ and $P = 8.02119 \times 10^{-19}$, respectively) substrates. All values are average ± s.e.m.

Inhibition of ROCK and MyoII is well known to result in a decrease in absolute traction force relative to uninhibited cells (123, 124). Here, both the absolute (n = 8 - 12 cells for each substrate, Table 1) and differential (n = 9 - 20 cells for each substrate elasticity, Table 1) traction force measurements were performed after pre-treatment for 30 min with Y27632 or blebbistatin. After 30 sec of nanomechanical stimulation there was no longer any statistically significant increase in absolute traction from Y27632 treated cells on the 63.8 ± 0.534 kPa (P = 0.29379) and 89.4 ± 0.679 kPa (P = 0.6068) substrates (Fig. 4.3.4-2a). Similarly, cells treated with blebbistatin also displayed no significant increase in absolute traction on the 63.8 ± 0.534 kPa (P = 0.56215) and 89.4 ± 0.679 kPa (P = 0.71013) (Fig 4.3.4-2b). There was also no significant increase in the differential traction in either case after 30 sec of nanomechanical stimulation on the 63.8 ± 0.534 kPa and 89.4 ± 0.679 kPa substrates (P = 0.16987 and 0.52375 for Y27632 treatments (Fig 4.3.4-2c), and P = 0.94772 and 0.6787 for blebbistatin treatments (Fig. 4.3.4-2d)). After 120 sec of nanomechanical stimulation there continued to be no statistically significant increase in absolute or differential traction on the 63.8 ± 0.534 kPa and 89.4 ± 0.679 kPa substrates for either Y27632 or blebbistatin treatment (Fig. 4.3.4-3).

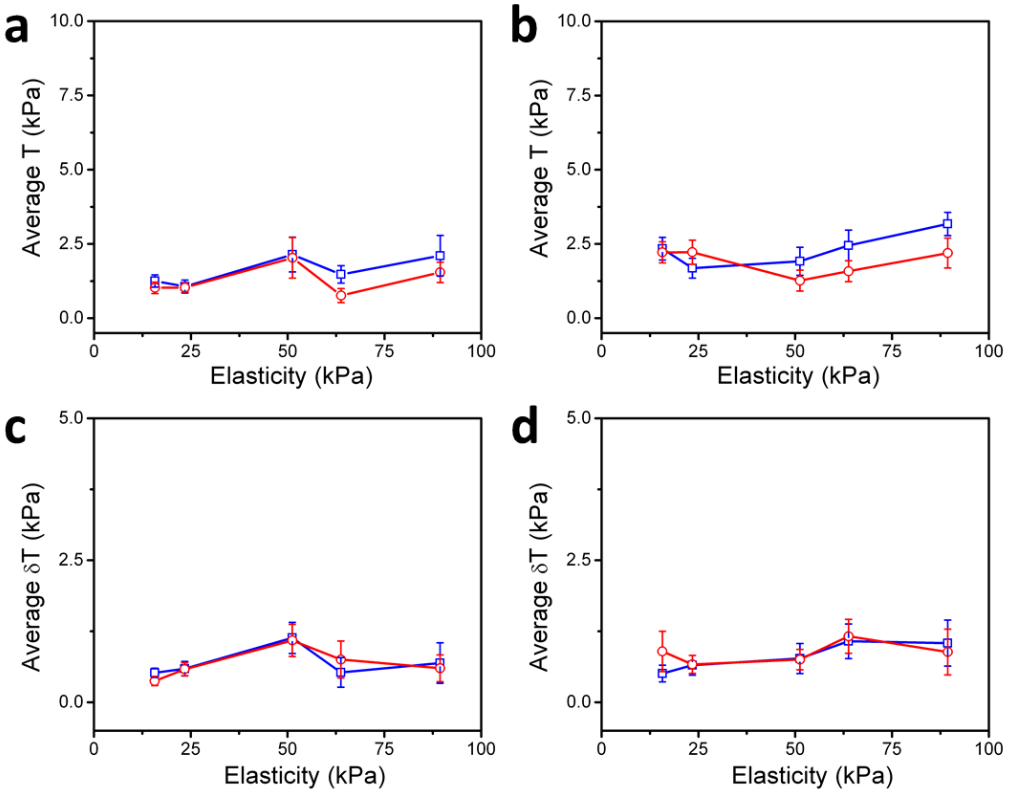

Figure 4.3.4-2. Traction force dynamics after 30 sec of nanomechanical stimulation on cells after Y27632 or blebbistatin treatment. Absolute traction measurements were performed on cells after pre-treatment for 30 min with (a) Y27632 or (b) blebbistatin: blue squares (control) and red circles (10 nN). Differential traction measurements were performed on cells after pre-treatment for 30 min with (c) Y27632 or (d) blebbistatin: blue squares (control) and red circles (10 nN). After 30 sec of nanomechanical stimulation there was no longer any statistically significant increase in absolute or differential traction under any set of conditions.

Finally, we also exposed cells to a 10 nN force for an extended period of time (240 sec) on 63.8 ± 0.534 kPa substrates, where the greatest difference in differential traction was observed. In this case, no significant change in differential traction was observed in response to a nanomechanical stimulus over the entire 240 sec of stimulation for Y27632 (Fig. 4.3.4-3e) or blebbistatin treated cells (Fig. 4.3.4-3f). These results negate the possibility of a delayed response to force when key contractility pathways are inhibited. As expected, inhibiting key mechanotransduction pathways prevents the cells from responding to a nanomechanical stimulus. Finally, as further controls, we also considered cells (n = 3) fixed with 3.5% paraformaldehyde and GXG substrates with no cells to ensure the AFM tip was not inducing spurious changes in bead positions causing apparent traction readouts. In all cases (with and without the application of a 10 nN force), no significant bead displacements were observed resulting in a null traction field. Therefore, baseline traction fluctuations and those that occur in response to nanomechanical stimulation are due to active cellular mechanotransduction pathways.

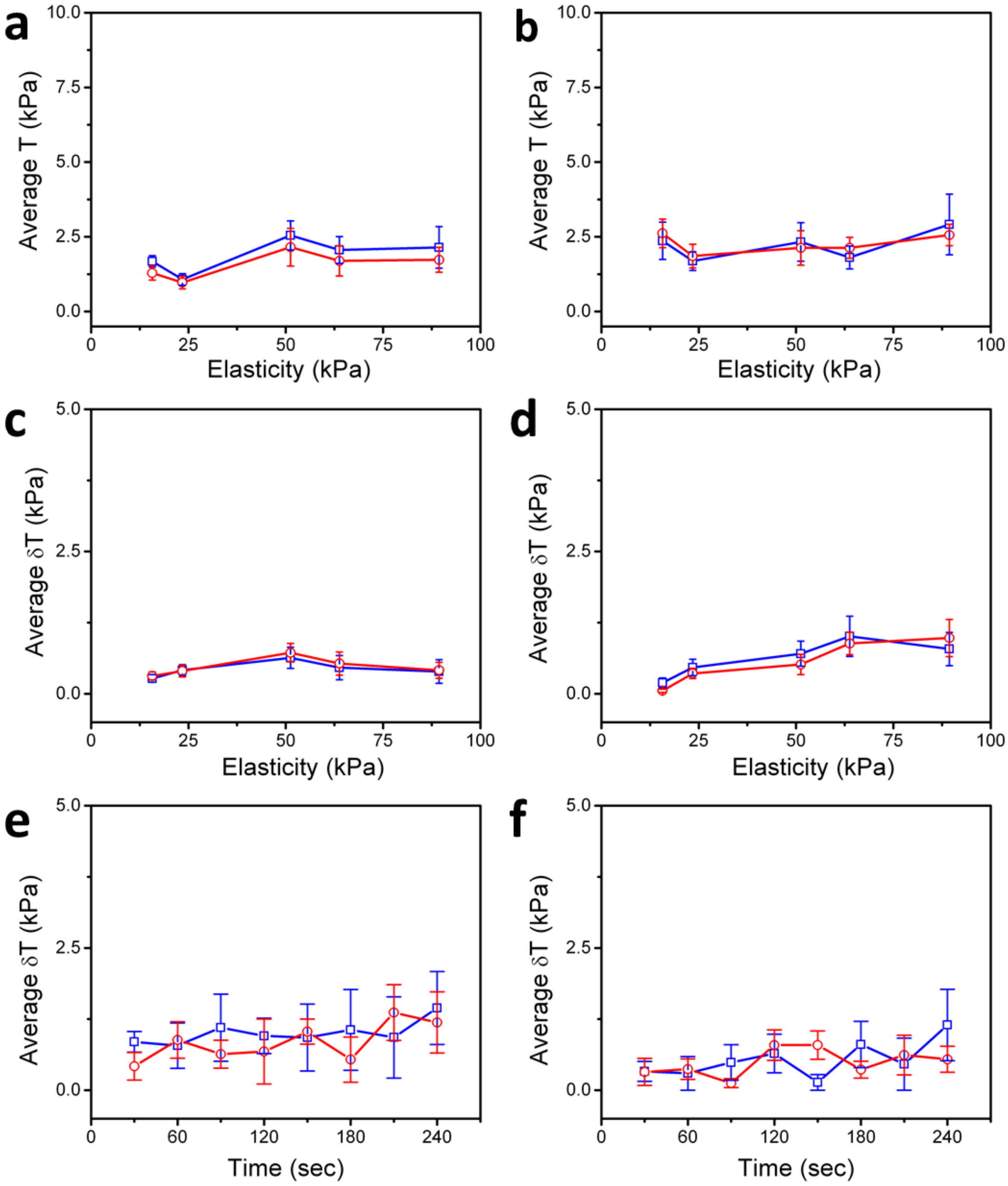

Figure 4.3.4-3: Traction force dynamics after 120 sec of nanomechanical stimulation on cells after Y27632 or blebbistatin treatment. Absolute traction measurements were performed on cells after pre-treatment for 30 min with (a) Y27632 or (b) blebbistatin: blue squares (control) and red circles (10 nN). Differential traction measurements were performed on cells after pre-treatment for 30min with (c) Y27632 or (d) blebbistatin: blue squares (control) and red circles (10 nN). After 120 sec of nanomechanical stimulation there was no longer any statistically significant increase in absolute or differential traction under any set of

conditions. In order to test for a delayed traction response, differential traction experiments were repeated on cells pre-treated with (e) Y27632 and (f) blebbistatin and exposed to a 10nN force on a 63.8 ± 0.534 kPa substrate for up to 240sec. Plots of the traction as a function of time reveal no significant increase in traction over the controls during the entire measurement in either case. All values are average ± s.e.m.

4.4 Discussions

In this study we characterized how myoblast cells respond to local nanomechanical stimulation with AFM on substrates of increasing elasticity using traction force as a readout. We chose to employ gelatine based hydrogels (116, 118, 119), due to their inherent biocompatibility, routine use as a coating in cell culture studies and that it is a close model of the in-vivo microenvironment. Importantly, C2C12 traction forces observed in this study were consistent with studies on PA gels (109). Moreover, the morphology and physical characteristics of the C2C12 cells were similar or identical to our previous studies on the cell line when cultured on other types of substrates including glass, plastic and PDMS with various coatings (108). These observations allow us to be reasonably sure that the results observed in this study are representative of the biology of C2C12 myoblasts. These cells are an ideal model system, as they are clearly mechanosensitive and must incorporate nanomechanical cues arising in the tissue microenvironment to carry out their physiological function (14, 20-24, 125). Nanonewton mechanical stimulation with the AFM typically results in a localized deformation of ~10-20% of the cell height over the nucleus (114). Myoblasts were observed to clearly increase their average traction magnitude in response to a local 10 nN force but only on substrates with an elasticity greater than ~64 kPa. No significant response is observed on softer substrates. Moreover, the response to nanomechanical force is rapid, occurring within 30 sec. Absolute traction measurements reveal that the response is constant during the stimulation. Interestingly, differential measurements reveal that while there is a rapid increase in traction fluctuations within 30 sec, they dissipate just as rapidly. In response to nanomechanical stimulation, local increases in traction were observed throughout the cell contact area. This is consistent with our previous work demonstrating that stimulation with AFM over the nucleus results in highly localized deformation of the cytoarchitecture far from the point of contact in addition to limited and localized focal adhesion remodelling (114). As shown previously, the AFM tip did not penetrate through the entire cell and damage the nucleus and cell membrane, even after mechanically stimulating the cells with large forces for several minutes (114, 126). Finally, ROCK and MyoII inhibition causes focal adhesions to become significantly reduced in size and there is a complete loss of any response to nanomechanical stimulation regardless of substrate elasticity.

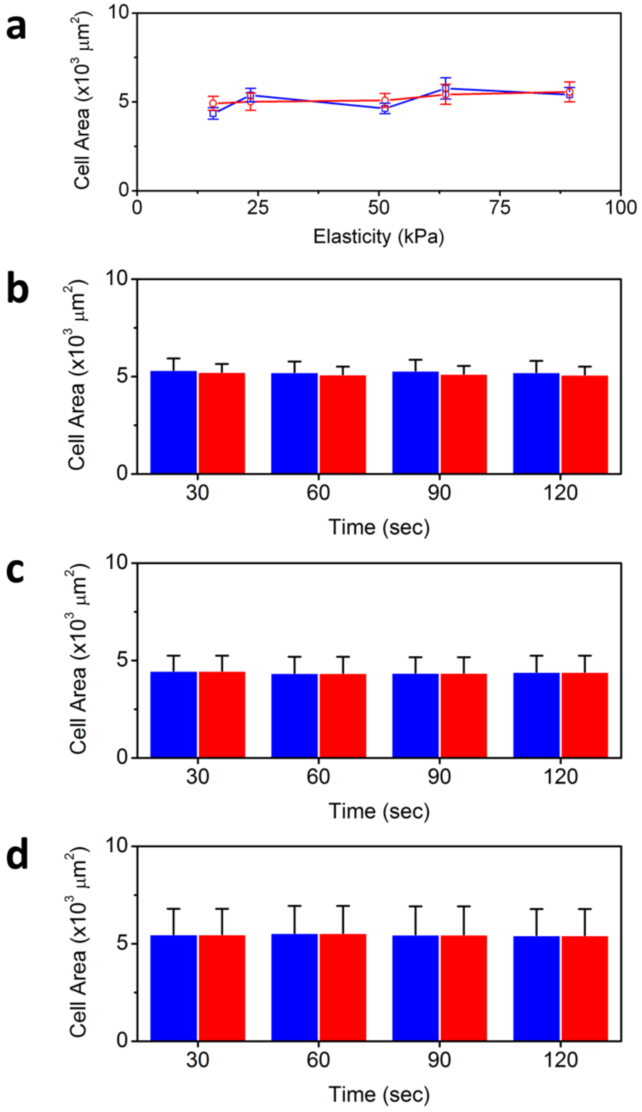

Figure 4.4. The spreading areas of all cells before and after 30sec of force application. (a) There was no dependence of untreated cell size on substrate elasticity before (blue) or after (red) force application. Results are similar for cells treated with Y27632 or blebbistatin (data not shown). (b – d) Cell size also remained constant before (blue bars) and after (red bars) mechanical stimulation over time (30-120sec) for (b) untreated cells, (c) Y27632 treated cells and (d) blebbistatin treated cells. Data shown is for cells cultured on, 63.8 ± 0.534 kPa substrates (similar results were obtained on all elasticities). All values are average ± s.e.m.

In contrast to the results presented here, it has been demonstrated that smooth muscle cells display a sudden decrease in traction accompanied by actin fluidization in response to substrate stress (89, 90). This indicates that cells likely possess cell-type specific responses to particular types of mechanical stress. Conversely, local mechanical stimulation with AFM can result in nanometer-scale displacements and small strain fluctuations occurring heterogeneously along actin stress fibres (114). Importantly, cell shape also tends to stay constant during stimulation with AFM as opposed to substrate stretch. In earlier work (14), it was demonstrated that increasing substrate elasticity increased cell size up to a plateau of ~2100 μm^2 on substrates with an elasticity greater than ~10 kPa. Consistent with this, we observed that untreated and Y27632 or blebbistatin treated cells in this study had a constant size of ~5000 μm^2 on all GXG substrates (~16-89 kPa) with no significant change in cell size in response to force, or as a function of time (Fig 4.4). Basal traction forces are also known to increase with cell area (121), but this phenomenon was not observed in control cells, as expected (Figs. 4.3.2-1 & 4.3.3). This behaviour may be due to the fact on substrates with an elasticity >16 kPa, cells are generating a maximum basal level of traction. Consistent with this observation, it was previously shown that for unstimulated cells, a limit was reached in terms of their basal traction and expected size as the substrate became stiffer (127, 128). Moreover, for both epithelial and fibroblast cells, the generated cell traction forces and projected cell area reached a saturation level, which may be due to the limit by which these cells can reinforce their cytoskeleton and/or focal adhesions (127, 128). It has been demonstrated previously (64) that fibroblast elasticity is relatively constant on substrates >10 kPa. Consistent with this observation, we also found that cells in this study maintained a relatively constant cortical elasticity of ~7 kPa on substrates between ~16 kPa and ~89 kPa. Interestingly, not all mechanosensitive cell types appear to maintain a relatively constant elasticity in relation to the changing mechanical properties of its microenvironment. For example primary cardiac myocytes and fibroblasts isolated from the ventricules of rats showed different responses, where elasticity of cardiac myocytes remained relatively constant whereas the elasticity of cardiac fibroblasts changed with substrate elasticity (~8-50 kPa) (129). In addition, cells grown on softer substrates (~0.095-10 kPa) will attempt to match their elasticity to that of the substrate as shown previously (64, 130, 131); however only at very high substrate elasticity (>10 kPa) do cells fail to match the substrate elasticity (64).These results suggest that on ~16-89 kPa substrates, C2C12 myoblasts may be in a quasi-steady mechanical state (constant cell elasticity, traction force and size) in which they only respond to mechanical force in a microenvironment that mimics working muscle tissue.

Inhibition of ROCK and MyoII is well known to result in a decrease in absolute traction force relative to uninhibited cells (123, 124). When considering the traction forces generated by cells treated with Y27632 or blebbistatin, there appears to be no significant decrease relative to untreated cells (comparing the blue lines in Figs. 4.3.2-1a and 4.3.3a to the blue lines in Fig. 6.3.4-2). However, there is a clear decrease in focal adhesion size under these conditions. This suggests that treatment with 10 μM of blebbistatin and 20 μM of Y27632 did not cause a strong inhibition of basal traction forces. This is very surprising given the literature that exists in which these inhibitors have been examined. In a recent study (132), U2OS cells were incubated with 50 μM of blebbistatin, where the traction forces decreased dramatically compared to the controls. Previous studies (133, 134) have shown that even though MDCK and NRK cells, respectively, were treated with 30 μM and 100 μM of blebbistatin, the cells still maintained the ability to migrate for several hours. All of the above studies were performed on much softer (<10 kPa) or very hard (glass) substrates compared to our study. In contrast, our previous work on C2C12 cells (108) demonstrated that they are able to maintain a high degree of contact and adhesion strength with their microenvironment even after treatment with Y27632 and blebbistatin. Therefore, basal traction forces are dependent on substrate elasticity and the concentration of Y27632 or blebbistattin. However, basal traction forces also exhibit a clear dependence on cell type.

Our results imply that the integration of extracellular nanomechanical forces and the nanomechanical properties of the cellular microenvironment modulates mechanotransduction pathways in myoblasts. The exact mechanism of the observed integration of mechanical cues is of course highly complex and not entirely understood at present. However, we can speculate on the possible mechanisms that give rise to this behaviour. Importantly, we hypothesize that there are two important steps in the possible mechanisms that govern the traction responses we observe in this paper. The first is a physical mechanism through which mechanical force is transmitted to focal adhesion sites and the second step is a biochemical mechanism through which mechanical force is converted into focal adhesion remodelling and traction dynamics. In previous work we have demonstrated that locally delivered nanonewton forces are physically transmitted throughout the actin and microtubule cytoskeleton leading to the onset of focal adhesion remodelling (114). This is likely taking place in cells on substrates >64kPa, however on soft substrates this process becomes impaired. We observe that on soft substrates the average focal adhesion size decreases by ~20% (1.0 to 0.8 μm^2) although the actin network does appear to remain intact. This is consistent with evidence that focal adhesion size and dynamics play an important role in governing the magnitude of cellular traction forces (135, 136). Several focal adhesion proteins (vinculin, zyxin, talin (137, 138)) are also well known to be mechanosensitive and possibly activated by tension in the actin cytoskeleton. We speculate that focal adhesion sites that are below a critical size no longer provide enough resistance against an increase in contractility (139), thus disabling the activation of these mechanosensitive proteins and their role in governing focal adhesion and traction dynamics. Taken together, this physical and biochemical picture would account for the observations in this study. However, future studies are clearly required in order to provide a full and complete mechanism.

Although a local nanomechanical stress similar to indentation with AFM is not likely to occur in-vivo, it may be tempting to examine if these findings have any significance for the process of myogenesis. The elasticity of the GXG hydrogels in this study were chosen to mimic the elasticity of resting (~12-39 kPa) and working (~38-97 kPa) muscle tissue in mice (14-19). The response of mouse C2C12 cells to mechanical force forms part of the initial stages of the myogenic pathway (140, 141). It has been shown that mechanical stimulation during stretch or exercise is responsible for many in-vivo muscle changes after early myogenic progression (35, 140-143). Moreover, myogenesis proceeds optimally on substrates with an elasticity of ~12 kPa (14). These results were linked to the ability of myoblasts to develop traction in a microenvironment with elasticity similar to resting tissue.

Interestingly, our results indicate that myoblasts respond optimally to local nanoscale stimulation in a microenvironment in which the elasticity is similar to active, working muscle tissue. Conversely, the progression of myogenesis (occurring several days after exercise (111, 112)) occurs optimally in a softer microenvironment, similar to resting muscle. Although this is an interesting finding, the results presented here are still limited to the conditions of this experiment and the data should not be over interpreted. Future work will be required to establish a firm link between the observations based on AFM/TFM measurements and the dynamics that occur in-vivo, especially during later stage fusion. Specifically, we envision experiments designed to examine the effects of planar stretching on traction force dynamics, especially during the early fusion of single myoblasts. Another more controlled approach maybe to perform stretching experiments on myoblasts patterned on islands of specific size and examine how traction dynamics evolve during fusion (144). Regardless, the major finding of this study is the observation that myoblasts possess an in-vitro mechanism that allows them to actively integrate at least two pieces of nanomechanical information during the regulation of traction force dynamics. These findings demonstrate that traction forces can be highly regulated and influenced by very different nanomechanical cues found in the microenvironment.

4.5 Conclusions

It is becoming increasingly evident that there is a very close relationship between fundamental biological pathways and physical cues found in the nanomechanical microenvironment of living cells (25, 27, 81-85). Cells are exposed to multiple physical cues at the macro- and nano-scales that integrate and eventually modulate cell-type specific mechanotransduction and mechanosensitivity pathways. Employing traction force as an indicator of mechanotransduction in myoblasts, we have examined the interplay between substrate elasticity and nanomechanical stimulation. As demonstrated here, myoblasts are actually insensitive to nanomechanical stimulation on substrates less than ~64 kPa. However, in a stiffer microenvironment, myoblasts respond rapidly and transiently to a nanomechanical force. Moreover, traction dynamics evolve rapidly in response to mechanical stimulation and can be transient in nature. Here, we have demonstrated that traction dynamics are highly regulated by a fundamental ability of myoblasts to simultaneously integrate the cross talk between extracellular nanoscale forces and substrate nanomechanics.

4.6 Acknowledgement

This work was supported by a Natural Sciences and Engineering Research Council Discovery Grant [grant number RGPIN/355535-2009 to A.E.P.] and Discovery Accelerator Supplement [grant number RGPAS/380321-2009 to A.E.P.]; the Canada Research Chairs program [grant number 950- 206182 to A.E.P.]; and a Province of Ontario Early Researcher Award [grant number ER09-06-158 to A.E.P.]. Z.A.R. gratefully acknowledges the uOttawa NSERC CREATE program in Quantitative Biomedicine for graduate student support.

	GXG Elasticity (kPa)				
	15.7±2.7	23.5±2.8	51.2 ± 4.2	63.8±5.5	89.4±6.8
Absolute TFM					
0nN	9	11	9	9	9
10nN	10	12	9	15	12
Differential TFM					
0nN	19	20	19	11	12
1nN	14	10	13	12	11
10nN	14	14	13	11	9
Absolute Y27632 Treatment					
0nN	8	11	10	10	9
10nN	8	10	10	9	10
Differential Y27632 Treatment					
0nN	15	16	18	13	9
10nN	11	17	20	15	13
Absolute Blebbistatin Treatment					
0nN	10	12	12	8	8
10nN	11	12	12	12	9
Differential Blebbistatin Treatment					
0nN	14	15	16	15	9
10nN	14	15	15	14	13

Table 1: Number of cells examined in each experiment in chapter 6.

Chapter Five: Microtubules mediate changes in the cortical elasticity of fibroblasts during contractile activation.

The material in chapter four is subject of a paper submitted for publication to Experimental Cell Research (Manuscript: ECR-13-506: "Microtubules mediate changes in membrane nanomechanics during contractile activation" by Z. Al-Rekabi, K. Haase and A.E. Pelling; 1st Revision).

Abstract

The mechanical properties of living cells are highly regulated by remodelling in the cytoarchitecture (cytoskeleton, nucleus, and organelles) and are linked to a wide variety of physiological and pathological processes. Microtubules (MT) and actomyosin contractility are both involved in regulating focal adhesion (FA) size and cortical elasticity in living cells. Although several studies have examined the effects of MT depolymerisation or actomyosin activation on biological processes, very few have investigated the influence of both on the mechanical properties, FA assembly and spreading of fibroblast cells. Here, we examined how activation of both processes modulates cortical elasticity as a function of time. The individual enhancement of contractility (calyculin A treatment) or the depolymerisation of MTs (nocodazole treatment) both caused an increase in FA size and a subsequent increase in cortical elasticity. Surprisingly, stimulating both processes simultaneously led to a decrease in cortical elasticity, loss of intact FAs and a concomitant increase in cell height. The results demonstrate that the loss of MTs disables the ability of fibroblast cells to maintain increased contractility and cortical elasticity upon activation of myosin-II. The interplay between cytoskeletal remodelling and actomyosin contractility modulate FA size and cell height leading to dynamic, time-dependent changes in the cortical elasticity of fibroblast cells.

5.1 Introduction

The cytoskeleton is a complex structure composed primarily of actin, microtubules (MTs) and intermediate filaments, and is required for an enormous array of cellular processes (121, 145-149). Actin is involved in the maintenance of cell morphology and adhesion as a result of their contractile nature and interaction with focal adhesion (FA) complexes. MTs and intermediate filaments also play crucial roles in many dynamic changes in cell shape, migration and adhesion. Importantly, changes in the composition and structure of the cytoskeleton during physiological and pathological processes have been shown to correlate with distinct changes in the physical properties of the cell (145, 148, 150). Moreover, crosstalk between the mechanical properties of the cell and the microenvironment regulates many of these processes (145, 148, 150).

For example, cytoskeletal remodelling plays an important role during cell death (apoptosis) and AFM has been employed to demonstrate the controlled mechanical breakdown of the cell (113). During apoptosis, the loss of mechanical regulation can lead to poor control of the cortical elasticity and apparent viscosity of the cell. Moreover, cell death induced with several chemotherapy agents has also been shown to result in a significant increase in elasticity within several hours (151). In addition, the AFM has been employed to elucidate on the mechanics of cytokinesis (152, 153), revealing that for proper spindle assembly and chromosome segregation, the activity and localization of moesin contributed to a stiff rounded cortex at metaphase. The AFM has also revealed important insights leading to further understanding of pathological processes (154-156). The biomechanics of cancer cells, in particular, has been identified as a possible platform for cytological evaluation of tumours (105, 157), where changes in elasticities of cancer cells can be used as an indicator for distinguishing cancerous cells from normal healthy cells in patients (105, 157). In addition, AFM may be used to monitor subtle structural and mechanical changes of articular cartilage that occurs during aging and at the onset of osteoarthritis (158). The atomic force microscope (AFM) has emerged as one of several tools that can be employed to investigate and quantify the mechanical properties of cells and their responses to mechanical stimuli (150, 159). The elastic properties of the cells can be imaged and quantified during numerous critical physiological and pathological cellular processes (145, 150). In addition, the AFM has also become an attractive tool for understanding how cells respond to local nanoscale forces (150).

The disruption of the cytoskeleton by selective removal of specific molecules through genetic or biochemical approaches is often employed to systematically study changes in the local mechanical properties of the cell. It has also been shown that the depolymerization of actin or inhibition of myosin-II results in a decrease in cortical elasticity and traction forces (129, 160-163). Conversely, increasing myosin-II contractility induces the assembly of FAs (163-167) and leads to increased traction forces and cortical elasticity (153, 168). The disruption of the MT network has resulted in conflicting results. The loss of MTs can have no impact on cell mechanics (161), result in cell stiffening (129, 162, 169) or cell softening (113, 170). However, the disruption of MTs alters actomyosin contractility, traction forces and cortical elasticity (121, 171-173). Therefore, there are two possible pathways in which cortical cell elasticity can be increased – MT depolymerisation or actomyosin activation. The simultaneous enhancement of contractility and depolymerisation of MTs might be expected to signal an increase in FA size and a subsequent increase in elasticity. However, there has been no systematic study of the effect of activating both pathways, individually and simultaneously, on the cortical elasticity, FA assembly and spreading of NIH3T3 fibroblasts.

Here, we show that stimulation of these two pathways individually lead to an increase in cortical elasticity. However, this response is not additive as activating these pathways in parallel led to a decrease in cortical elasticity. This was due to a loss of intact FAs and a concomitant increase in cell height. Clearly, the loss of MTs disables the ability of fibroblast cells to maintain increased contractility and cortical elasticity upon activation of myosin-II. These results illuminate the complex interplay between cytoskeletal and FA remodelling dynamics that ultimately control the mechanical properties of the cells. It should be noted however that these changes in cortical elasticity were also highly time dependent. Understanding how the mechanical properties of cells are regulated is of extreme interest due to the role that these properties play in critical physiological and pathological pathways (145, 148, 150, 174). This knowledge may aid in our understanding of the mechanisms that link mechanotransduction and mechanosensitivity signalling pathways to remodelling dynamics in the cytoarchitecture during normal physiological and pathological processes (27, 175, 176).

5.2 Materials and Methods

5.2.1 Cell Culture and Reagents

NIH3T3 mouse fibroblast cells were maintained in a 37°C, 5% CO_2 incubator and cultured in DMEM with 10% fetal bovine serum and 1% streptomycin/penicillin (all from Hyclone Laboratories Inc.). Experiments were performed 24 hrs after cells were cultured on 0.1% gelatine (GE) coated plastic at a density of ~10^5 cells/cm^2 respectively. All drugs (Sigma) were stored as stock solutions in DMSO at -20ºC. Calyculin A was used at a final concentration of 1 nM and nocodozole was used at a final concentration of 10 µM. The concentrations were chosen based on commonly employed values used in previous studies (163, 177, 178). These exact concentrations and time durations were used in order to draw insightful comparisons with the previous studies (163, 177, 178).

5.2.2 Immunofluorescent Staining and Transfections

Immunofluorescence staining was carried out as previously described (113) but with some small modifications. Briefly, cells were fixed with 3.5% paraformaldehyde and permeabilized with 0.5% Triton X-100. Cells were then quenched in 0.15 M Glycine for 25 minutes. Actin filaments were stained with Phalloidin Alexa Fluor 546 (Invitrogen), and the nuclei stained with DAPI (Invitrogen). Vinculin was labelled with a monoclonal anti-vinculin primary antibody produced in mouse (Invitrogen) and a rabbit anti-mouse IgG secondary (Invitrogen) antibody conjugated to AlexaFluor 488 fluorophore (each used at a 1:500 dilution). Following each step cells were incubated with wash buffer for 15 minutes (5% Horse Serum (Sigma)). For the MT stains, cells were fixed and permeabilized with -20˚C methanol and immediately placed on ice for 3 minutes. The methanol was quickly removed and cells were washed and incubated with the wash buffer for 15 minutes. MT filaments were labelled with a monoclonal alpha-tubulin primary antibody produced in mouse (Invitrogen) and a rabbit anti-mouse IgG secondary (Invitrogen) antibody conjugated to AlexaFluor 488 fluorophore (each used at a 1:200 dilution).

It is preferable to transfect 12 hours after cells have been passaged. The liposomal technique involved Plasmids for the PH domain of PLCδ conjugated to EGFP (PH-PLCδ-EGFP) has been described previously (179). DNA containing GFP protein as (PH-PLCδ-EGFP) was amplified using E. *coli* cells. Bacteria are well-suited for this purpose since cells multiply rapidly, where they easily replicate plasmid DNA as well as their own. After the amplification process, the DNA was isolated, quantified and used for transfection. The technique also involved incubating the plasmid DNA with a solution of cationic lipids which accumulate around the negatively charged DNA forming complexes of lipid/DNA (180). These liposomes were then replaced in the dish with 3T3 fibroblast cells. Through endocytosis, the process through which cells absorb molecules (such as liposomes) by engulfing them enables the DNA to successfully be transported to the cytoplasm to the inside of the cell. For each dish of cells a solution containing 46 µl of Optimem (Invitrogen) and 4 µl of Lipofectamine 200 reagent (Invitrogen) were prepared. In addition, in a separate tube a solution of 50 µl containing 1 µg of PLCδ conjugated to EGFP (PH-PLCδ-EGFP) plasmid DNA in Optimem was prepared. After 5mins to allow for equilibration, the two solutions were combined, where the resulting solution was 100 µl, this was allowed to sit at room temperature for 25 mins, before it was added directly to the suspension of cells containing DMEM. After two days, experiments were conducted on the dishes.

In all cases, samples were then mounted in vectashield (Vector Labs) and a glass coverslip placed on top. All imaging were then carried out on an A1R high speed laser scanning confocal microscope (LSCM) using a 60X water immersion objective (Nikon, Canada). All images were processed and analyzed with ImageJ.

5.2.3 Atomic Force Microscopy

An AFM (Nanowizard II, JPK Instruments) was used for all experiments with PNP-TR-50 cantilevers (Nanoworld) with spring constants of 69±6pN/nm (Average±SD). 2 cells were randomly chosen from n = 10 plates and 5-15 force curves were collected on each cell over the nucleus, until 100 force curves in total were acquired. Moreover, the AFM measurements were obtained in ± 2 mins. Multiple PNP-TR-50 tips were calibrated and the value presented here is the average value ± s.e.m. Force-displacement curves were recorded at 1 Hz with a velocity of 1 µm/sec. The half angle of the AFM tip was 35º. The Sneddon model is only valid for small indentations of about 10-20% of the height of the cell, maybe 200-1000 nm (56, 170, 181), where the substrate is not influencing the calculations and where the geometry of the indentation matches the geometry of the indenter. In addition, since we are assuming that the cells behave as an elastic material, which is generally true at such small indentations, then it is safe to use a Poisson ratio of 0.5. Data analysis was carried out using PUNIAS software (182).

5.2.4 Quantification of Focal Adhesion Area, Cell Spreading Area and Cell Height

Image post-processing was carried out in ImageJ, where FA images were thresholded and segmented using available ImageJ plugins (Fig. 5.3.2a). For cells transiently expressing PH-PLCδ-EGFP were used to quantify cell height. Cell heights were determined from orthogonal maximum intensity projections of cell expressing PH-PLCδ-EGFP. A line was drawn across the nucleus; this generated intensity versus displacement map (Fig. 5.3.3b). The height was measured as the haf-width of the curve.

5.2.5 Statistical Analysis

All values are presented as the average ± s.e.m. A two-sample t-test ($P < 0.05$) was performed to indicate significance.

5.3 Results

5.3.1Measurements of the mechanical properties of NIH3T3 fibroblasts in response to calyculin A and nocodazole treatments

In this study we examined the activation of two contractility pathways through the activation of myosin-II (calyculin A treatment) or depolymerization of MTs (nocodazole treatment). NIH3T3 mouse fibroblast cells were cultured on plastic coated with 0.1% GE, and then treated with each agent either individually or in combination. LSCM images of actin filaments and vinculin were acquired in order to visualize changes in the cytoskeletal and FA structure relative to the untreated cells (Fig. 5.3.1-1). The untreated fibroblasts appeared well spread with prominent FAs and actin filaments (Fig. 5.3.1-1a). Calyculin A-treated cells were well spread displaying actin filaments and more elongated FAs (Fig. 5.3.1-1b). In addition, fibroblasts were also treated with nocodazole; however both the actin filaments and FAs remained intact and prominent as expected (Fig. 5.3.1-1c). The sequential combination of calyculin A and nocodazole resulted in a reduction of discrete FAs compared to the untreated cells (Fig. 5.3.1-1d).

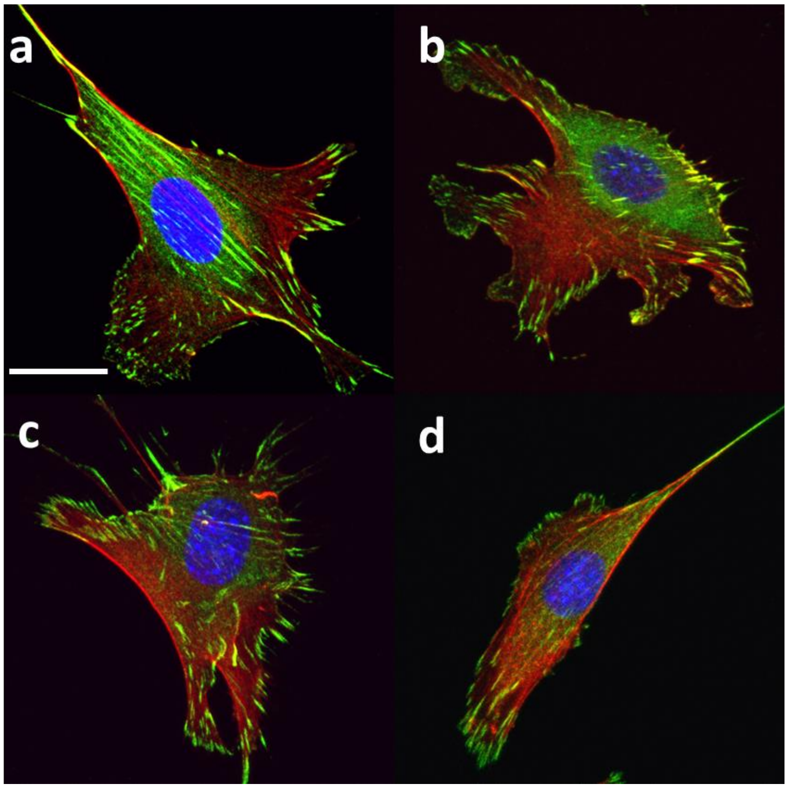

Figure 5.3.1-1: Immunofluorescent images of NIH3T3 fibroblast cells following treatments with calyculin A and nocodazole alone or in combination. LSCM images were taken to visualize the changes in the size of vinculin-rich FAs and actin filaments in fibroblast cells. Cells were fixed and stained for vinculin (green), actin filaments (red) and DNA (blue). Discrete FAs are clearly visible in large numbers and sizes for the untreated cells (a). More FAs were seen for the calyculin A- and nocodazole-treated cells (b and c respectively) and less were seen in the case of the combined treatment with the two drugs (d). Scale bar: 26μm.

In order to assess the effect of these drugs individually and in combination on the mechanical properties of fibroblasts, the local cortical elasticity of the cells were obtained (183). Untreated fibroblasts cells (n = 20) were observed to possess a local cortical elasticity of 5.05 ± 0.098 kPa (Fig. 5.3.1-2a). Fibroblasts were then individually treated with calyculin A or nocodazole for 30 minutes and 5 minutes respectively and then assessed with AFM (n = 11-20 cells). When cells were treated with calyculin A alone there was a significant increase in elasticity as expected ($P = 8.213 \times 10^{-16}$). In addition, treatments with nocodazole, which disrupts MTs also revealed a significant increase in cell elasticity ($P = 1.964 \times 10^{-13}$). The effect of calyculin A and nocodazole in combination was then investigated, where cells were initially incubated with calyculin A for 30 minutes followed with 5 minutes treatment with nocodazole. Interestingly, a significant decrease in cortical elasticity was observed (P =

2.184×10^{-7}) compared to the untreated cells. We also performed a control in which cells were treated only with the vehicle DMSO (n = 10 cells) and we found no significant difference compared to untreated cells for all conditions (4.703 ± 0.1727) kPa and (4.367 ± 0.1059) kPa, P = 0.0838). MTs were also stained and imaged with LSCM and revealed the effects of calyculin A and nocodazole on the MT cystoskeleton. After 30 minutes of calyculin A treatment, MTs are observed to remain intact and fibrous, similar to untreated cells (Fig 5.3.1-2b). However, after 5 minutes of nocodazole treatment, much of the MT network was depolymerized with some intact filaments remaining. After sequential incubation with calyculin A and nocodazole, a similar result is observed in which the majority of MTs were depolymerized leaving a small population of intact filaments.

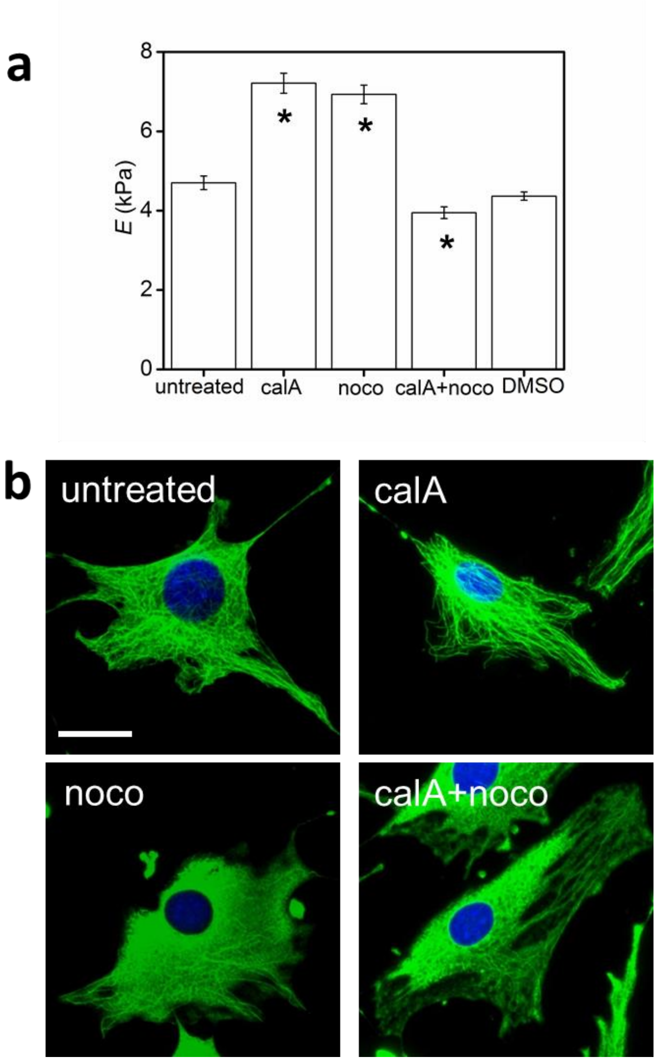

Figure 5.3.1-2: Changes in both cell elasticity and MT distribution of NIH3T3 fibroblasts following treatments with calyculin A and nocodazole alone or in combination. When cells were incubated with

calyculin A there was a significant increase (P = $8.213\text{x}10^{-16}$) observed on the 0.1% GE coated plastic compared to the untreated cells. In addition, treatments with nocodazole, revealed a significant increase in cell elasticity (P = $1.964\text{x}10^{-13}$), implying an overall stiffening of the cell as a result of the actin filaments. Conversely, the effect of calyculin A and nocodazole in combination resulted in a significant decrease in elasticity compared to the untreated case (P = $2.184\text{x}10^{-7}$). As a further control, DMSO-treated cells did not vary significantly from untreated cells for all conditions ((4.703 ± 0.1727) kPa and (4.367 ± 0.1059) kPa, P = 0.0838). The immunofluorescent images obtained by the LSCM demonstrate the effects of calyculin A and nocodazole on the MT cytoskeleton. After 30 minutes of calyculin A treatment, MTs are observed to remain intact and fibrous, similar to untreated cells. After 5 minutes of nocodazole treatment, much of the MT network was depolymerized but some intact filaments remain. After sequential incubation with calyculin A and nocodazole, a similar result is observed in which the majority of MTs have depolymerized. Scale bar: 26μm.

5.3.2 Effect of drug treatments on focal adhesion assembly and cell spreading

To quantify the FA and cell areas for both individually and combined treatments of calyculin A and nocodazole, immunofluorescent confocal images were obtained and post-processed by segmentation (Fig. 5.3.2a) (n = 6 - 12 cells, with 150 FAs analyzed in total). Fibroblasts plated on 0.1% GE coated plastic attach and spread well such that the FA size and distribution appear prominent as shown in Fig. 5.3.1-1a. Interestingly, upon the individual treatments of fibroblasts with calyculin A and nocodazole; there was a significant increase in FA area (P = $5.601\text{x}10^{-4}$; P = 0.0012 respectively; Fig. 5.3.2b). After sequential treatment with both drugs, the FA area decreased significantly (P = 0.0102). Although the average cell spreading area for all treatments displayed a similar trend as the cortical elasticity and FA size, there was no significance found compared to untreated cells. This is due to much more variability in observed cell spreading area (Fig. 5.3.2c; $P > 0.1$ in all cases). As expected, the individual or combined drug treatments with calyculin A and nocodazole (Fig. 5.3.1-1b) had dramatic effects on the size and distribution of FAs. FA morphology varied from the typical well-defined elongated FAs to more punctate structures. Taken together, the data suggests that the size of FAs correlates with the cortical elasticity of the cells.

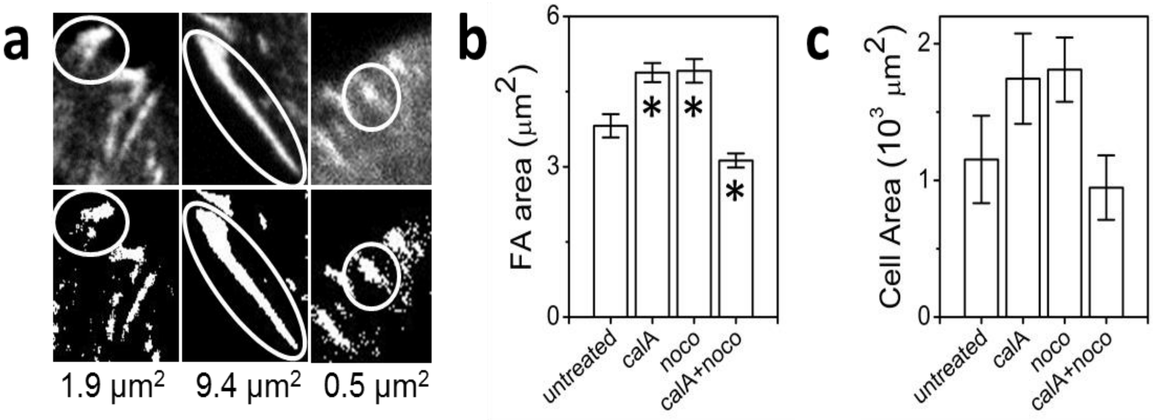

Figure 5.3.2: FA and projected cell area under drug treatments. (a) LSCM images were post-processed in ImageJ, where FA and cell areas were segmented using available ImageJ plugin. Three examples of how the segmenting process was carried showing the area for three different FAs. (b) Upon the individual treatments of fibroblasts with the myosin light chain phosphatase inhibitor, calyculin A and with the depolymerizer of MTs, nocodazole; there was a significant increase in FA area ($P = 5.601x10^{-4}$; P = 0.0012 respectively); moreover in the presence of both drug treatments, the FA area decreased significantly (P = 0.0102). (c) The overall average projected cell area remained unchanged even though the same trend was observed in (b) and in fig. 5.3.1-2a

5.3.3 Effect of drug treatments on cell height

Cell height is also known to have a major influence in the observed elasticity of cells when examined with AFM (184). To investigate the effect of the drugs on cell height, experiments were performed on cells transiently expressing the pleckstrin homology (PH) domain transfected with the PLCδ conjugated to EGFP (PH-PLCδ-EGFP). This protein appears to be localized to the cell membrane (179) and therefore provides a means of directly visualizing and measuring cell height (Fig. 5.3.3a & b). Cells were stained with Hoesht 33342 for the nucleus and fixed with 3.5% paraformaldehyde. LSCM images were obtained for all conditions (n = 9 - 14 cells) and the cell height was determined (Fig. 5.3.3c). A decrease in cell height after treatment with calyculin A and nocodazole alone (P = 0.0220; P = 0.0463 respectively) were observed compared to the untreated cells. Conversely, upon the sequential treatments of calyculin A and nocodazole, a significant increase in cell height was observed (P = 0.0011). Therefore, there appears to be a correlation between changes in cell height, FA size and cortical elasticity. Finally, as a further control, we also treated fibroblasts with

DMSO alone (n = 10 cells) and observed that cell heights did not vary significantly from untreated cells for all conditions ((5.347 ± 0.4186) µm and (4.729 ± 0.2041) µm, P = 0.1900).

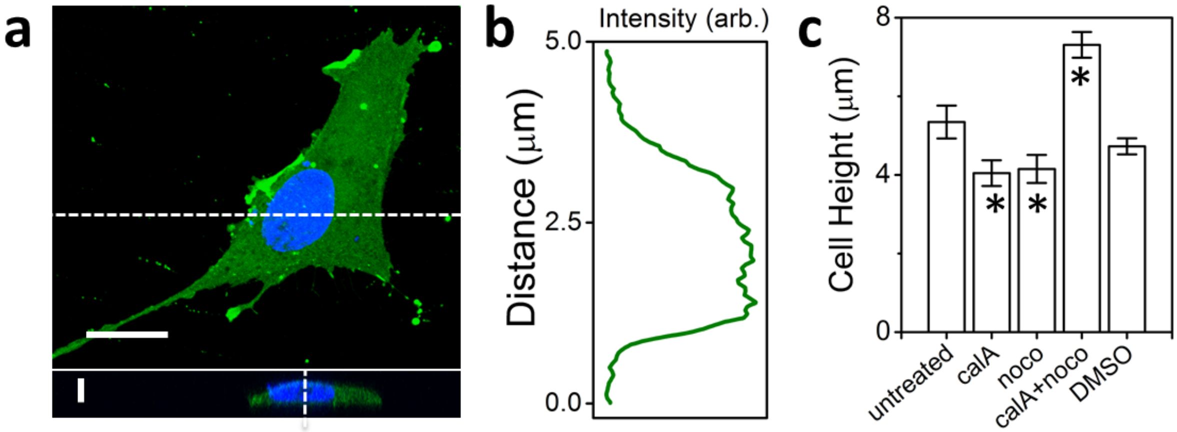

Figure 5.3.3: NIH3T3 fibroblasts undergo distinct shape changes in height after calyculin A- and nocodazole-treated cells. (a) NIH3T3 fibroblast cells were transiently transfected with the PLCδ conjugated to EGFP (PH-PLCδ-EGFP) and stained with Hoesht 33342 for the nucleus. The cells were fixed with 3.5% paraformaldehyde and imaged using a LSCM. Cell heights were measured from the Z-stacks and analyzed using ImageJ. Both channels were added together then resliced at a z-step of 0.39 µm from left-to-right and all images were projected as a maximum Z-intensity projection of the confocal planes. (b) The heights were measured by drawing a line and obtaining the intensity profile, where the half-width was measured for all as the height of the cell. (Scale bar: 20µm; xz: 6.5 µm). (c) A significant decrease in cell height for both the individually treated cells with calyculin A and nocodazole (P = 0.0220; P = 0.04629 respectively) were observed compared to the untreated cells. Conversely, upon the combined drug treatments, a significant increase in cell height was observed (P = 0.0011). As a further control, DMSO-treated cells did not vary significantly from untreated cells for all conditions ((5.347 ± 0.4186) µm and (4.729 ± 0.2041) µm, P = 0.1900).

5.3.4 Duration of treatment with calyculin A and nocodazole influences the mechanical properties of fibroblasts

To assess whether or not the duration of incubation with the drugs, either individually or in combination affects the overall mechanical response of the cells; the cortical elasticity of n =

10 cells were analyzed for 0, 5 and 30 minute incubation times with the drugs (Fig. 5.3.4). The times used here mimicked the duration of incubation used for all drugs employed in this study. Cells did not display any significant change in cortical elasticity after 5 minutes of incubation with calyculin A. However, after 30 minutes, there was a significant increase in cell elasticity ($P = 1.964 \times 10^{-13}$) (Fig. 5.3.4a) consistent with Fig. 5.3.1-2a. Cells treated with nocodazole for 5 minutes appeared significantly stiffer ($P = 2.099 \times 10^{-25}$; Fig. 5.3.4b) consistent with Fig. 5.3.1-2a. However, after 30 minutes of incubation, a significant decrease in cortical elasticity was observed ($P = 5.514 \times 10^{-16}$) along with complete MT depolymerization. Finally, cells were first treated with calyculin A for 30 minutes, producing an increase in elasticity, and then treated with nocodazole and assessed after 5 and 30 minutes. After 5 minutes of incubation with nocodozale, a significant decrease in cell cortical elasticity was observed ($P = 2.366 \times 10^{-40}$) consistent with Fig. 5.3.1-2a. The decrease in elasticity also persisted after 30 minutes of incubation ($P = 8.567 \times 10^{-22}$) and was consistent with the complete loss of intact MTs.

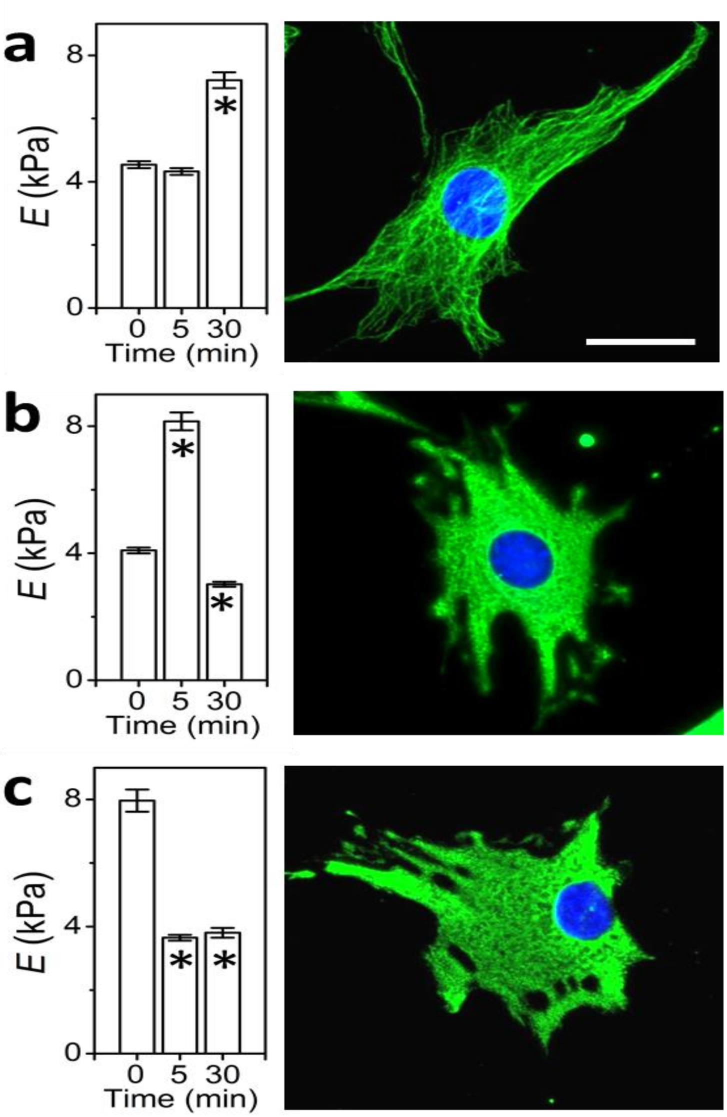

Figure 5.3.4: Duration of drug treatment influences the mechanical properties of NIH3T3 fibroblasts. To determine whether or not the duration of incubation with the drugs, either alone or in combination affects the overall mechanical response of the cells; the elasticity of the cells were analyzed at 0, 5 and 30 minutes incubation times in order to mimic all duration times used throughout the experiment. (a) Calyculin A-treated cells measured at 0 minutes appeared comparable to the untreated cells. Cells did not display any significant change in cortical elasticity after 5 minutes of incubation with calyculin A. After 30 minutes, there was a significant increase in cortical elasticity compared to the 0 minutes ($P = 1.964x10^{-13}$) along with complete MT depolymerization. (b) Cells treated with the nocodazole for 5 minutes appeared significantly stiffer ($P = 2.099x10^{-25}$); however, after 30 minutes of incubation, a significant decrease in cortical elasticity was observed ($P = 5.514x10^{-16}$) along with complete MT depolymerization. (c) Finally, cells were first treated with calyculin A for 30 minutes, producing an increase in elasticity, and then treated with nocodazole and assessed after 5 and 30 minutes. After 5 minutes of incubation with nocodozale, a significant decrease in cell elasticity was

observed ($P = 2.366x10^{-40}$). The decrease in elasticity also persisted after 30 minutes of incubation ($P = 8.567x10^{-22}$) and was consistent with the complete loss of intact MTs. Scale bar: 26μm.

5.4 Discussion

The mechanical properties of cells are becoming widely recognized as key indicators and regulators of critical physiological and pathological pathways (105, 156-158, 174, 185). Therefore, understanding the regulation and dynamics of the mechanical properties of cells has important implications for our fundamental understanding of these processes as well as potentially aiding in novel diagnostic approaches (105, 156-158, 185). Cell elasticity is determined by several cytoskeletal elements, including actin filaments, MTs and intermediate filaments (130, 186). The cytoskeletal actin network transmits forces to the extracellular matrix through integrin assemblies at cell FA contacts and can form contractile stress fibers in conjunction with myosin. MTs play a dominant role in directing tensile forces during cell division (187). Importantly, several pharmacological agents can be employed to systematically study how the mechanical properties of the cell can be modulated through the activation or inhibition of distinct pathways. Calyculin A and nocodzole are two such agents that can either enhance actomyosin contractility or depolymerize MTs, respectively (188, 189). Calyculin A is a phosphatase inhibitor which can act on myosin light chain phosphatase, leading to myosin-II hyperactivation and an increase in contractility (163, 167). On the other hand, nocodzole treatment causes the loss of intact MTs, leading to increased stress fibres and contraction over shorter timescales (171, 172, 190). For both drugs, an increase in cell cortical elasticity has been observed previously (129, 153, 162). In this study, we sought to determine the time-dependent elastic response of NIH3T3 fibroblasts when subjected to calyculin A and nocodazole, alone or in combination. We quantified the mechanical properties, FA area, projected cell area and cell height before and after drug treatments for up to 30 minutes.

Previous studies have shown that the depolymerisation of MTs and the inhibition of myosin light chain phosphatase separately in cells caused an increase in cell spreading, changes in cellular morphology and FA assembly (121, 163-165). Here, an AFM cantilever was used as a microindenter to determine the mechanical properties of the cells for shallow indentations (64, 183). In all cases, NIH3T3 fibroblasts were cultured on 0.1% GE coated plastic and subjected to drug treatments. For the untreated fibroblasts, the cell elasticity remained constant (4.703 ± 0.1727 kPa), consistent with previous measurements (64). In response to calyculin A, cells were observed to display an increased cortical elasticity after 30 minutes of treatment. Conversely, in response to nocodazole treatment, a transient increase in cortical elasticity was observed within 5 minutes of treatment followed by cortical softening within 30 minutes. The increase in cell stiffening as a result of MT disruption has been observed in cardiac fibroblasts cultured on polyacrylamide gels of varying elasticities (129) and with L929 cells under the effect of the cytoskeletal drug treatments (162). Conversely, it has also been shown that nocodozole treated cells appear softer than untreated cells (113, 170). Comparable to these observations, we found that after longer exposure times (~30 minutes) cells become softer (Fig. 4.3.4). Clearly, the drugs used in this study cause a time-dependent modulation of cortical elasticity. A longer exposure time with the drug has a greater effect in saturating any response in which the intact cytoskeleton might contribute to the overall cortical elasticity of cells. This may explain both extremes of responses that cells exhibit when treated with nocodazole in the literature. In addition, nocodazole-treated cells stimulated the formation and size of FAs (173). These results suggest that individual drug treatments of calyculin A and nocodazole play a crucial role in modulating the contractile response in cells. This behaviour was consistent with observations of changes in FA size, cell area and cell heights. The cells do not detach and they retain, in general a flattened shape where FAs are visible as shown previously (121, 167, 173). An increase in cortical elasticity was observed to occur concomitantly with an increase in FA area and a decrease in cell height. Changes in cell height are commonly observed to correlate with changes in local cortical stiffness (184), consistent with our results. In contrast to our results, it was previously shown that highly metastatic breast adenocarcinoma cells (MDA-MA-231) resulted in rounded morphologies and a decrease in actin intensity, indicative of a loss in shape (37). Together, these differences may indicate that treatment with nocodazole may result in cell-type-specific behaviors. Although the projected cell areas appeared to exhibit an interesting trend, a large degree of variability in cell areas led to a lack of any statistical significance.

Furthermore, there appears to be a surprising effect during the combined treatments of fibroblasts with calyculin A and nocodazole. Cells were initially incubated with calyculin A for 30 minutes followed with 5 minutes treatment with nocodazole. The cell elasticities were significantly lower than the untreated cells suggesting that there is an overall softening of cortical elasticity. This appears to be counter-intuitive because for both individually treated calyculin A and nocodazole cells, their respective elasticities appear to increase along with the appearance of more prominently FAs. This would lead to the prediction that a combined treatment with both drugs would cause an additive response in cell elasticity. Instead, cell elasticity and FA area were significantly lower than untreated cells. In addition, cell heights were observed to be higher than untreated cells. Therefore, the interplay between cytoskeletal remodelling and actomyosin contractility modulate FA area and cell height leading to dynamic, time-dependent changes in cortical elasticity. The relationship between FA size and cell elasticity clearly reveals the important role FAs have in governing the material properties of cells. The drop in the size and number of FAs, which are mechanically linked to actin filaments, leads to dramatic increase in cell height. Importantly, a calyculin A induced increase in contraction and cortical elasticity, clearly cannot be maintained upon the loss of MTs. It was previously shown that the inhibition of the actomyosin contractility induced the loss and reduction of FAs (167, 191); whereas FA assembly increased upon the disruption of MTs (121, 173). Our results, and previous studies, all appear to support the notion that MTs appear to play an important role in modulating cellular contractility and mechanical properties.

Taken together, results here reveal a complex interplay between cytoskeletal and FA remodelling on the mechanical properties of the cell cortex. Importantly, responses to calyculin A and nocodazole are highly time dependent. Moreover, these responses are highly dependent on cell type, concentration and the mechanical properties and biochemistry of the substrate (121, 129, 162-165, 169, 192). For example, as highlighted above, changes in cortical elasticity in response to nocodazole treatments are highly dependent on cell type

(121, 129, 162, 163, 170). In addition, here were examined the response of NIH3T3 cells cultured on GE coated plastic, whereas in previous studies, similar experiments have been performed on uncoated or functionalized surfaces (170, 193). Surface biochemistry plays a major role in modulating FA size (194, 195) and therefore, will modulate the mechanical properties of the cell and its response to pharmacological agents. Clearly the biochemical and mechanical properties of the microenvironment cannot be ignored when considering the mechanical dynamics of living cells. This is due to the complex interplay between components of the cytoarchitecture and their remodelling dynamics on any observed changes in the mechanical properties of the cell. Therefore, one must take care when considering the mechanical responses of cells to particular pharmacological agents. That being said, under the conditions in this study, we observe clear time-dependent changes in cortical elasticity in response to the activation of actomyosin contractility and MT depolymerization. The results demonstrate that MTs play a key role in modulating cortical elasticity. The loss of intact MTs clearly counteracts the effects of induced contractility on cortical elasticity. This is due to a reduction in FA size and a corresponding increase in cell height.

5.5 Conclusion

It is becoming increasingly evident that there is a very close relationship between mechanotransduction and mechanosensitivity signalling pathways in the remodelling of the cytoarchitecture in biological processes (27, 175, 176). Cells are exposed to multiple physical cues that are integrated and used to modulate cell-type specific mechanotransduction and mechanosensitivity pathways. By determining the time-dependent elastic response of NIH3T3 fibroblasts when subjected to calyculin A and nocodazole, alone or in combination, we were able to quantify the mechanical properties, FA area, projected cell area and cell height before and after the enhancement of actomyosin contractility and the depolymerisation of MTs. As demonstrated here, the loss of MTs disabled the ability of fibroblast cells to maintain increased contractility and cortical elasticity upon activation of myosin-II. Moreover, a transient increase in cortical elasticity was initially observed with nocodazole-treated cells followed by cortical softening after 30 minutes. Here, we have demonstrated how the interplay between cytoskeletal remodelling and actomyosin contractility modulate FA area and cell height leading to dynamic, time-dependent changes in cortical elasticity of NIH3T3 fibroblast cells.

5.6 Acknowledgment

This work was supported by a Natural Sciences and Engineering Research Council Discovery Grant [grant number RGPIN/355535-2009 to A.E.P.] and Discovery Accelerator Supplement [grant number RGPAS/380321-2009 to A.E.P.]; the Canada Research Chairs program [grant number 950- 206182 to A.E.P.]; and a Province of Ontario Early Researcher Award [grant number ER09-06-158 to A.E.P.]. Z.A.R. gratefully acknowledges the uOttawa NSERC CREATE program in Quantitative Biomedicine for graduate student support.

Chapter Six: Mechanotransduction inhibited in the presence of nanoforce application during contractile activation

The material in chapter five is subject of a paper in preparation.

Abstract

Increasing evidence suggests that the crosstalk between the mechanical properties of the cell and its surrounding microenvironment along with its integration of external physical forces profoundly influences key regulatory roles in many biological processes. Actomyosin contractility and microtubules (MTs) are both implicated in regulating traction force dynamics and cell mechanics in cells. Several studies have examined the effects of contractile activation-based control of traction forces; however little is known of the force-dependent response of fibroblast cells in mediating this control. Here, we directly characterized the generation of traction forces by fibroblast cells in response to contractile activation and controlled nanomechanical stimulation. Initially, we found that the individual enhancement of contractility or the depolymerisation of MTs both caused an increase in traction dynamics, FA size and a subsequent increase in cell elasticity and a concomitant decrease in cell height and area. However, the loss of MTs diminished the increase in traction force and cell elasticity in the presence of myosin-II activation compared to the individual treatments. Finally, fibroblasts responded greatly to nanomechanical stimulation only on a 51.2 ± 0.419 kPa hydrogel; however, this response disappeared when cells were subjected either to contractile activation alone or in combination. Clearly, the application of force during contractile activation inhibited the mechanotransduction response in fibroblasts grown on flexible substrates.

6.1 Introduction

Cellular response and adaptation to mechanical stresses are crucial for a broad range of cellular functions including development, homeostasis and cytoskeletal remodelling (176, 196, 197). For example, cellular differentiation not only depends on the expression of certain growth factors but also on the mechanical properties of the microenvironment (198). It is well known that the surrounding cellular microenvironment plays an important role in directing the fate of stem cells, apoptotic and mitotic progression, gene expression and regulation, as well as influencing cancerous pathologies (11, 33, 93, 104, 113, 153, 199, 200). Therefore, cells need to sense mechanical cues in their cellular microenvironment, and transduce them into biochemical signals in order to respond to them appropriately. The cell is composed of an intricate organization of highly-regulated cytoskeletal networks. These networks not only provide structural support, enabling the cell to maintain its shape and polarity, but also act as a crucial mechanism for transducing and regulating mechanical cues from the microenvironment. Furthermore, disruption of the cytoskeleton or mechanical signals, through selective removal of specific molecules, often affects the most basic functions of the cell, including: cell migration, growth, and differentiation (25).

In order to understand mechanotransduction, it is important to examine how the cytoskeleton responds to, and generates, mechanical forces (146). In particular, the actin cytoskeleton, in conjunction with the myosin-II motor protein, is responsible for the production of cellular traction forces (83, 201). Moreover, the actomyosin network and focal adhesion (FA) complexes have been implicated in transmitting mechanical forces to and from the extracellular matrix (ECM). FA complexes consist of an assembly of proteins that act to mechanically link the intricate organization of the cytoskeletal network to the ECM. FAs are highly dynamic and mechanosensitive, changing their conformation, size, and number in response to substrate elasticity and applied mechanical stimuli (202, 203). Various nanomechanical tools have shown that on the application of force, the size and force generated by the FAs are reinforced (204-206). Therefore, for proper regulation of FA assembly and traction force generation, both of which are necessary for many mechanosensitive events (11, 207, 208), many signalling factors or pathways must exist.

It was previously demonstrated that the depolymerization of actin with cytochalasin D, and direct inhibition of myosin-II with blebbistatin both resulted in decreased traction forces (163, 167, 191). In contrast, calyculin A, a compound used to increase myosin-II contractility, resulted in an increase in the assembly of FAs (166, 167), which evidently led to an increase in traction forces (153, 168), and cell elasticity (153). Interestingly, microtubules (MTs) have also been implicated in regulating traction forces in the cell, suggesting that MTs play crucial roles in cell morphology, migration and adhesion (121, 209). Previous studies have shown direct mechanical coupling between the actin and MT cytoskeletons (210). It was recently found that MTs play a dominant role in governing the size, assembly and disassembly of FAs (121, 173), which directly correlated with traction force dynamics (202). Moreover, MT depolymerisation has been shown to result in an increase in magnitude of cellular traction forces through two distinct pathways (121). It is now evident that both MTs and actomyosin contractility are involved in regulating traction forces and FA size in living cells. Therefore, two possible pathways exist which can lead to increased traction forces: MT depolymerisation (Fig. 6.1a) or actomyosin activation (Fig. 6.1b). In addition, cells subjected to mechanical forces and strains also undergo cytoskeletal remodelling, FA remodelling and traction force dynamics (34, 170, 202). It has been shown that nanomechanical stimulation of cells with the atomic force microscope (AFM) can lead to rapid remodelling of the actin cytoskeleton, organelles and FA remodelling (113, 170, 211, 212). Therefore, despite the ability to stimulate traction forces by increasing cell contractility with pharmacological agents, it still remains unclear how local nanomechanical stimulation alters traction force dynamics. Moreover, it is also unclear if a cell in an activated contractile state will display traction force responses to nanomechanical stimulation.

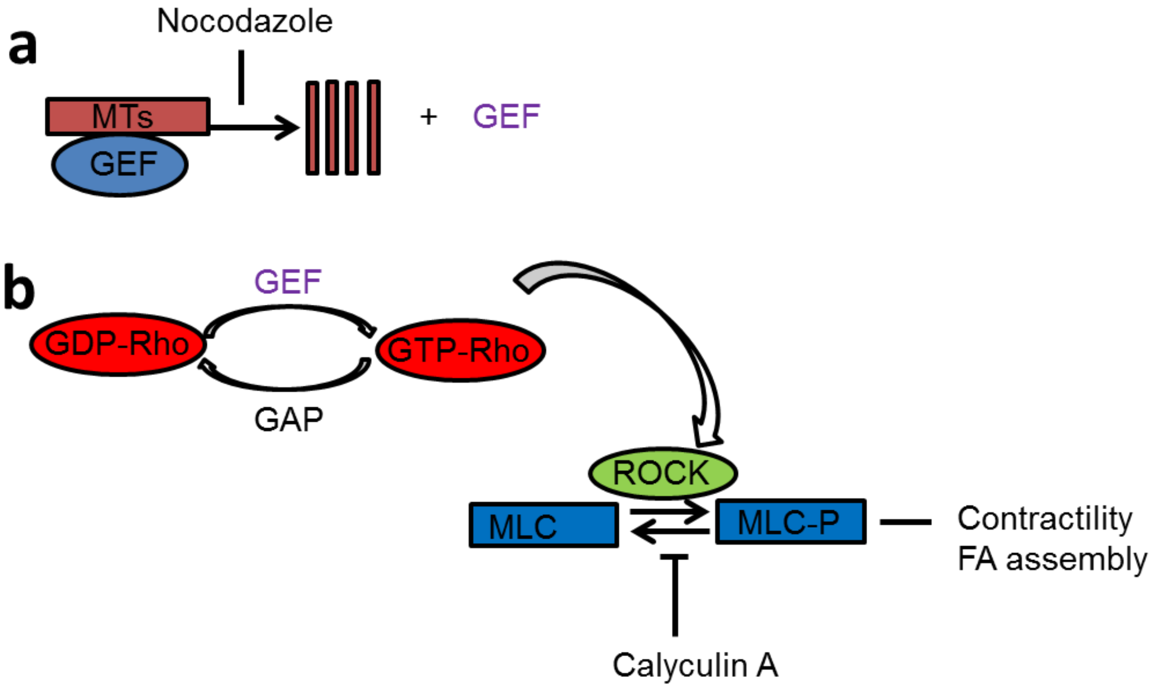

Figure 6.1: Two possible pathways that are involved in contractile activation. (a) Nocodazole depolymerizes MTs, which releases the GEF molecule, which further increases the level of GTP-bound active Rho. This action stimulates ROCKs, which stimulates actomyosin contractility leading to the assembly of FAs.

(b) The rho pathway is involved in the regulation of actomyosin contractility leading to the assembly of FAs. Calyculin A augments the activity of myosin-II inhibiting myosin light chain phosphatase, leading to the enhancement of myosin phosphatase and hence increasing cellular contractility and FA assembly.

Here, we examined how activation of contractility (through myosin-II activation or MT depolymerization) modulates traction forces in the presence of nanomechanical stimulation. We combined atomic force microscopy (AFM) and traction force microscopy (TFM) to directly characterize the generation of traction forces by NIH3T3 fibroblast cells in response to contractile activation and controlled nanomechanical stimulation. Importantly, NIH3T3 cells were found to respond optimally to nanomechanical stimulation (10 nN) on substrates with an elasticity of 51.2 ± 0.419 kPa. Cells treated with calyculin A and nocodazole either alone or in combination were also investigated in order to examine the effect of contractile activation on mechanotransduction, cell mechanics, FA morphology and cell area. Treatments all resulted in an increase in traction forces compared to controls, as expected. However, the loss of MTs diminished the increase in traction force and cell elasticity in response to myosin-II activation compared to the individual treatments. Interestingly however, cells no longer displayed any response to nanomechanical stimulation with AFM. The lack of an increase in traction force in response to nanomechanical stimulation indicated that cells in an activated contractile state lose the mechanotrasduction response, implying that there is no further increase in their basal traction force generation. Moreover, the loss of MTs diminished any increase in traction force in the presence of myosin-II compared to the individual treatments. Therefore, our results suggest that there indeed exists a complex relationship between the actomyosin phosphorylation pathway and the MT network with local traction dynamics and mechanical stimulation. The data presented here provides greater insight on the complex interplay between the cytoskeletal and FA remodelling that control and mediate the traction dynamics and mechanical properties of the cells in relation to its surrounding mechanical microenvironment.

6.2 Materials and Methods

6.2.1 Fabrication of Glutaraldehyde Cross-Linked Gelatine (GXG) Substrates

A Porcine Type-A Gelatine (GE) (Sigma-Aldrich) solution was made by autoclaving 4-7% GE in distilled water. Green fluorescent beads (Invitrogen) were added to 1 mL GE at a 1:200 dilution and this solution was cross-linked with 50% Glutaraldehyde (Sigma-Aldrich) (GA) to a final concentration of 0.5%. The solution (1 ml) was spread evenly over the surface of a 35 mm plastic culture dish. The dishes were placed in a humidity chamber and stored in the refrigerator overnight. The next day, $NaBH_4$ (1 mg/mL in ice cold phosphate Buffer Saline (PBS) made immediately before use) was used to reduce any unreacted GA for 1 hr on ice. The final plates were then rinsed with cold PBS, UV sterilized for 1 minute (Spectroline UV Crosslinker Select Series) and then filled with culture media. The plates were placed in the tissue culture incubator for 4hrs prior to seeding cells and the next day they were used for experiments.

6.2.2 Cell Culture and Reagents

NIH3T3 mouse fibroblast cells were maintained in a 37°C, 5% CO_2 incubator and cultured in DMEM with 10% fetal bovine serum and 1% streptomycin/penicillin (all from Hyclone Laboratories Inc.). All the experiments were performed 24 hrs after cells were cultured on 5% GXG at a density of $\sim 10^5$ cells/cm^2. All drugs (Sigma) used here were stored as stock solutions in DMSO at -20ºC. Calyculin A was used at a final concentration of 1 nM and nocodozole was used at a final concentration of 10 µM. The concentrations were chosen based on commonly employed values in literature (163).

6.2.3 Immunofluorescent Staining

All the immunofluorescence staining was carried out as described previously (113) but with some minor modifications to the protocols. The actin filaments were stained with Phalloidin Alexa Fluor 546 (Invitrogen), and the nuclei stained with DAPI (Invitrogen). The FA protein, vinculin was labelled with a monoclonal anti-vinculin primary antibody produced in mouse (Invitrogen) and a rabbit anti-mouse IgG secondary (Invitrogen) antibody conjugated to AlexaFluor 488 fluorophore (each used at a 1:500 dilution). After each step cells were incubated with wash buffer for 15 minutes (5% Horse Serum (Sigma)). Concerning the MT stains, fibroblasts were fixed and permeabilized with -20˚C methanol and immediately placed on ice for 3 minutes. The methanol was quickly removed and cells were washed and incubated with the wash buffer for 15 minutes. MT filaments were labelled with a monoclonal alpha-tubulin primary antibody produced in mouse (Invitrogen) and a rabbit anti-mouse IgG secondary (Invitrogen) antibody conjugated to AlexaFluor 488 fluorophore (each used at a 1:200 dilution). All samples to be imaged were then mounted in vectashield (Vector Labs) and a glass coverslip placed on top. The imaging were all carried out on an A1R high speed laser scanning confocal microscope (LSCM) using a 60X water immersion objective (Nikon, Canada). The final post-processing of all images was carried out with ImageJ.

6.2.4 Atomic Force Microscopy

For all the AFM experiments, an AFM (Nanowizard II, JPK Instruments, Germany) was used with PNP-TR-50 cantilevers (Nanoworld) with spring constants of 69±6 pN/nm (Average±SD). For the cell elasticity experiments with the drugs: 2 cells were randomly chosen in n = 10 plates and 5 - 15 force curves were collected on each cell over the center of the nucleus. In addition, the AFM measurements were obtained in ± 2 mins. The local mechanical properties of the cells were determined by analyzing the force curves, which were measured at 1Hz, with the Sneddon Model for a conical indenter at an indentation of 200 nm as described previously (56, 170). The half angle of the AFM tip was 35º and Poisson ratio of 0.5. The data analysis was carried out using the PUNIAS software (182). In addition, force-volume elasticity maps of the GXG substrates were acquired in the 'force mapping' mode. Force maps were acquired over a 32 x 32 pixel scan area and the elasticity was determined as described above.

6.2.5 Rheology

The viscoelastic properties of 5% GXG substrates were quantified by measuring their dynamic shear moduli using an Anton-Paar MCR 301 Rheometer (Paar Physica). This rheometer uses a drag cup motor and optical encoder to measure torque, θ, and γ, as explained in appendix D. The rheometer utilizes disposable, 25 mm diameter, circular top plates and specialized bottom plates, both designed by Dr. James Harden. These plates were sand-blasted to create a rough surface. This rough surface was used to minimize the amount of slippage that could occur between the plates and the samples as slip between the two causes a lower stress to be observed for a certain strain. Here, GXG substrates were produced with at least 1.6 mm thickness. A round cutter was used to cut the sample so that it fit between the two 25 mm stainless steel parallel plates. Surgical glue was used to glue the round piece of GXG onto the bottom steel plate. The top plate was also glued so that it sandwiched the thick sample of GXG. Excess sample was removed via a razor. A procedure was performed before each test to determine the height between the two plates. This procedure uses a normal force sensor which measures deflections in the air bearing and a resultant difference in capacitance, allowing the normal force to be calculated. Thus, the height between the two plates can be determined by slowly lowering the rheometer's top plate until a normal force is detected. At this point the height of the upper plate is slowly increased until no more normal force is measured. Standardizing the height ensures the sample volume is similar between different samples. The shear storage modulus G' was determined from the shear stress in phase with an oscillatory (10 rad/s) shear strain of 0.25% maximal amplitude, by standard techniques.

6.2.6 Atomic and Traction Force Microscopy

By mounting the AFM on a Nikon Eclipse TiE epi-fluorescence and phase contrast microscope (Nikon, Canada), simultaneous AFM and TFM measurements were performed. The TFM was performed by acquiring both paired phase contrast and fluorescence images of the cell and the bead positions respectively, using a CCD camera (Photometric Cool Snap HQ^2) and a 40X, NA 0.65 objective lens. This was then repeated; however this time the cell was exposed to a constant 10nN force from the AFM tip. This approach allowed us to examine the change in traction force in response to an externally applied nanomechanical stimuli and to compare it to its built-in control (mechanically unstimulated case). 1 cell was randomly chosen from n = 20 plates. The null image was obtained by removing the cell from the substrate with 10 mM EDTA, allowing us to measure the average traction force generated by fibroblasts. This was obtained by dissolving EDTA in PBS without Ca^{2+} and Mg^{2+}, the pH was brought down to 7-8 by adding 0.02 M Acetic acid. Therefore, we ensured that every fibroblast cell measured possessed a built-in control. The cells were maintained at 37°C with a microscope stage petri dish heater (JPK Instruments). The tracking and registration was performed with the well-described and commonly employed optical flow registration algorithms and LIBTRC libraries, which were kindly provided to us by Micah Dembo, Boston University (67, 115). Origin 8.5 was used to generate the traction heat maps.

6.2.7 Morphological Quantification

Post-processing of the images was all carried out in ImageJ. The FA images were all thresholded and subsequently segmented using available ImageJ plugins. In addition, the maximum intensity projections of LSCM images were used to quantify cell spreading area. LSCM volumes were used to quantify cell heights.

6.2.8 Statistical Analysis

All values are presented as the average ± s.e.m. A two-sample t-test ($P < 0.05$) was performed to determine significance.

6.3 Results

6.3.1 Characterization of the mechanical properties of glutaraldehyde cross-linked gelatine substrates

Glutaraldehyde crosslinked gelatine (GXG) substrates were prepared by embedding 200 nm fluorescent beads in them and culturing NIH3T3 mouse fibroblasts on those hydrogels. Generally, polyacrylamide (PA) gels have been commonly employed in TFM studies, however; several other materials, including gelatine, have been utilized with much success (116-119). The GXG substrates fabricated here, were both thick (500 µm) and optically clear. Initially, four GXG substrates were produced (4-7% w/v) and the local mechanical properties of each gel was characterized with an AFM, where we observed an increase in the local mechanical elasticity 23.5 ± 0.278 kPa, 51.2 ± 0.419 kPa, 63.8 ± 0.534 kPa and 89.4 ± 0.679 kPa (Fig. 6.3.1a). Moreover, it was found that the elasticities of fibroblast cells were not dependent on the elasticity of the GXG substrates (64). Untreated fibroblasts cells were observed to possess a local elasticity of 4.22 ± 0.168 kPa on all GXG hydrogels (Fig. 6.3.1a).

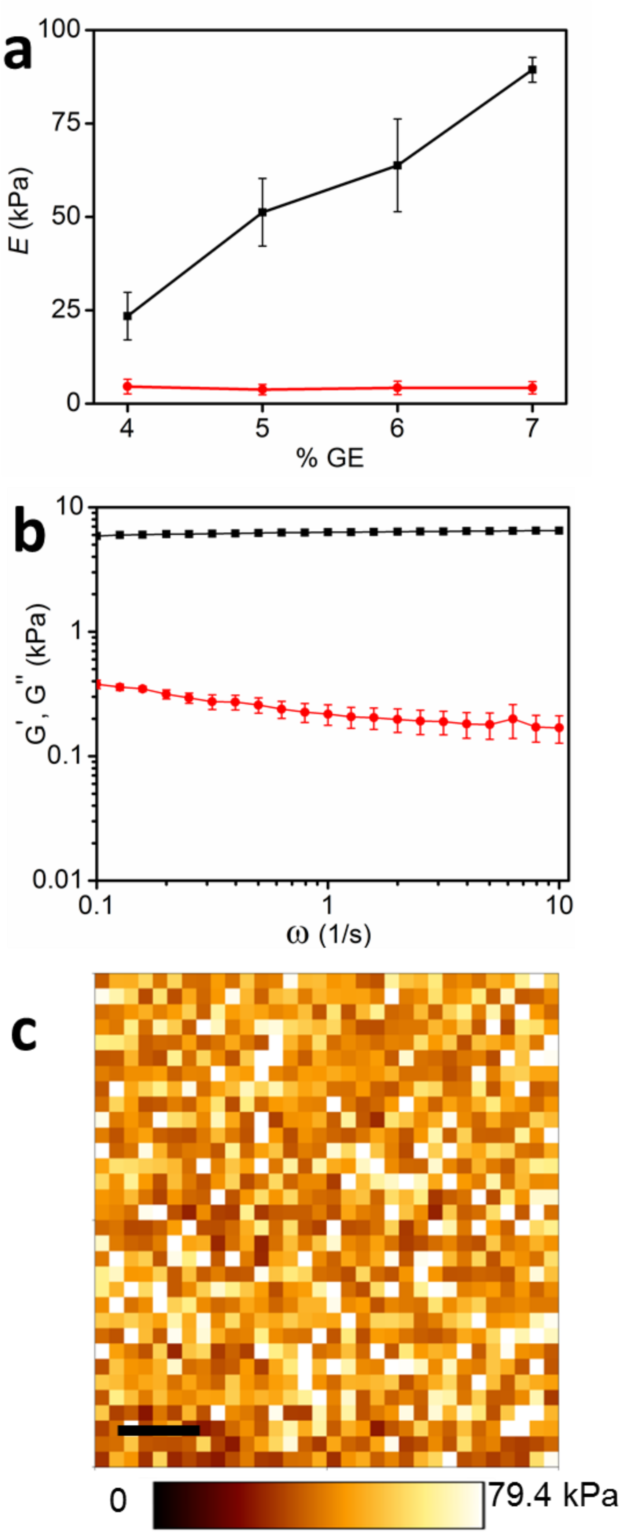

Figure. 6.3.1: Mechanical characterization of GXG hydrogel. (a) NIH3T3 fibroblasts were seeded on four GXG substrates that were produced with an increasing amount of gelatin (4-7% w/v) allowing us to control the elasticity from ~23-89 kPa (23.5 ± 0.278 kPa, 51.2 ± 0.419 kPa, 63.8 ± 0.534 kPa and 89.4 ± 0.679 kPa; black

squares). However, the mechanical properties of the cell were not affected by increasing substrate elasticity and remained relatively constant at 4.22 ± 0.168 kPa (red circles). (b) Rheological data of a 5% GXG substrate (n = 3) showing an average shear modulus of 6.26 ± 0.039 kPa. The log-log plot of the $G^{'}$ (storage modulus; black squares) and $G^{''}$ (the loss modulus; red circles) as a function of angular frequency ω at 37°C reveals that the gel behaves as a linearly elastic solid. AFM force-volume elasticity maps of (c) a GXG substrate (51.2 ± 0.419 kPa) revealed that the local mechanical properties of the GXG hydrogels were spatially homogeneous. Scale bar = 2μm. All values are average ± s.e.m.

The local mechanical properties of GXG hydrogels were further examined by comparing the elasticities obtained from AFM indentation of the hydrogels to values of shear modulus determined by bulk rheology (213) (Fig. 6.3.1b). The rheological data confirmed that the GXG hydrogels behaved as linear elastic materials (n = 3). Finally, AFM force-volume imaging of the GXG substrates revealed a relatively smooth surface with homogeneous elasticity as measured with force-volume imaging (Fig. 6.3.1c). Taken together, the results demonstrate that the GXG substrates have spatially uniform mechanical properties and that the average values are a good estimate of the overall elasticity of the substrate.

6.3.2 Traction force dynamics of fibroblast cells during contractile activation

In this study we examined the activation of two contractility pathways through the activation of myosin-II (calyculin A treatment) or depolymerization of MTs (nocodazole treatment). To investigate the role of traction force generation of NIH3T3 fibroblasts under the influence of the individual or combined drug treatments, cells were cultured on the compliant GXG substrates. This allowed us to examine the response of fibroblasts to a nanomechanical stimulus in a microenvironment of varying elasticity and to compare it to its built-in control (mechanically unstimulated treated case). In the absence of a nanomechanical stimulus, the average traction force generated by the cells remained constant for the 4-7% GXG substrates (23.5 ± 0.278 kPa, 51.2 ± 0.419 kPa, 63.8 ± 0.534 kPa and 89.4 ± 0.679 kPa; n = 10 – 15 cells). Moreover, NIH3T3 fibroblasts responded significantly to a nanomechanical stimulus of 10 nN only on the 5% GXG (51.2 ± 0.419 kPa) substrates compared to all others ($P = 5.52 \times 10^{-4}$: Fig. 6.3.2a and P = 0.023: Fig. 6.3.2b). The application of force to cells on the 51.2 ±

0.419 kPa caused a significant increase in the magnitude of local traction force as shown by fig. 6.3.2d compared to the nanomechanically unstimulated case (Fig. 6.3.2c). Therefore, the 5% GXG substrate was chosen as the optimal substrate elasticity for probing mechanotransduction and was used exclusively throughout the rest of this study.

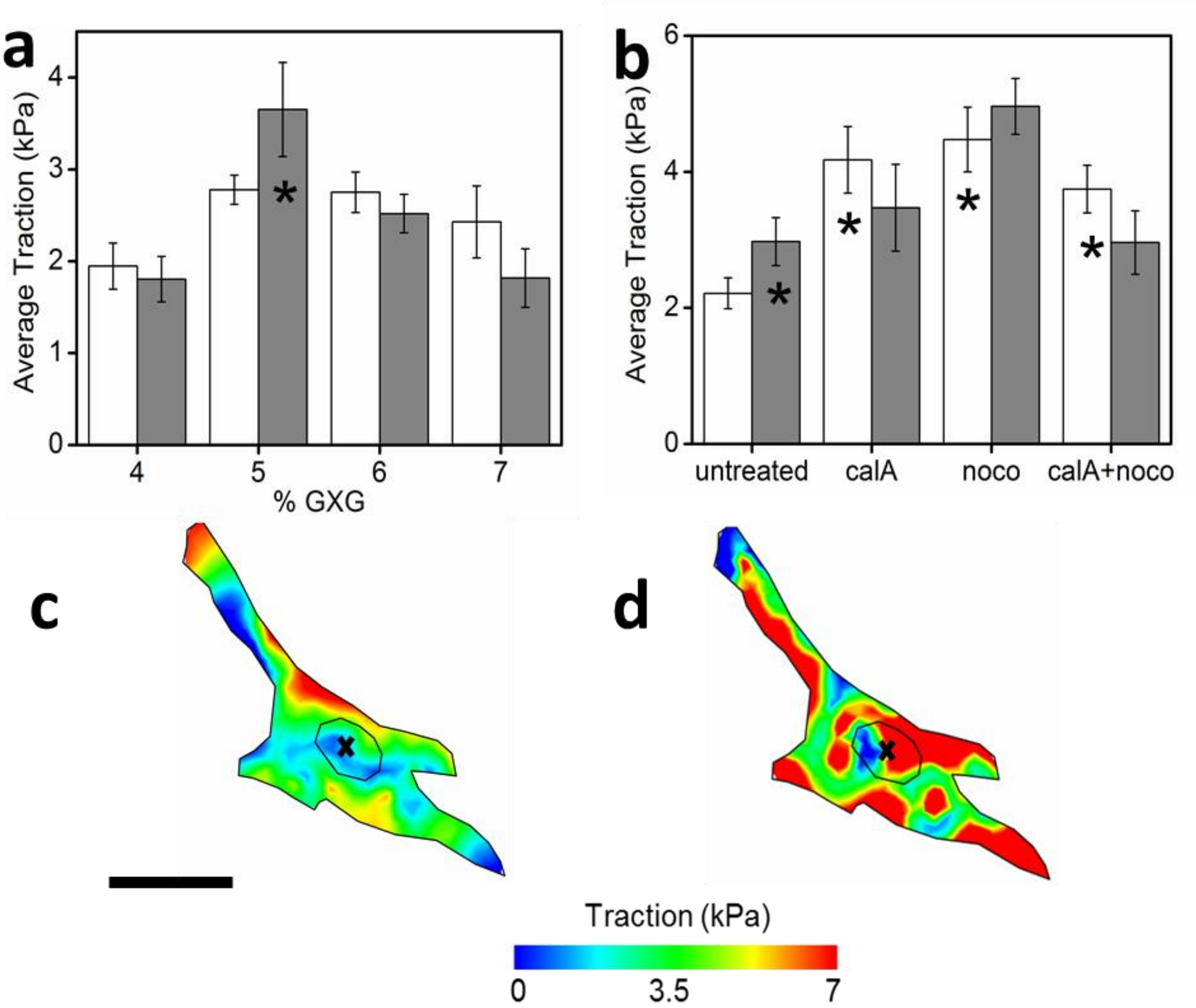

Figure 6.3.2: Average traction force for fibroblasts. (a) Examining the response of fibroblasts to a nanomechanical stimulus in a microenvironment of varying elasticities, four GXG substrates were produced with an increasing amount of gelatin (4-7% w/v) allowing us to control the elasticity from ~23-89 kPa. NIH3T3 responded greatly to a 5% GXG (51.2 ± 0.419 kPa) when stimulated with a 10nN nanomechanical force compared to the unstimulated case (* $P < 0.05$); whereas for the unstimulated cells cultured on the 4-7% GXG, the average traction force generated by the cells remained constant. The corresponding heat maps were obtained for untreated cells cultured on the 51.2 ± 0.419 kPa hydrogel before (c) and after (d) force application. (b) Fibroblasts cultured on 51.2 ± 0.419 kPa substrate generated a significant increase in traction force when

treated with calyculin A and nocodazole individually or in combination compared to the untreated case (* $P < 0.05$). When a 10nN force was applied to cells on the 51.2 ± 0.419 kPa during the individual or combine drug treatments, there were no observed significance in the magnitude of traction force compared to their built-in controls. The only observed increase in the presence of nanomechanical stimulation with 10nN was found with the untreated case (* $P < 0.05$). Scale bar: 30µm.

After processing the data, an average traction force was calculated for each drug treatment ($n = 8 – 14$). Fibroblasts grown on the 51.2 ± 0.419 kPa GXG substrate were either individually treated with calyculin A or nocodazole for 30 minutes and 5 minutes respectively or subjected to a sequential stimulation of both drugs, starting with calyculin A for 30 minutes followed by nocodazole for 5 minutes. What becomes evident is that fibroblasts generate a significant increase in traction force when treated with individual ($P = 0.001$, $P = 1.29\text{x}10^{-4}$; for calyculin A and nocodazole respectively) and combined drugs of calyculin A and nocodazole ($P = 9.15\text{x}10^{-8}$) compared to untreated cells (Fig. 6.3.2b). Finally, the average traction force measured for the stimulated cells displayed no significant change from their built-in controls during contractile activation ($P > 0.1$ in all cases), suggesting that during the stimulation of fibroblasts with the drug treatments the cells no longer generated an increase in traction forces, since there was no observed change in their force generation even after being subjected to an additional external nanomechanical stimuli.

6.3.3 Changes in cell elasticity in response to calyculin A and nocodazole treatments

In order to examine the effect of these drugs either alone or in combination on the mechanical properties of fibroblasts, the local cell elasticity of the cells were obtained with AFM (183). Untreated cells were observed to possess a local cell elasticity of 3.78 ± 0.119 kPa (Fig. 6.3.3a). After the drug treatments, the mechanical properties of NIH3T3 fibroblast cells assessed with AFM ($n = 19 - 20$ cells). When cells were treated with calyculin A or nocodazole alone, there was a significant increase observed in cell elasticity ($P = 5.50\text{x}10^{-8}$ and $= 1.67\text{x}10^{-8}$, respectively; Fig. 6.3.3). The effect of the sequential stimulation with calyculin A and nocodazole was investigated. For these cells cultured on a compliant surface, a significant increase ($P = 4.87x10^{-13}$) in cell elasticity was observed compared to the untreated cells.

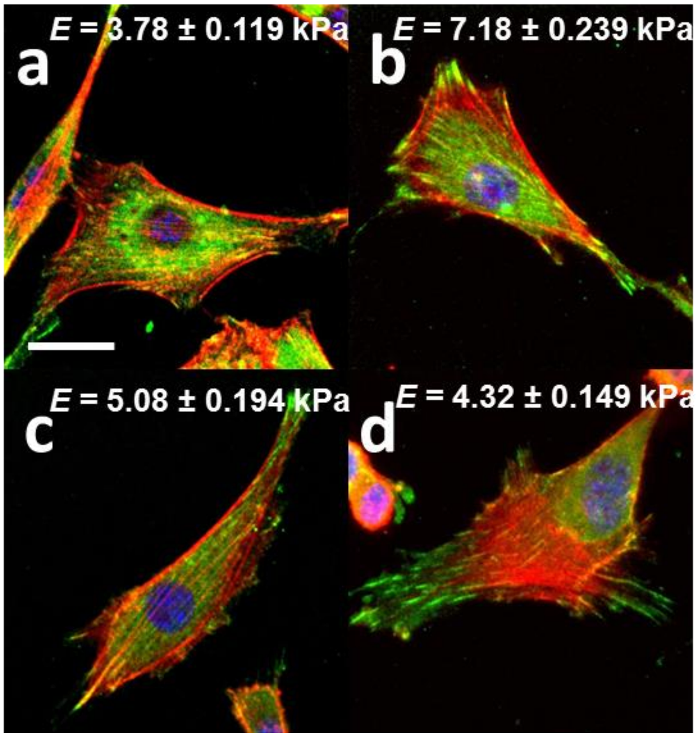

Figure 6.3.3: Immunofluorescent images and cell elasticity of NIH3T3 fibroblast cells following treatments with calyculin A and nocodazole alone or in combination. LSCM images were taken to visualize the changes in the size of vinculin-rich FAs and actin filaments in fibroblast cells. Cells were cultured on 51.2 ± 0.419 kPa GXG substrate and they were fixed and stained for vinculin (green), actin filaments (red) and DNA (blue). Treatment with calyculin A (b) and nocodazole alone (c) or in combination (d) increased the cell elasticity from ~ 7.2 kPa to ~5 kPa and ~4 kPa respectively compared to the untreated (a). Scale bar = 26μm, applies to all.

6.3.4 Morphological changes in response to calyculin A and nocodazole treatments

NIH3T3 mouse fibroblast cells were cultured on a compliant GXG surfaces, and then treated with each agent either individually or in combination. LSCM images of actin and vinculin were acquired in order to visualize changes in the cytoskeletal and FA structure relative to the untreated cells (Fig. 6.3.3). The untreated fibroblasts appeared to be well spread with prominent FAs and actin filaments (Fig. 6.3.3a). Calyculin A-treated cells also appeared to be well spread with more elongated FAs and well-defined actin filaments (Fig. 6.3.3b). In addition, both the actin filaments and FAs remained intact and prominent for the nocodazole-treated fibroblast cells (Fig. 6.3.3c). Upon the sequential combination of calyculin A and nocodazole, a similar observation was seen, where FAs appeared more prominent than the untreated cells (Fig. 6.3.3d).

To assess the effect of contractile activation using calyculin A and nocodazole alone or in combination on the MT cytoskeleton, fibroblasts cultured on a flexible substrate were stained for the MTs and imaged with LSCM. After 30 minutes of calyculin A treatment, MTs remained intact and fibrous, similar to the untreated case (Fig 6.3.4-1b). However, after nocodazole treatments for 5 minutes, most of the MT networks were disrupted with a few intact filaments still visible (Fig. 6.3.4-1c). Finally, after exposing the cells to a sequential incubation with calyculin A and nocodazole, a similar observation was seen in which the majority of MTs were depolymerized leaving only a few intact filaments in the cell (Fig. 6.3.4-1d).

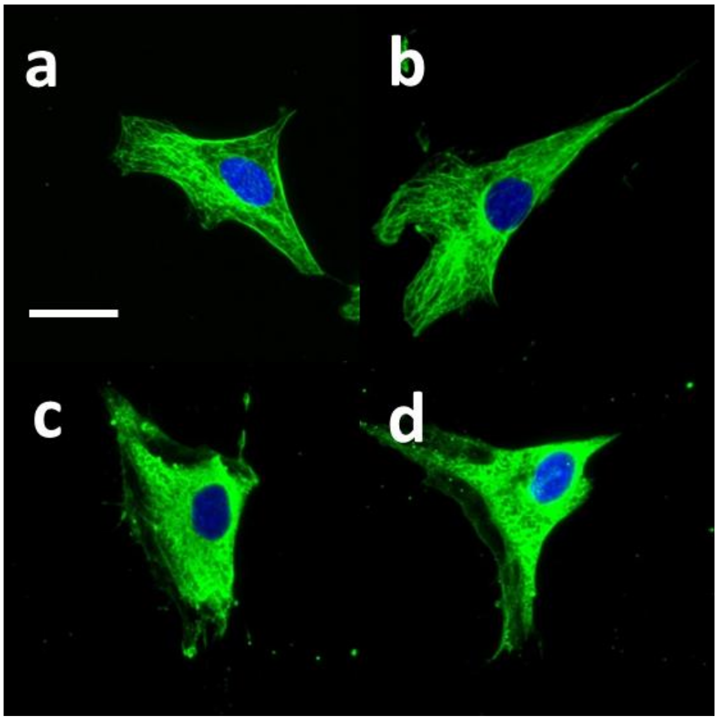

Figure 6.3.4-1: Morphological alteration in MT distribution for calyculin A- and nocodzole-treated cells alone or in combination. MTs are clearly intact in untreated (A) and calyculin A-treated cells (b). Exposure to nocodzole, alone (c) or in combination with calyculin A (d), caused a significant depolymerization of the majority of MT filaments. Scale bar = 26μm, applies to all.

In order to evaluate the effect of these drugs on cell morphology, both the FA and cell areas were investigated and quantified for the individual and combined treatments of calyculin A and nocodazole. Here, LSCM images were obtained and post-processed by segmentation. For cells cultured on 5% GE, FA area increased significantly for calyculin A-treated cells (P = 0.021) compared to the untreated fibroblasts (Fig. 6.3.4-2a) (n = 7 - 8 cells, with ~148 FAs analyzed in total). The effect of nocodazole-treated fibroblasts revealed a significant increase in FA area ($P = 5.74x10^{-4}$). Clearly, the depolymerisation of MTs stimulates the formation and size of FAs (121, 173). After sequential treatment with both drugs, the FA area increased significantly ($P = 1.16x10^{-4}$). Interestingly, there was a significant reduction in cell spreading even though the traction force and FA area increased for the individual (P = 0.030 calyculin A; P = 0.004 nocodazole) and combined drug treatments (P = 0.011; Fig. 6.3.4-2b) (n = 7 - 9 cells). Taken together, the results here suggest that the FA size directly compares with both the traction dynamics and cell mechanics of fibroblasts.

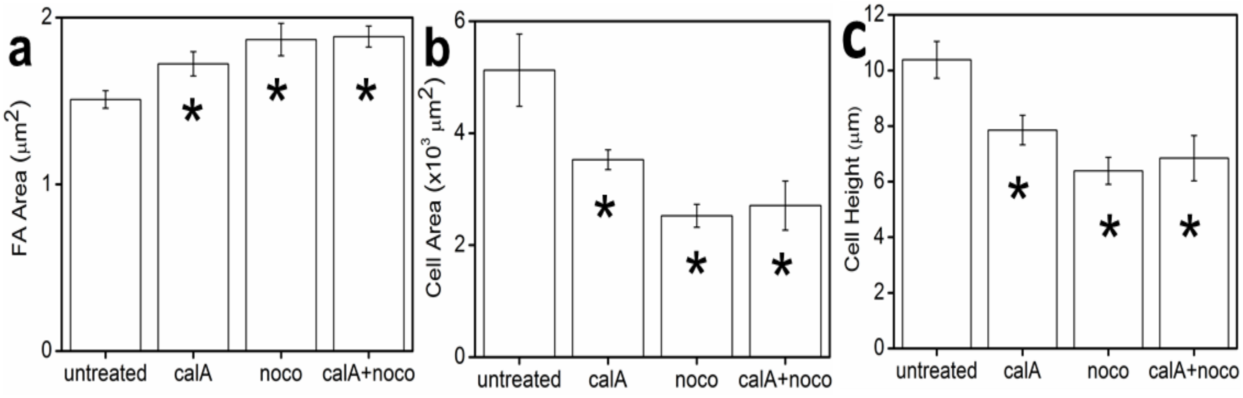

Figure 6.3.4-2: FA, projected cell heights and areas under drug treatments. (a) Calyculin A or nocodazole alone caused an increase in FA area for all drug conditions compared to the untreated cells (* $P < 0.05$). (b) Changes in projected cell area in response to each drug treatment decreased significantly compared to the untreated (* $P < 0.05$). In addition, cell height (c) decreased significantly for all conditions compared to the untreated case (* $P < 0.05$).

Finally, cell height has been previously shown to influence the observed cell elasticity (184). To examine the effect of the drugs on cell height, LSCM images were acquired for all conditions here (n = 5 - 10 cells) and the cell height was determined using segmentation. Both a decrease in cell height after treatment with calyculin A and nocodazole alone ($P = 0.013$; $P = 3.87\times10^{-4}$ respectively) were observed compared to the untreated cells (Fig. 6.3.4-2c). In addition, upon the sequential treatments of calyculin A and nocodazole, a significant decrease in cell height was also observed ($P = 0.013$). Therefore, a correlation appears to exist between changes in cell height, cell area, FA size, cell elasticity and traction force dynamics in NIH3T3 fibroblasts when cultured on flexible substrate.

6.4 Discussion

Cells are constantly subjected to a variety of mechanical signals arising in the microenvironment, including the mechanical properties as substrate elasticity or the exposure to mechanical force. In adherent cells, forces are generated within the actin cytoskeletal network and are transmitted to extracellular matrix via FA contacts. Two inhibitory drugs, calyculin A and nocodzole can be employed to investigate how nanomechanical stimulation effects traction force dynamics in fibroblast cells through the activation of the actomyosin contractility network or depolymerisation of MTs, respectively (163). Calyculin A inhibits myosin light chain phosphatase, leading to the enhancement of myosin phosphatase and hence an increase in contractility (163, 167). Conversely, over shorter timescales, nocodzole treatment disrupts intact MTs, leading to both increased stress fibres and contraction (171, 172, 190).

In this study, we investigated the traction force dynamics and elastic response of NIH3T3 fibroblasts cultured on flexible substrates when subjected to calyculin A and nocodazole, alone or in combination. We quantified the traction dynamics, mechanical properties, FA area, projected cell area and height before and after drug treatments. We combined both AFM and phase contrast/fluorescence microscopy to simultaneously apply controlled local nanomechanical stimulation to a cell while performing TFM. The gel used here was characterized by both an AFM and a rheometer. The AFM confirmed that the mechanical properties of the gel were spatially uniform and that the average values obtained were a good estimate of the overall elasticity of the substrate. Moreover, for the rheological data, the slope of the storage modulus curve (G') was nearly 0, which implied that the GXG substrate behaved as a linear elastic solid. The rheometer better characterizes the three dimensional material properties; however, it is thought that cells sense the surface properties, rather than the bulk properties (25, 26). Generally, rheometers measure the bulk or shear modulus of a material of at least 1 mm (> 1.6 mm for 5% gel) in thickness, while AFM provides a local measurement of the material usually of thin samples of less than 500 µm. It was previously shown that the mechanical property of a compliant polyacrylamide gel measured with a ball indentation technique was considerably stiffer (77) than the same gel measured with an AFM (26). That is because the former technique utilized a spherical steel ball of different diameters (0.64 mm, 1 mm and 2 mm), which covered a greater surface area of the material whereas the latter used either a spherical or conical tip usually with radii in the microns or nanometer range respectively, and hence provided a more localized characterization of the material.

Several flexible hydrogels were fabricated and fibroblast cells exerted the greatest traction forces in the presence of a constant 10 nN nanomechanical stimulus when grown on the substrate with an elasticity of 51.2 ± 0.419 kPa. Moreover, there was no significant response seen on the other substrates under the application of force. Therefore, under the conditions of this study, a 51.2 ± 0.419kPa substrate was considered the optimal elasticity for mechanotransduction to take place. In addition, untreated cell elasticity remained softer (4.22 ± 0.168 kPa) than their substrate elasticity (51.2 ± 0.419 kPa) presumably because cells reach a limit in their mechanism by which they reinforce their cytoskeleton and hence both the traction force generated on all substrates (in the absence of an external mechanical stimuli; Fig. 5.3.2a) and cell elasticity (Fig. 5.3.1a) remained constant (64, 127, 128).

In response to calyculin A, cells were observed to display increased traction force and cell elasticity after 30 minutes of treatment. It was previously shown that highly metastatic breast adenocarcinoma cells (MDA-MA-231) generated greater traction force when myosin-II activity was augmented with calyculin A (163). However, in response to local 10nN nanomechanical stimulation with an AFM, we observed no clear increase in the average traction magnitude by fibroblasts during calyculin A treatment. This suggests that during the enhancement of the actomyosin contractility (calyculin A), fibroblasts no longer generate an increase in their basal level of traction and hence regardless of an additional nanomechanical stimulation, there is no further increase. In addition, in response to nocodazole treatment, an increase in traction force and cell elasticity was also observed within 5 minutes of treatment. The increase in cell elasticity as a result of MT disruption has been observed in other cell types cultured either on polyacrylamide gels of varying elasticities (129) or under the effect of pharmacological drugs targeting the cytoskeleton (162). Conversely, it has also been shown that longer exposure times with nocodozole caused the cells to appear much softer than the untreated cells (113, 170). Therefore, local cell elasticity when measured with AFM is highly dependent on the exposure time to nocodazole. In addition, the cell area decreased whereas the size of FAs increased suggesting that nocodazole stimulates the growth of FAs (173), inducing an increase in traction force generation. Generally, the rigidity of MTs may be responsible for the absorption of some of the contractile forces from the actin cytoskeleton hence limiting the complete transmission of the forces to the substrate. However, when MTs are depolymerized, this absorbed mechanical load can be transmitted to the microenvironment through the FAs (210). Interestingly, cells no longer displayed any response to mechanical stimulation with AFM compared to their built-in controls. This observed lack of an increase in traction force in response to nanomechanical stimulation clearly suggests that cells in an activated contractile state lose their mechanotransduction response. Therefore, although mechanotransduction occurred on a 51.2 ± 0.419 kPa substrate the response disappeared in the presence of contractile activation. It was previously shown that an externally applied strain modulated the assembly of MTs (214). Moreover, prolonged treatment with nocodazole in smooth muscle cells before strain application greatly altered the membrane-associated RhoA and Rac after applied strain (215), which implied that the force-mediated regulation of Rho GTPases required force-induced changes in MT polymerization. In contrast, it was previously shown that disruption of MTs had no significant effect on FA size implying that for stationary and geometrically constrained cells less FAs were stimulated (121); whereas in our study, the fibroblasts were geometrically unconstrained. Moreover, in another case no apparent change in the organization of the actin filaments or traction forces were observed when MTs were depolymerized (216). These results suggest that individual drug treatments of calyculin A and nocodazole are highly dependent on cell type, surface conditions and type of force applied in modulating the contractile response in cells.

Furthermore, there appears to be a diminished response for both the traction force and cell elasticity during the combined treatments compared to the individual drug treatments upon the activation of myosin-II. Initially, fibroblasts were incubated with calyculin A for 30 minutes followed by 5 minutes treatment with nocodazole. Cells generated greater traction force compared to untreated cells; however the response was diminished compared to the individual treatments. Interestingly, like the individual drug treatments with calyculin A and nocodazole, there was no observed increase in traction force when nanomechanically stimulated with a 10 nN force from the AFM. This behaviour may be due to the fact under the combined activation of contractility, cells are generating an increase in basal level of traction and that additional nanomechanical stimulation results in no further increase. This result indicates that there may in fact be a limit reached by unstimulated cells in the presence of contractile activation where they can no longer reinforce their cytoskeleton and hence there is no further response to nanomechanical force in the presence of contractile activation. It was previously shown that for both epithelial and fibrosblast cells, the generated traction force reached a saturation level as the microenvironment became stiffer (127, 128). In addition, we also found that cell elasticties were found to be significantly greater that the untreated cells; however, the behaviour diminished compared to the individual drug treatments. These results clearly imply that the loss of MTs during myosin-II activation diminished the contractile response compared to the individual drug treatments; however when compared to the untreated case there was an obvious increase in both traction force and cell elasticity.

6.5 Conclusions

Our results imply that during contractile activation, NIH3T3 fibroblasts have the ability to integrate mechanical cues in the cellular microenvironment in order to modulate mechanotransduction and mechanosensitivity pathways. Clearly, fibroblasts respond optimally to nanomechanical stimulation only on substrates with an elasticity of 51.2 ± 0.419 kPa. It is quite evident here that in the absence of nanomechanical stimulation, fibroblasts respond greatly to contractile activation by generating an increase in traction force and cell elasticity; however during nanomechanical stimulation the response to force (mechanotransduction) is lost due to no further increase in the basal level of contractility achieved during contractile activation either alone or in combination. Interestingly, the loss of MTs was shown to diminish the increase in traction force and cell elasticity in response to myosin-II activation compared to the individual treatments. Therefore, under the conditions in this study, we observe clear changes in traction dynamics and cell mechanics in response to the activation of actomyosin contractility and MT depolymerisation. The results demonstrate that an inhibited mechanotrasnduction response occurs in the presence of nanomechanical stimulation during contractile activation for NIH3T3 mouse fibroblast cells.

6.6 Acknowledgements

This work was supported by a Natural Sciences and Engineering Research Council Discovery Grant [grant number RGPIN/355535-2009 to A.E.P.] and Discovery Accelerator Supplement [grant number RGPAS/380321-2009 to A.E.P.]; the Canada Research Chairs program [grant number 950- 206182 to A.E.P.]; and a Province of Ontario Early Researcher Award [grant number ER09-06-158 to A.E.P.]. Z.A.R. gratefully acknowledges the uOttawa NSERC CREATE program in Quantitative Biomedicine for graduate student support.

Thesis Conclusions

Previous work involving cellular response to applied external forces has revealed its effect on cytoskeletal remodeling, focal adhesion assembly and cell function (34, 36, 217-221). In addition, other studies involving variations in substrate mechanics has shown its effect in directing the fate of undifferentiated cells, cell migration and proliferation (11, 13, 14, 93, 200, 222). Although separately it was shown how substrate mechanics and applied external forces influence cell behavior, their combined effect remained largely unexplored. In this thesis, the combined behavior of these two factors was studied. Moreover, experimental evidence was provided revealing that cells have the ability to sense and respond to distinct physical cues (mechanical cues in the microenvironment or external physical forcs) simultaneously; herein measured via traction forces. In the following pages, I will briefly review the results presented in this thesis and look at potential future research, which can be done on these topics presented.

To recap briefly, traction forces are generated by adherent cells by the contractility of myosin-II motors pulling on the actin fibers. These forces are transmitted to the ECM through a complex structure which is linked to the actin fibers, known as FAs. The forces generated by the cells can be measured by tracking the fiduciary marker beads embedded in the fabricated biocompatible substrates, through TFM. The proper regulation of traction forces may serve to modulate the ablity of cells to sense their physical microenvironment, such that cells with poor regulation of forces may interpret their microenvironments differently than normal cells. Traction forces may be manipulated by external mechanical factors or through intracellular manipulation in order to allow for controlled differentiation of cells and optimize the function of differentiated cells (223). Similarily, traction force regulation may also play a role in deregulating the growth and migration found in malignant cancers. It is becoming quite evident that the mechanical microenvironments of tumors are being recognized as an important aspect in tumor development. Moreover, tumors have been routinely discovered by their increased elasticties relative to normal tissue, however in recent years it is becoming clear that this increase in elasticity can dramatically alter the progression of the disease (8, 9, 224, 225). In particular, it has been shown in vitro that increased ECM elasticities increases tumorigenesis (9). Therefore, it is becoming quite clear that mechanical signals control a wide range of biological events and understanding these behaviors will likely lead to advancements in diagnoses of diseased systems as cancer. Therefore, traction forces represent a critical readout for the understanding and manipulation of biological processes for these purposes.

In chapter four, I examined how external forces and substrates mechanics together influenced the response of mouse myoblasts; whereby traction forces were used as a readout. In order to mimic the microenvironment of muscle tissue, biocompatible gelatin substrates were fabricated with five distinct elastic moduli ranging from ~16-89 kPa. The mechanical properties here, were tuned to mimic the elasticity of resting (~12-39 kPa) to active (~38-97 kPa) mouse muscle tissue (14-19). Here, C2C12 mouse myoblast cells were used as a model system in order to characterize the cellular traction force dynamics in response to both substrate mechanics and controlled mechanical stimulation with the AFM. The response of mouse C2C12 cells to mechanical force is part of the first stages of the myogenic pathway (140, 141). It has been previously shown that for many in-vivo muscle changes after early myogenic progression (35, 140-143), mechanical stimulation during stretch or exercise is responsible for such events. Moreover, for myogenesis to proceed optimally, the physical microenvironment has to mimic that of resting tissue, ~12kPa (14). Interestingly, the results presented in chapter four suggest that myoblasts respond to local nanoscale stimulation only in a microenvironment in which the elasticity is similar to active, working muscle tissue (~64-89kPa). Conversely, the progression of myogenesis, which generally occurs several days after exercise (111, 226) occurs in a softer microenvironment, similar to resting muscle (~16-51kPa) (14). Therefore, the findings presented in chapter four demonstrate that traction forces can be highly regulated and influenced by very different mechanical cues found in the microenvironment. It is advanteagoeus for muscle cells to have increased traction forces at short-time scales because it may lead to increased motility of satellite cells to the areas that are under tissue damage or under active muscle conditions in order to promote myogenesis at later stages (227, 228). This strongly implies that myoblasts can integrate two different mechanical informations; the mechanical properties of its microenvironment (mechanosensitivity) and mechanical stimulation (mechanotrasnduction) in order to regulate its traction force dynamics. Moreover, as future works, it is tempting to test whether my AFM/TFM measurements have any significance in muscle in-vivo in order to establish a link between my obervations and the dynamics taking place during the late myogenic process. Taken together, the results in chapter four evidently reveal that there is indeed a very close relationship between fundamental biological pathways and physical cues found in the mechanical microenvironment of living cells as shown previously (25, 27, 82, 83, 148, 176, 201).

The cytoskeleton is a complex structure composed primarily of actin filaments, MTs and intermediate filaments, and is required for an enormous array of cellular processes (reviewed in appendix A). Although there are numerous studies that have examined either the effect of MT depolymerisation or actomyosin activation on biological processes, very few have investigated the influence of both on the mechanical properties, FA assembly and spreading of NIH3T3 cells. Interestingly, most studies focus on the deactivation of contractility by using specific molecules through biochemical approaches on the cytoskeleton as blebbistatin (which inhibits myosin-II motor protein) or Y27632 (which inhibits the rho dependent kinase pathway); whereas very little studies have investigated the effect of an overly tensed cytoskeleton and its role in cell elasticity as a function of time. In chapter five, I found that overly contractile cells appeared flatter and were stiffer than their untreated counter-parts in agreement with previous work (163, 167, 171, 172). Moreover, they exhibited different morphologies, where they showed an increase in FA size and a concomitant decrease in cell height. A counter-intutive response was observed for the combined treatment. Rather than observing an additive response, cells appeared softer, indicative of cell rounding, where a loss in FA was observed with a concomitant increase in cell height. This may be attributed to a hypercontractile phenotype induced by the collective effects of the two drugs. One can consider tracking the cell area with time to observe this response. Another experiment would be to measure the cell elasticity for different concentrations of nocodazole and calyculin A separately in order to probe this effect. The data presented in chapter five clearly reveals that upon the loss of MTs, the ability of fibroblast cells to maintain increased contractility upon activation of myosin-II was eventually disabled. Therefore, MTs are responsibe for mediating the mechanical properties of cells induced with an increase in contractlity. In chapter six, I extend this study by characterizing the traction forces of fibroblasts during contractile activation and mechanical stimulation.

Chapter six presents' data which suggests that cells induced with the drug agents that increased contractlity will generate greater traction forces; however in the presence of a force, those cells lose their mechanotransduction responses. Unlike chapter four, a reduction in cell elasticity was not observed when MTs were disrupted even though myosin-II was enhanced. This clearly implies that fibroblasts are highly mechanosensitive cells. In chapter six, cells were grown on an optimal flexible substrate that behaved as linear elastic solid as revealed by the rheological data (appendix E), unlike in chapter four, where cells were grown a rigid substrate; which may likely contribute to the observed response observed during the sequential stimulation of contractility. Several future experiments can arise from the interesting results found in chapter five. Since cells did not respond to to an external physical stimulation (constant 10nN) it could be that an overly tensed cell would require a larger force in order to trigger the onset of traction forces. Maybe increasing the applied force, fibroblasts will respond to an external force. Another, interesting question to address is to find if the response to external force depends on incubation time. Since I have shown in chapter four, that cell elasticity is time-independent then will this also be true for traction forces. The data presented here provides greater insight on the complex interplay between the cytoskeletal and FA remodelling that control and mediate the traction dynamics and mechanical properties of the cells in relation to its surrounding mechanical microenvironment and physical forces.Understanding this complex interplay will have important implications in diseased systems, with hypercontractile phenotypic cells (229, 230).

It is becoming quite clear that there indeed exists a very close relationship and link between the fundamental biological pathways and the many physical cues found in the mechanical microenvironment of living mammalian cells (38-44). Moreover, cells are exposed to a number of physical signals, whether at the cellular or subcellular levels, where they are eventually combined to regulate or modulate cell-type specific mechanotransduction and mechanosensitivity pathways. Employing traction force as indicator of mechanotransduction in myoblasts and fibroblasts, we have both examined and provided experimental evidence that there is definitely an existing interplay between substrate elasticity, mechanical stimulation, traction forces, cell mechanics, and FA remodelling. Therefore, understanding how cells can integrate and regulate physical cues in the microenvironment, nanomechanical forces and cell mechanics has important implications for our fundamental understanding of these processes as well as potentially aiding in novel diagnostic approaches (105, 156-158, 185).

References

1. Heilbrunn, L., editor. 1956. The Dynamics of Living Protoplasm. Academic Press, New York.
2. Levental, I., P. C. Georges, and P. A. Janmey. 2007. Soft biological materials and their impact on cell function. Soft Matter 3:299-306.
3. Kononov, S., K. Brewer, H. Sakai, F. S. A. Cavalcante, C. R. Sabayanagam, E. P. Ingenito, and B. Suki. 2001. Roles of mechanical forces and collagen failure in the development of elastase-induced emphysema. Am J Resp Crit Care 164:1920-1926.
4. Cavalcante, F. S. A., S. Ito, K. Brewer, H. Sakai, A. M. Alencar, M. P. Almeida, J. S. Andrade, A. Majumdar, E. P. Ingenito, and B. Suki. 2005. Mechanical interactions between collagen and proteoglycans: implications for the stability of lung tissue. J Appl Physiol 98:672-679.
5. Mijailovich, S. M., D. Stamenovic, R. Brown, D. E. Leith, and J. J. Fredberg. 1994. Dynamic Moduli of Rabbit Lung-Tissue and Pigeon Ligamentum Propatagiale Undergoing Uniaxial Cyclic Loading. J Appl Physiol 76:773-782.
6. Yuan, H. C., S. Kononov, F. S. A. Cavalcante, K. R. Lutchen, E. P. Ingenito, and B. Suki. 2000. Effects of collagenase and elastase on the mechanical properties of lung tissue strips. J Appl Physiol 89:3-14.
7. Levental, K. R., H. M. Yu, L. Kass, J. N. Lakins, M. Egeblad, J. T. Erler, S. F. T. Fong, K. Csiszar, A. Giaccia, W. Weninger, M. Yamauchi, D. L. Gasser, and V. M. Weaver. 2009. Matrix Crosslinking Forces Tumor Progression by Enhancing Integrin Signaling. Cell 139:891-906.
8. Huang, S., and D. E. Ingber. 2005. Cell tension, matrix mechanics, and cancer development. Cancer Cell 8:175-176.
9. Paszek, M. J., N. Zahir, K. R. Johnson, J. N. Lakins, G. I. Rozenberg, A. Gefen, C. A. Reinhart-King, S. S. Margulies, M. Dembo, D. Boettiger, D. A. Hammer, and V. M. Weaver. 2005. Tensional homeostasis and the malignant phenotype. Cancer Cell 8:241-254.

10. Tilghman, R. W., C. R. Cowan, J. D. Mih, Y. Koryakina, D. Gioeli, J. K. Slack-Davis, B. R. Blackman, D. J. Tschumperlin, and J. T. Parsons. 2010. Matrix Rigidity Regulates Cancer Cell Growth and Cellular Phenotype. Plos One 5.

11. Engler, A. J., S. Sen, H. L. Sweeney, and D. E. Discher. 2006. Matrix elasticity directs stem cell lineage specification. Cell 126:677-689.

12. Dalby, M. J., N. Gadegaard, R. Tare, A. Andar, M. O. Riehle, P. Herzyk, C. D. W. Wilkinson, and R. O. C. Oreffo. 2007. The control of human mesenchymal cell differentiation using nanoscale symmetry and disorder. Nat Mater 6:997-1003.

13. Martino, S., F. D'Angelo, I. Armentano, R. Tiribuzi, M. Pennacchi, M. Dottori, S. Mattioli, A. Caraffa, G. G. Cerulli, J. M. Kenny, and A. Orlacchio. 2009. Hydrogenated Amorphous Carbon Nanopatterned Film Designs Drive Human Bone Marrow Mesenchymal Stem Cell Cytoskeleton Architecture. Tissue Eng Pt A 15:3139-3149.

14. Engler, A. J., M. A. Griffin, S. Sen, C. G. Bonnetnann, H. L. Sweeney, and D. E. Discher. 2004. Myotubes differentiate optimally on substrates with tissue-like stiffness: pathological implications for soft or stiff microenvironments. J Cell Biol 166:877-887.

15. Collinsworth, A. M., S. Zhang, W. E. Kraus, and G. A. Truskey. 2002. Apparent elastic modulus and hysteresis of skeletal muscle cells throughout differentiation. Am J Physiol-Cell Ph 283:C1219-C1227.

16. Mathur, A. B., A. M. Collinsworth, W. M. Reichert, W. E. Kraus, and G. A. Truskey. 2001. Endothelial, cardiac muscle and skeletal muscle exhibit different viscous and elastic properties as determined by atomic force microscopy. J Biomech 34:1545-1553.

17. Nyland, L. R., and D. W. Maughan. 2000. Morphology and transverse stiffness of Drosophila myofibrils measured by atomic force microscopy. Biophys J 78:1490-1497.

18. Ogneva, I. V. 2010. Transversal stiffness of fibers and desmin content in leg muscles of rats under gravitational unloading of various durations. J Appl Physiol 109:1702-1709.

19. Ogneva, I. V., D. V. Lebedev, and B. S. Shenkman. 2010. Transversal Stiffness and Young's Modulus of Single Fibers from Rat Soleus Muscle Probed by Atomic Force Microscopy. Biophys J 98:418-424.

20. Akimoto, T., T. Uchida, S. Miyaki, H. Akaogi, T. Tateishi, and T. Fukubayashi. 2004. Effect of mechanical stretch on TGF-beta 1 expression of C2C12 myogenic cells. Mat Sci Eng C-Bio S 24:387-389.

21. Kook, S. H., H. J. Lee, W. T. Chung, I. H. Hwang, S. A. Lee, B. S. Kim, and J. C. Lee. 2008. Cyclic mechanical stretch stimulates the proliferation of C2C12 myoblasts and inhibits their differentiation via prolonged activation of p38 MAPK. Molecules and Cells 25:479-486.

22. Otis, J. S., T. J. Burkholder, and G. K. Pavlath. 2005. Stretch-induced myoblast proliferation is dependent on the COX2 pathway. Experimental Cell Research 310:417-425.

23. Zhan, M., B. W. Jin, S. E. Chen, J. M. Reecy, and Y. P. Li. 2007. TACE release of TNF-alpha mediates mechanotransduction-induced activation of p38 MAPK and myogenesis. J Cell Sci 120:692-701.

24. Parker, M. H., P. Seale, and M. A. Rudnicki. 2003. Looking back to the embryo: Defining transcriptional networks in adult myogenesis. Nature Reviews Genetics 4:497-507.

25. Buxboim, A., I. L. Ivanovska, and D. E. Discher. 2010. Matrix elasticity, cytoskeletal forces and physics of the nucleus: how deeply do cells 'feel' outside and in? J Cell Sci 123:297-308.

26. Engler, A. J., L. Richert, J. Y. Wong, C. Picart, and D. E. Discher. 2004. Surface probe measurements of the elasticity of sectioned tissue, thin gels and polyelectrolyte multilayer films: Correlations between substrate stiffness and cell adhesion. Surf Sci 570:142-154.

27. Jaalouk, D. E., and J. Lammerding. 2009. Mechanotransduction gone awry. Nat Rev Mol Cell Bio 10:63-73.

28. von Wichert, G., D. Krndija, H. Schmid, G. Wichert, G. Haerter, G. Adler, T. Seufferlein, and M. P. Sheetz. 2008. Focal adhesion kinase mediates defects in the

force-dependent reinforcement of initial integrin-cytoskeleton linkages in metastatic colon cancer cell lines. Eur J Cell Biol 87:1-16.

29. Discher, D. E., P. Janmey, and Y. L. Wang. 2005. Tissue cells feel and respond to the stiffness of their substrate. Science 310:1139-1143.

30. Engler, A. J., C. Carag-Krieger, C. P. Johnson, M. Raab, H. Y. Tang, D. W. Speicher, J. W. Sanger, J. M. Sanger, and D. E. Discher. 2008. Embryonic cardiomyocytes beat best on a matrix with heart-like elasticity: scar-like rigidity inhibits beating. J Cell Sci 121:3794-3802.

31. Chen, C., R. Krishnan, E. H. Zhou, A. Ramachandran, D. Tambe, K. Rajendran, R. M. Adam, L. H. Deng, and J. J. Fredberg. 2010. Fluidization and Resolidification of the Human Bladder Smooth Muscle Cell in Response to Transient Stretch. Plos One 5.

32. Krishnan, R., C. Y. Park, Y. C. Lin, J. Mead, R. T. Jaspers, X. Trepat, G. Lenormand, D. Tambe, A. V. Smolensky, A. H. Knoll, J. P. Butler, and J. J. Fredberg. 2009. Reinforcement versus Fluidization in Cytoskeletal Mechanoresponsiveness. Plos One 4.

33. Lopez, J. I., J. K. Mouw, and V. M. Weaver. 2008. Biomechanical regulation of cell orientation and fate. Oncogene 27:6981-6993.

34. Sniadecki, N. J., A. Anguelouch, M. T. Yang, C. M. Lamb, Z. Liu, S. B. Kirschner, Y. Liu, D. H. Reich, and C. S. Chen. 2007. Magnetic microposts as an approach to apply forces to living cells. P Natl Acad Sci USA 104:14553-14558.

35. Vandenburgh, H. H., S. Hatfaludy, P. Karlisch, and J. Shansky. 1989. Skeletal-Muscle Growth Is Stimulated by Intermittent Stretch-Relaxation in Tissue-Culture. American Journal of Physiology 256:C674-C682.

36. Yamamoto, K., T. Sokabe, T. Watabe, K. Miyazono, J. K. Yamashita, S. Obi, N. Ohura, A. Matsushita, A. Kamiya, and J. Ando. 2005. Fluid shear stress induces differentiation of Flk-1-positive embryonic stem cells into vascular endothelial cells in vitro. Am J Physiol-Heart C 288:H1915-H1924.

37. Binnig, G., C. F. Quate, and C. Gerber. 1986. Atomic Force Microscope. Phys Rev Lett 56:930-933.

38. Binnig, G., and H. Rohrer. 1982. Scanning Tunneling Microscopy. Helv Phys Acta 55:726-735.

39. Binnig, G., H. Rohrer, C. Gerber, and E. Weibel. 1982. Tunneling through a Controllable Vacuum Gap. Appl Phys Lett 40:178-180.

40. Hansma, P. K., V. B. Elings, O. Marti, and C. E. Bracker. 1988. Scanning Tunneling Microscopy and Atomic Force Microscopy - Application to Biology and Technology. Science 242:209-216.

41. Drake, B., C. B. Prater, A. L. Weisenhorn, S. A. C. Gould, T. R. Albrecht, C. F. Quate, D. S. Cannell, H. G. Hansma, and P. K. Hansma. 1989. Imaging Crystals, Polymers, and Processes in Water with the Atomic Force Microscope. Science 243:1586-1589.

42. Barris, B., U. Knipping, S. M. Lindsay, L. Nagahara, and T. Thundat. 1988. Images of DNA Fragments in an Aqueous Environment by Scanning Tunneling Microscopy. Biopolymers 27:1691-1696.

43. Smith, D. P. E., A. Bryant, C. F. Quate, J. P. Rabe, C. Gerber, and J. D. Swalen. 1987. Images of a Lipid Bilayer at Molecular Resolution by Scanning Tunneling Microscopy. P Natl Acad Sci USA 84:969-972.

44. Butt, H. J., B. Cappella, and M. Kappl. 2005. Force measurements with the atomic force microscope: Technique, interpretation and applications. Surf Sci Rep 59:1-152.

45. Radmacher, M., R. W. Tillmann, M. Fritz, and H. E. Gaub. 1992. From Molecules to Cells - Imaging Soft Samples with the Atomic Force Microscope. Science 257:1900-1905.

46. Zougagh, M., and A. Rios. 2009. Micro-electromechanical sensors in the analytical field. Analyst 134:1274-1290.

47. Mäkynen, A., T. Ruotsalainen, T. Rahkonen, and J. Kostamovaara. 2003. CMOS-compatible position-sensitive devices (PSDs) based on photodetector arrays. Sensors and Actuators A 105:261-270.

48. Carl, P., and H. Schillers. 2008. Elasticity measurement of living cells with an atomic force microscope: data acquisition and processing. Pflug Arch Eur J Phy 457:551-559.

49. Meyer, G., and N. M. Amer. 1990. Optical-Beam-Deflection Atomic Force Microscopy - the Nacl (001) Surface. Appl Phys Lett 56:2100-2101.
50. Taylor, G. W., J. J. Gagnepain, T. R. Meeker, T. Nakamura, and L. A. Shuvalov. 1985. Piezoelectricity. 4 ed. Gordon and Breach Science Publishers, New York.
51. Barr, M. 2002. Closed Loop Control. Embedded Systems Programming:55-56.
52. Levy, R., and M. Maaloum. 2002. Measuring the spring constant of atomic force microscope cantilevers: Thermal fluctuations and other methods. Nanotechnology 13:33-37.
53. Hutter, J. L., and J. Bechhoefer. 1993. Calibration of Atomic-Force Microscope Tips. Review of Scientific Instruments 64:1868-1873.
54. Sader, J. E., J. W. M. Chon, and P. Mulvaney. 1999. Calibration of rectangular atomic force microscope cantilevers. Review of Scientific Instruments 70:3967-3969.
55. Cleveland, J. P., S. Manne, D. Bocek, and P. K. Hansma. 1993. A Nondestructive Method for Determining the Spring Constant of Cantilevers for Scanning Force Microscopy. Review of Scientific Instruments 64:403-405.
56. Levy, R., and M. Maaloum. 2002. Measuring the spring constant of atomic force microscope cantilevers: thermal fluctuations and other methods. Nanotechnology 13:33-37.
57. Giessibl, F. J. 2003. Advances in atomic force microscopy. Rev Mod Phys 75:949-983.
58. Hansma, P. K., J. P. Cleveland, M. Radmacher, D. A. Walter, P. E. Hillner, M. Bexanilla, M. Fritz, D. Vie, H. G. Hansma, C. B. Prater, J. Massie, and L. Fukunaga. 1994. Tapping mode atomic-force microscopy in liquids. Applied physics Letters 64:1738-1740.
59. Radmacher, M., M. Fritz, C. M. Kacher, J. P. Cleveland, and P. K. Hansma. 1996. Measuring the viscoelastic properties of human platelets with the atomic force microscope. Biophys J 70:556-567.
60. Radmacher, M., M. Fritz, and P. K. Hansma. 1995. Imaging Soft Samples with the Atomic-Force Microscope - Gelatin in Water and Propanol. Biophys J 69:264-270.
61. Hertz, H. 1882. Uber die Beriihrung fester elastischer Korper. J. Reine Angew. Mathematik 92:156-171.

62. Sneddon, I. N. 1965. The Relation between Load and Penetration in the Axisymmetric Boussinesq Problem for a Punch of Arbitrary Profile. Int. J. Engng Sci. 3:47-57.

63. Kojima, H., A. Ishijima, and T. Yanagida. 1994. Direct Measurement of Stiffness of Single Actin-Filaments with and without Tropomyosin by in-Vitro Nanomanipulation. P Natl Acad Sci USA 91:12962-12966.

64. Solon, J., I. Levental, K. Sengupta, P. C. Georges, and P. A. Janmey. 2007. Fibroblast adaptation and stiffness matching to soft elastic substrates. Biophys J 93:4453-4461.

65. Harris, A. K., P. Wild, and D. Stopak. 1980. Silicone-Rubber Substrata - New Wrinkle in the Study of Cell Locomotion. Science 208:177-179.

66. Lee, J., M. Leonard, T. Oliver, A. Ishihara, and K. Jacobson. 1994. Traction forces generated by locomoting keratocytes. J Cell Biol. 127:1957-1964.

67. Dembo, M., and Y. L. Wang. 1999. Stresses at the cell-to-substrate interface during locomotion of fibroblasts. Biophys J 76:2307-2316.

68. Pelham, R. J., and Y. L. Wang. 1997. Cell locomotion and focal adhesions are regulated by substrate flexibility. P Natl Acad Sci USA 94:13661-13665.

69. Nelson, C., S. Raghavan, J. Tan, and C. Chen. 2003. Degradtaion of micropatterned surfaces by cell-dependent and -independent processes. Langmuir 19:1493-1499.

70. Doyle, A., W. Marganski, and J. Lee. 2004. Calcium transients induce spatially coordinated increases in traction force during the movement of fish keratocytes. J Cell Sci 117:2203-2214.

71. Tan, J. L., J. Tien, D. M. Pirone, D. S. Gray, K. Bhadriraju, and C. S. Chen. 2003. Cells lying on a bed of microneedles: an appraoch to isolate mechanical force. Proc Natl Acas Sci USA 100:1484-1489.

72. Tan, J. L., J. Tien, D. M. Pirone, D. S. Gray, K. Bhadriraju, and C. S. Chen. 2003. Cells lying on a bed of microneedles: An approach to isolate mechanical force. P Natl Acad Sci USA 100:1484-1489.

73. Beningo, K. A., M. Dembo, I. Kaverina, J. V. Small, and Y. L. Wang. 2001. Nascent focal adhesions are responsible for the generation of strong propulsive forces in migrating fibroblasts. J Cell Biol 153:881-887.

74. Wang, J. H. C., and J. S. Lin. 2007. Cell traction force and measurement methods. Biomech Model Mechan 6:361-371.

75. Marganski, W. A., M. Dembo, and Y. L. Wang. 2003. Measurements of cell-generated deformations on flexible substrata using correlation-based optical flow. Method Enzymol 361:197-211.

76. Landau, L. D. L., E.M., editor. 1970. Course of Theoretical Physics: Theory of Elasticity. Pergamon Press, Oxford.

77. Lo, C. M., H. B. Wang, M. Dembo, and Y. L. Wang. 2000. Cell movement is guided by the rigidity of the substrate. Biophys J 79:144-152.

78. Munevar, S., Y. L. Wang, and M. Dembo. 2001. Traction force microscopy of migrating normal and H-ras transformed 3T3 fibroblasts. Biophys J 80:1744-1757.

79. Marganski, W. A., M. Dembo, and W. Y. L. 2003. Measurements of cell-generated deformations on flexible substrata using correlation-based optical flow. Methods Enzymol. 361:197-211.

80. Butler, J. P., I. M. Tolic-Norrelykke, B. Fabry, and J. J. Fredberg. 2002. Traction fields, moments, and strain energy that cells exert on their surroundings. Am J Physiol-Cell Ph 282:C595-C605.

81. Janmey, P. A., and R. T. Miller. 2011. Mechanisms of mechanical signaling in development and disease. J Cell Sci 124:9-18.

82. Discher, D. E., D. J. Mooney, and P. W. Zandstra. 2009. Growth Factors, Matrices, and Forces Combine and Control Stem Cells. Science 324:1673-1677.

83. Holle, A. W., and A. J. Engler. 2011. More than a feeling: discovering, understanding, and influencing mechanosensing pathways. Curr Opin Biotech 22:648-654.

84. Vogel, V., and M. Sheetz. 2006. Local force and geometry sensing regulate cell functions. Nat Rev Mol Cell Biol 7:265-275.

85. Schwarz, U. S., and M. L. Gardel. 2012. United we stand: integrating the actin cytoskeleton and cell-matrix adhesions in cellular mechanotransduction. J Cell Sci 125:3051-3060.

86. Sniadecki, N. J., A. Anguelouch, M. T. Yang, C. M. Lamb, Z. Liu, S. B. Kirschner, Y. Liu, D. H. Reich, and C. S. Chen. 2007. Magnetic microposts as an approach to apply forces to living cells. Proc Natl Acad Sci U S A 104:14553-14558.

87. Arora, P. D., N. Narani, and C. A. G. McCulloch. 1999. The compliance of collagen gels regulates transforming growth factor-beta induction of alpha-smooth muscle actin in fibroblasts. American Journal of Pathology 154:871-882.

88. Nagayama, K., A. Adachi, and T. Matsumoto. 2011. Heterogeneous response of traction force at focal adhesions of vascular smooth muscle cells subjected to macroscopic stretch on a micropillar substrate. J Biomech 44:2699-2705.

89. Krishnan, R., C. Y. Park, Y. C. Lin, J. Mead, R. T. Jaspers, X. Trepat, G. Lenormand, D. Tambe, A. V. Smolensky, A. H. Knoll, J. P. Butler, and J. J. Fredberg. 2009. Reinforcement versus fluidization in cytoskeletal mechanoresponsiveness. PloS One 4:e5486.

90. Chen, C., R. Krishnan, E. Zhou, A. Ramachandran, D. Tambe, K. Rajendran, R. M. Adam, L. Deng, and J. J. Fredberg. 2010. Fluidization and resolidification of the human bladder smooth muscle cell in response to transient stretch. PloS One 5:e12035.

91. Na, S., O. Collin, F. Chowdhury, B. Tay, M. Ouyang, Y. Wang, and N. Wang. 2008. Rapid signal transduction in living cells is a unique feature of mechanotransduction. Proc Natl Acad Sci U S A 105:6626-6631.

92. Zhao, X. H., C. Laschinger, P. Arora, K. Szaszi, A. Kapus, and C. A. McCulloch. 2007. Force activates smooth muscle alpha-actin promoter activity through the Rho signaling pathway. J Cell Sci 120:1801-1809.

93. Chowdhury, F., S. Na, D. Li, Y. C. Poh, T. S. Tanaka, F. Wang, and N. Wang. 2010. Material properties of the cell dictate stress-induced spreading and differentiation in embryonic stem cells. Nat Mater 9:82-88.

94. Pines, M., R. Das, S. J. Ellis, A. Morin, S. Czerniecki, L. Yuan, M. Klose, D. Coombs, and G. Tanentzapf. 2012. Mechanical force regulates integrin turnover in Drosophila in vivo. Nat Cell Biol 14:935-943.

95. Ng, C. P., B. Hinz, and M. A. Swartz. 2005. Interstitial fluid flow induces myofibroblast differentiation and collagen alignment in vitro. J Cell Sci 118:4731-4739.

96. Lin, Y. C., C. M. Kramer, C. S. Chen, and D. H. Reich. 2012. Probing cellular traction forces with magnetic nanowires and microfabricated force sensor arrays. Nanotechnology 23.

97. Friedrichs, J., J. Helenius, and D. J. Muller. 2010. Quantifying cellular adhesion to extracellular matrix components by single-cell force spectroscopy. Nat Protoc 5:1353-1361.

98. Muller, D. J., and Y. F. Dufrene. 2011. Atomic force microscopy: a nanoscopic window on the cell surface. Trends Cell Biol 21:461-469.

99. Stewart, M. P., Y. Toyoda, A. A. Hyman, and D. J. Muller. 2012. Tracking mechanics and volume of globular cells with atomic force microscopy using a constant-height clamp. Nat Protoc 7:143-154.

100. Stewart, M. P., J. Helenius, Y. Toyoda, S. P. Ramanathan, D. J. Muller, and A. A. Hyman. 2011. Hydrostatic pressure and the actomyosin cortex drive mitotic cell rounding. Nature 469:226-230.

101. Pelling, A. E., F. S. Veraitch, C. P. Chu, C. Mason, and M. A. Horton. 2009. Mechanical dynamics of single cells during early apoptosis. Cell Motil Cytoskeleton 66:409-422.

102. Kunda, P., A. E. Pelling, T. Liu, and B. Baum. 2008. Moesin controls cortical rigidity, cell rounding, and spindle morphogenesis during mitosis. Curr Biol 18:91-101.

103. Iyer, S., R. M. Gaikwad, V. Subba-Rao, C. D. Woodworth, and I. Sokolov. 2009. Atomic force microscopy detects differences in the surface brush of normal and cancerous cells. Nat Nanotechnol 4:389-393.

104. Hogan, C., S. Dupre-Crochet, M. Norman, M. Kajita, C. Zimmermann, A. E. Pelling, E. Piddini, L. A. Baena-Lopez, J. P. Vincent, Y. Itoh, H. Hosoya, F. Pichaud, and Y. Fujita. 2009. Characterization of the interface between normal and transformed epithelial cells. Nat Cell Biol 11:460-U234.

105. Cross, S. E., Y. S. Jin, J. Rao, and J. K. Gimzewski. 2007. Nanomechanical analysis of cells from cancer patients. Nat Nanotechnol 2:780-783.

106. Young, J. L., and A. J. Engler. 2011. Hydrogels with time-dependent material properties enhance cardiomyocyte differentiation in vitro. Biomaterials 32:1002-1009.

107. Guvendiren, M., and J. A. Burdick. 2012. Stiffening hydrogels to probe short- and long-term cellular responses to dynamic mechanics. Nat Commun 3:792.

108. Modulevsky, D. J., D. Tremblay, C. Gullekson, N. V. Bukoresthliev, and A. E. Pelling. 2012. The Physical Interaction of Myoblasts with the Microenvironment during Remodeling of the Cytoarchitecture. PloS One 7:e45329.

109. Li, B., M. Lin, Y. Tang, B. Wang, and J. H. C. Wang. 2008. A novel functional assessment of the differentiation of micropatterned muscle cells. J Biomech 41:3349-3353.

110. Griffin, M. A., S. Sen, H. L. Sweeney, and D. E. Discher. 2004. Adhesion-contractile balance in myocyte differentiation. J Cell Sci 117:5855-5863.

111. Nag, A. C., and J. D. Foster. 1981. Myogenesis in Adult Mammalian Skeletal-Muscle Invitro. Journal of Anatomy 132:1-18.

112. Yang, Y., A. Creer, B. Jemiolo, and S. Trappe. 2005. Time course of myogenic and metabolic gene expression in response to acute exercise in human skeletal muscle. J Appl Physiol 98:1745-1752.

113. Pelling, A. E., F. S. Veraitch, C. P. K. Chu, C. Mason, and M. A. Horton. 2009. Mechanical Dynamics of Single Cells During Early Apoptosis. Cell Motil Cytoskel 66:409-422.

114. Guolla, L., M. Bertrand, K. Haase, and A. E. Pelling. 2012. Force transduction and strain dynamics in actin stress fibres in response to nanonewton forces. J Cell Sci 125:603-613.

115. Dembo, M., T. Oliver, A. Ishihara, and K. Jacobson. 1996. Imaging the traction stresses exerted by locomoting cells with the elastic substratum method. Biophys J 70:2008-2022.

116. Lee, J. 2007. The use of gelatin substrates for traction force microscopy in rapidly moving cells. Cell Mechanics 83:297-312.

117. Guvendiren, M., and J. A. Burdick. 2012. Stiffening hydrogels to probe short- and long-term cellular responses to dynamic mechanics. Nat Commun 3:792.

118. Lee, J., M. Leonard, T. Oliver, A. Ishihara, and K. Jacobson. 1994. Traction Forces Generated by Locomoting Keratocytes. J Cell Biol 127:1957-1964.

119. Lombardi, M. L., D. A. Knecht, M. Dembo, and J. Lee. 2007. Traction force microscopy in Dictyostelium reveals distinct roles for myosin II motor and actin-crosslinking activity in polarized cell movement. J Cell Sci 120:1624-1634.

120. Hazeltine, L. B., C. S. Simmons, M. R. Salick, X. Lian, M. G. Badur, W. Han, S. M. Delgado, T. Wakatsuki, W. C. Crone, B. L. Pruitt, and S. P. Palecek. 2012. Effects of substrate mechanics on contractility of cardiomyocytes generated from human pluripotent stem cells. Int J Cell Biol. doi:10.1155/2012/508294.

121. Rape, A., W. H. Guo, and Y. L. Wang. 2011. Microtubule depolymerization induces traction force increase through two distinct pathways. J Cell Sci 124:4233-4240.

122. Curtze, S., M. Dembo, M. Miron, and D. B. Jones. 2004. Dynamic changes in traction forces with DC electric field in osteoblast-like cells. J Cell Sci 117:2721-2729.

123. Beningo, K. A., K. Hamao, M. Dembo, Y. L. Wang, and H. Hosoya. 2006. Traction forces of fibroblasts are regulated by the Rho-dependent kinase but not by the myosin light chain kinase. Archives of Biochemistry and Biophysics 456:224-231.

124. Gardel, M. L., B. Sabass, L. Ji, G. Danuser, U. S. Schwarz, and C. M. Waterman. 2008. Traction stress in focal adhesions correlates biphasically with actin retrograde flow speed. J Cell Biol 183:999-1005.

125. Formigli, L., E. Meacci, C. Sassoli, F. Chellini, R. Giannini, F. Quercioli, B. Tiribilli, R. Squecco, P. Bruni, F. Francini, and S. Zecchi-Orlandini. 2005. Sphingosine 1-phosphate induces cytoskeletal reorganization in C2C12 myoblasts: physiological relevance for stress fibres in the modulation of ion current through stretch-activated channels. J Cell Sci 118:1161-1171.

126. Haase, K., and A. E. Pelling. 2013. Resiliency of the plasma membrane and actin cortex to large-scale deformation. Cytoskeleton.

127. Ghibaudo, M., A. Saez, L. Trichet, A. Xayaphoummine, J. Browaeys, P. Silberzan, A. Buguin, and B. Ladoux. 2008. Traction forces and rigidity sensing regulate cell functions. Soft Matter 4:1836-1843.

128. Saez, A., A. Buguin, P. Silberzan, and B. Ladoux. 2005. Is the mechanical activity of epithelial cells controlled by deformations or forces? Biophys J 89:L52-L54.

129. Shi, X. L., L. Qin, X. J. Zhang, K. M. He, C. Y. Xiong, J. Fang, X. H. Fang, and Y. Y. Zhang. 2011. Elasticity of cardiac cells on the polymer substrates with different stiffness: an atomic force microscopy study. Phys Chem Chem Phys 13:7540-7545.

130. Byfield, F. J., R. K. Reen, T. P. Shentu, I. Levitan, and K. J. Gooch. 2009. Endothelial actin and cell stiffness is modulated by substrate stiffness in 2D and 3D. J Biomech 42:1114-1119.

131. Ghosh, K., Z. Pan, E. Guan, S. R. Ge, Y. J. Liu, T. Nakamura, X. D. Ren, M. Rafailovich, and R. A. F. Clark. 2007. Cell adaptation to a physiologically relevant ECM mimic with different viscoelastic properties. Biomaterials 28:671-679.

132. Oakes, P. W., Y. Beckham, J. Stricker, and M. L. Gardel. 2012. Tension is required but not sufficient for focal adhesion maturation without a stress fiber template. J Cell Biol 196:363-374.

133. de Rooij, J., A. Kerstens, G. Danuser, M. A. Schwartz, and C. M. Waterman-Storer. 2005. Integrin-dependent actomyosin contraction regulates epithelial cell scattering. J Cell Biol 171:153-164.

134. Guo, W. H., M. T. Frey, N. A. Burnham, and Y. L. Wang. 2006. Substrate rigidity regulates the formation and maintenance of tissues. Biophys J 90:2213-2220.

135. Fu, J., Y. K. Wang, M. T. Yang, R. A. Desai, X. Yu, Z. Liu, and C. S. Chen. 2010. Mechanical regulation of cell function with geometrically modulated elastomeric substrates. Nature methods 7:733-736.

136. Han, S. J., K. S. Bielawski, L. H. Ting, M. L. Rodriguez, and N. J. Sniadecki. 2012. Decoupling Substrate Stiffness, Spread Area, and Micropost Density: A Close Spatial Relationship between Traction Forces and Focal Adhesions. Biophys J 103:640-648.

137. Grashoff, C., B. D. Hoffman, M. D. Brenner, R. Zhou, M. Parsons, M. T. Yang, M. A. McLean, S. G. Sligar, C. S. Chen, T. Ha, and M. A. Schwartz. 2010. Measuring

mechanical tension across vinculin reveals regulation of focal adhesion dynamics. Nature 466:263-266.

138. Hoffman, L. M., C. C. Jensen, A. Chaturvedi, M. Yoshigi, and M. C. Beckerle. 2012. Stretch-induced actin remodeling requires targeting of zyxin to stress fibers and recruitment of actin regulators. Molecular biology of the cell 23:1846-1859.

139. Gallegos, L., M. R. Ng, and J. S. Brugge. 2011. The myosin-II-responsive focal adhesion proteome: a tour de force? Nat Cell Biol 13:344-346.

140. Goldspink, D. F., V. M. Cox, S. K. Smith, L. A. Eaves, N. J. Osbaldeston, D. M. Lee, and D. Mantle. 1995. Muscle Growth in Response to Mechanical Stimuli. American Journal of Physiology-Endocrinology and Metabolism 31:E288-E297.

141. Goldspink, D. F., J. Easton, S. K. Winterburn, P. E. Williams, and G. E. Goldspink. 1991. The Role of Passive Stretch and Repetitive Electrical-Stimulation in Preventing Skeletal-Muscle Atrophy While Reprogramming Gene-Expression to Improve Fatigue Resistance. Journal of Cardiac Surgery 6:218-224.

142. Collinsworth, A. M., C. E. Torgan, S. N. Nagda, R. J. Rajalingam, W. E. Kraus, and G. A. Truskey. 2000. Orientation and length of mammalian skeletal myocytes in response to a unidirectional stretch. Cell Tissue Res 302:243-251.

143. Vandenburgh, H. H., S. Swasdison, and P. Karlisch. 1991. Computer-Aided Mechanogenesis of Skeletal-Muscle Organs from Single Cells-Invitro. Faseb J 5:2860-2867.

144. Zatti, S., A. Zoso, E. Serena, C. Luni, E. Cimetta, and N. Elvassore. 2012. Micropatterning topology on soft substrates affects myoblast proliferation and differentiation. Langmuir 28:2718-2726.

145. Bukoreshtliev, N. V., K. Haase, and A. E. Pelling. 2013. Mechanical cues in cellular signalling and communication. Cell Tissue Res 352:77-94.

146. Fletcher, D. A., and D. Mullins. 2010. Cell mechanics and the cytoskeleton. Nature 463:485-492.

147. Herrmann, H., H. Bar, L. Kreplak, S. V. Strelkov, and U. Aebi. 2007. Intermediate filaments: from cell architecture to nanomechanics. Nat Rev Mol Cell Bio 8:562-573.

148. Janmey, P. A., and R. T. Miller. 2011. Mechanisms of mechanical signaling in development and disease. J Cell Sci 124:9-18.

149. Rape, A. D., W. H. Guo, and Y. L. Wang. 2011. The regulation of traction force in relation to cell shape and focal adhesions. Biomaterials 32:2043-2051.

150. Dufrene, Y. F., and A. Pelling, E.. 2013. Force nanoscopy of cell mechanics and cell adhesion. Nanoscale 5:4094-4104.

151. Lam, W. A., M. J. Rosenbluth, and D. A. Fletcher. 2007. Chemotherapy exposure increases leukemia cell stiffness. Blood 109:3505-3508.

152. Matzke, R., K. Jacobson, and M. Radmacher. 2001. Direct, high-resolution measurement of furrow stiffening during division of adherent cells. Nat Cell Biol 3:607-610.

153. Kunda, P., A. E. Pelling, T. Liu, and B. Baum. 2008. Moesin controls cortical rigidity, cell rounding, and spindle morphogenesis during mitosis. Curr Biol 18:91-101.

154. Costa, K. D. 2003. Single-cell elastography: Probing for disease with the atomic force microscope. Dis Markers 19:139-154.

155. Muller, D. J., and Y. F. Dufrene. 2008. Atomic force microscopy as a multifunctional molecular toolbox in nanobiotechnology. Nat Nanotechnol 3:261-269.

156. Suresh, S. 2007. Biomechanics and biophysics of cancer cells. Acta Biomaterialia 3:413-438.

157. Cross, S. E., Y. S. Jin, J. Tondre, R. Wong, J. Rao, and J. K. Gimzewski. 2008. AFM-based analysis of human metastatic cancer cells. Nanotechnology 19.

158. Stolz, M., R. Gottardi, R. Raiteri, S. Miot, I. Martin, R. Imer, U. Staufer, A. Raducanu, M. Duggelin, W. Baschong, A. U. Daniels, N. F. Friederich, A. Aszodi, and U. Aebi. 2009. Early detection of aging cartilage and osteoarthritis in mice and patient samples using atomic force microscopy. Nat Nanotechnol 4:186-192.

159. Bao, G., and S. Suresh. 2003. Cell and molecular mechanics of biological materials. Nat Mater 2:715-725.

160. Martens, J. C., and M. Radmacher. 2008. Softening of the actin cytoskeleton by inhibition of myosin II. Pflug Arch Eur J Phy 456:95-100.

161. Rotsch, C., and M. Radmacher. 2000. Drug-induced changes of cytoskeletal structure and mechanics in fibroblasts: An atomic force microscopy study. Biophysical Journal 78:520-535.

162. Wu, H. W., T. Kuhn, and V. T. Moy. 1998. Mechanical properties of l929 cells measured by atomic force microscopy: Effects of anticytoskeletal drugs and membrane crosslinking. Scanning 20:389-397.

163. Kraning-Rush, C. M., S. P. Carey, J. P. Califano, B. N. Smith, and C. A. Reinhart-King. 2011. The role of the cytoskeleton in cellular force generation in 2D and 3D environments. Phys Biol 8.

164. Chartier, L., L. L. Rankin, R. E. Allen, Y. Kato, N. Fusetani, H. Karaki, S. Watabe, and D. J. Hartshorne. 1991. Calyculin-a Increases the Level of Protein-Phosphorylation and Changes the Shape of 3t3 Fibroblasts. Cell Motil Cytoskel 18:26-40.

165. Hirano, K., L. Chartier, R. G. Taylor, R. E. Allen, N. Fusetani, H. Karaki, and D. J. Hartshorne. 1992. Changes in the Cytoskeleton of 3t3 Fibroblasts Induced by the Phosphatase Inhibitor, Calyculin-A. J Muscle Res Cell M 13:341-353.

166. Peterson, L. J., Z. Rajfur, A. S. Maddox, C. D. Freel, Y. Chen, M. Edlund, C. Otey, and K. Burridge. 2004. Simultaneous stretching and contraction of stress fibers in vivo. Mol Biol Cell 15:3497-3508.

167. Stricker, J., Y. Aratyn-Schaus, P. W. Oakes, and M. L. Gardel. 2011. Spatiotemporal Constraints on the Force-Dependent Growth of Focal Adhesions. Biophys J 100:2883-2893.

168. Lu, L., S. J. Oswald, H. Ngu, and F. C. P. Yin. 2008. Mechanical Properties of Actin Stress Fibers in Living Cells. Biophys J 95:6060-6071.

169. Sen, S., and S. Kumar. 2009. Cell-Matrix De-Adhesion Dynamics Reflect Contractile Mechanics. Cell Mol Bioeng 2:218-230.

170. Guolla, L., M. Bertrand, K. Haase, and A. E. Pelling. 2012. Force transduction and strain dynamics in actin stress fibres in response to nanonewton forces. J Cell Sci 125:603-613.

171. Danowski, B. A. 1989. Fibroblast Contractility and Actin Organization Are Stimulated by Microtubule Inhibitors. J Cell Sci 93:255-266.

172. Kolodney, M. S., and E. L. Elson. 1995. Contraction Due to Microtubule Disruption Is Associated with Increased Phosphorylation of Myosin Regulatory Light-Chain. P Natl Acad Sci USA 92:10252-10256.

173. Ezratty, E. J., M. A. Partridge, and G. G. Gundersen. 2005. Microtubule-induced focal adhesion disassembly is mediated by dynamin and focal adhesion kinase. Nat Cell Biol 7:581-U515.

174. Wirtz, D., K. Konstantopoulos, and P. C. Searson. 2011. The physics of cancer: the role of physical interactions and mechanical forces in metastasis. Nat Rev Cancer 11:512-522.

175. Orr, A. W., B. P. Helmke, B. R. Blackman, and M. A. Schwartz. 2006. Mechanisms of mechanotransduction. Dev Cell 10:11-20.

176. Schwarz, U. S., and M. L. Gardel. 2012. United we stand - integrating the actin cytoskeleton and cell-matrix adhesions in cellular mechanotransduction. J Cell Sci 125:3051-3060.

177. Lemmon, C. A., C. S. Chen, and L. H. Romer. 2009. Cell Traction Forces Direct Fibronectin Matrix Assembly. Biophys J 96:729-738.

178. Lu, L., Y. F. Feng, W. J. Hucker, S. J. Oswald, G. D. Longmore, and F. C. P. Yin. 2008. Actin stress fiber pre-extension in human aortic endothelial cells. Cell Motil Cytoskel 65:281-294.

179. Hemsley, A. L., D. Hernandez, C. Mason, A. E. Pelling, and F. S. Veraitch. 2011. Precisely delivered nanomechanical forces induce blebbing in undifferentiated mouse embryonic stem cells. Cell Health Cytoskelet 3:23-34.

180. Lin, A. J., N. L. Slack, A. Ahmad, I. Koltover, C. X. George, C. E. Samuel, and C. R. Safinya. 2000. Structure and structure-function studies of lipid/plasmid DNA complexes. J Drug Target 8:13-27.

181. Al-Rekabi, Z., and A. E. Pelling. 2013. Cross talk between matrix elasticity and mechanical force regulates myoblast traction dynamics. Phys Biol 10:066003.

182. Carl, P., C. H. Kwok, G. Manderson, D. W. Speicher, and D. E. Discher. 2001. Forced unfolding modulated by disulfide bonds in the Ig domains of a cell adhesion molecule. P Natl Acad Sci USA 98:1565-1570.

183. Harris, A. R., and G. T. Charras. 2011. Experimental validation of atomic force microscopy-based cell elasticity measurements. Nanotechnology 22:345102.

184. Silberberg, Y. R., G. E. Yakubov, M. A. Horton, and A. E. Pelling. 2009. Cell nanomechanics and focal adhesions are regulated by retinol and conjugated linoleic acid in a dose-dependent manner. Nanotechnology 20.

185. Suresh, S., J. Spatz, J. P. Mills, A. Micoulet, M. Dao, C. T. Lim, M. Beil, and T. Seufferlein. 2005. Connections between single-cell biomechanics and human disease states: gastrointestinal cancer and malaria. Acta Biomaterialia 1:15-30.

186. Cai, X. F., X. B. Xing, J. Y. Cai, Q. Chen, S. X. Wu, and F. C. Huang. 2010. Connection between biomechanics and cytoskeleton structure of lymphocyte and Jurkat cells: An AFM study. Micron 41:257-262.

187. Marquez, J. P., E. L. Elson, and G. M. Genin. 2010. Whole cell mechanics of contractile fibroblasts: relations between effective cellular and extracellular matrix moduli. Philos T R Soc A 368:635-654.

188. Hoebeke, J., G. Van Nijen, and M. De Brabander. 1976. Interaction of oncodazole (R 17934), a new anti-tumoral drug with rat brain tubulin. Biochem Bioph Res Co 69:319-324.

189. Ishihara, H., B. L. Martin, D. L. Brautigan, H. Karaki, H. Ozaki, Y. Kato, N. Fusetani, S. Watabe, K. Hashimoto, D. Uemura, and D. J. Hartshorne. 1989. Calyculin-a and Okadaic Acid - Inhibitors of Protein Phosphatase-Activity. Biochem Bioph Res Co 159:871-877.

190. Rhee, S., H. Jiang, C. H. Ho, and F. Grinnell. 2007. Microtubule function in fibroblast spreading is modulated according to the tension state of cell-matrix interactions. P Natl Acad Sci USA 104:5425-5430.

191. Aratyn-Schaus, Y., P. W. Oakes, and M. L. Gardel. 2011. Dynamic and structural signatures of lamellar actomyosin force generation. Mol Biol Cell 22:1330-1339.

192. Takai, E., K. D. Costa, A. Shaheen, C. T. Hung, and X. E. Guo. 2005. Osteoblast elastic modulus measured by atomic force microscopy is substrate dependent. Ann Biomed Eng 33:963-971.

193. Chou, S. Y., C. M. Cheng, and P. R. Leduc. 2009. Composite polymer systems with control of local substrate elasticity and their effect on cytoskeletal and morphological characteristics of adherent cells. Biomaterials 30:3136-3142.

194. Keselowsky, B. G., D. M. Collard, and A. J. Garcia. 2004. Surface chemistry modulates focal adhesion composition and signaling through changes in integrin binding. Biomaterials 25:5947-5954.

195. Sampson, N. S., M. Mrksich, and C. R. Bertozzi. 2001. Surface molecular recognition. P Natl Acad Sci USA 98:12870-12871.

196. Hoffman, B. D., C. Grashoff, and M. A. Schwartz. 2011. Dynamic molecular processes mediate cellular mechanotransduction. Nature 475:316-323.

197. Humphrey, J. D. 2008. Vascular adaptation and mechanical homeostasis at tissue, cellular, and sub-cellular levels. Cell Biochem Biophys 50:53-78.

198. Butcher, D. T., T. Alliston, and V. M. Weaver. 2009. A tense situation: forcing tumour progression. Nat Rev Cancer 9:108-122.

199. Chiquet, M., V. Tunc-Civelek, and A. Sarasa-Renedo. 2007. Gene regulation by mechanotransduction in fibroblasts. Appl Physiol Nutr Me 32:967-973.

200. Maloney, J. M., D. Nikova, F. Lautenschlager, E. Clarke, R. Langer, J. Guck, and K. J. Van Vliet. 2010. Mesenchymal Stem Cell Mechanics from the Attached to the Suspended State. Biophys J 99:2479-2487.

201. Vogel, V., and M. P. Sheetz. 2006. Local force and geometry sensing regulate cell functions. Nat Rev Mol Cell Bio 7:265-275.

202. Balaban, N. Q., U. S. Schwarz, D. Riveline, P. Goichberg, G. Tzur, I. Sabanay, D. Mahalu, S. Safran, A. Bershadsky, L. Addadi, and B. Geiger. 2001. Force and focal adhesion assembly: a close relationship studied using elastic micropatterned substrates. Nat Cell Biol 3:466-472.

203. Riveline, D., E. Zamir, N. Q. Balaban, U. S. Schwarz, T. Ishizaki, S. Narumiya, Z. Kam, B. Geiger, and A. D. Bershadsky. 2001. Focal contacts as mechanosensors: Externally applied local mechanical force induces growth of focal contacts by an mDia1-dependent and ROCK-independent mechanism. J Cell Biol 153:1175-1185.

204. Glogauer, M., P. Arora, G. Yao, I. Sokholov, J. Ferrier, and C. A. G. McCulloch. 1997. Calcium ions and tyrosine phosphorylation interact coordinately with actin to regulate cytoprotective responses to stretching. J Cell Sci 110:11-21.

205. Pourati, J., A. Maniotis, D. Spiegel, J. L. Schaffer, J. P. Butler, J. J. Fredberg, D. E. Ingber, D. Stamenovic, and N. Wang. 1998. Is cytoskeletal tension a major

determinant of cell deformability in adherent endothelial cells? Am J Physiol-Cell Ph 274:C1283-C1289.

206. von Wichert, G., B. Haimovich, G. S. Feng, and M. P. Sheetz. 2003. Force-dependent integrin-cytoskeleton linkage formation requires downregulation of focal complex dynamics by Shp2. Embo J 22:5023-5035.

207. Lo, C. M., D. B. Buxton, G. C. H. Chua, M. Dembo, R. S. Adelstein, and Y. L. Wang. 2004. Nonmuscle myosin IIB is involved in the guidance of fibroblast migration. Mol Biol Cell 15:982-989.

208. Ulrich, T. A., E. M. D. Pardo, and S. Kumar. 2009. The Mechanical Rigidity of the Extracellular Matrix Regulates the Structure, Motility, and Proliferation of Glioma Cells. Cancer Res 69:4167-4174.

209. Rodriguez, O. C., A. W. Schaefer, C. A. Mandato, P. Forscher, W. M. Bement, and C. M. Waterman-Storer. 2003. Conserved microtubule-actin interactions in cell movement and morphogenesis. Nat Cell Biol 5:599-609.

210. Wang, N., K. Naruse, D. Stamenovic, J. J. Fredberg, S. M. Mijailovich, I. M. Toric-Norrelykke, T. Polte, R. Mannix, and D. E. Ingber. 2001. Mechanical behavior in living cells consistent with the tensegrity model. P Natl Acad Sci USA 98:7765-7770.

211. Silberberg, Y. R., A. E. Pelling, G. E. Yakubov, W. R. Crum, D. J. Hawkes, and M. A. Horton. 2008. Mitochondrial displacements in response to nanomechanical forces. Journal of Molecular Recognition 21:30-36.

212. Zimmer, C. C., L. F. Shi, Y. P. Shih, J. R. Li, L. Jin, S. H. Lo, and G. Y. Liu. 2012. F-Actin reassembly during focal adhesion impacts single cell mechanics and nanoscale membrane structure. Sci China Chem 55:1922-1930.

213. Balland, M., N. Desprat, D. Icard, S. Fereol, A. Asnacios, J. Browaeys, S. Henon, and F. Gallet. 2006. Power laws in microrheology experiments on living cells: Comparative analysis and modeling. Phys Rev E 74:021911.

214. Putnam, A. J., K. Schultz, and D. J. Mooney. 2001. Control of microtubule assembly by extracellular matrix and externally applied strain. Am J Physiol-Cell Ph 280:C556-C564.

215. Putnam, A. J., J. J. Cunningham, B. B. L. Pillemer, and D. J. Mooney. 2003. External mechanical strain regulates membrane targeting of Rho GTPases by controlling microtubule assembly. Am J Physiol-Cell Ph 284:C627-C639.

216. Pelham, R. J., and Y. L. Wang. 1999. High resolution detection of mechanical forces exerted by locomoting fibroblasts on the substrate. Mol Biol Cell 10:935-945.

217. Biton, Y. Y., and S. A. Safran. 2010. Theory of the mechanical response of focal adhesions to shear flow. Journal of Physics-Condensed Matter 22:-.

218. Chen, C. S., J. Tan, and J. Tien. 2004. Mechanotransduction at cell-matrix and cell-cell contacts. Annual Review of Biomedical Engineering 6:275-302.

219. Goldyn, A. M., B. A. Rioja, J. P. Spatz, C. Ballestrem, and R. Kemkemer. 2009. Force-induced cell polarisation is linked to RhoA-driven microtubule-independent focal-adhesion sliding. J Cell Sci 122:3644-3651.

220. Mierke, C. T., P. Kollmannsberger, D. P. Zitterbart, J. Smith, B. Fabry, and W. H. Goldmann. 2008. Mechano-coupling and regulation of contractility by the vinculin tail domain. Biophys J 94:661-670.

221. Ting, L. H., J. R. Jahn, J. I. Jung, B. R. Shuman, S. Feghhi, S. J. Han, M. L. Rodriguez, and N. J. Sniadecki. 2012. Flow mechanotransduction regulates traction forces, intercellular forces, and adherens junctions. Am J Physiol-Heart C 302:H2220-H2229.

222. D'Angelo, F., I. Armentano, S. Mattioli, L. Crispoltoni, R. Tiribuzi, G. G. Cerulli, C. A. Palmerini, J. M. Kenny, S. Martino, and A. Orlacchio. 2010. Micropatterned Hydrogenated Amorphous Carbon Guides Mesenchymal Stem Cells Towards Neuronal Differentiation. Eur Cells Mater 20:231-244.

223. Rape, A. D., W. H. Guo, and Y. L. Wang. 2011. Responses of Cells to Adhesion-Mediated Signals: A Universal Mechanism. Mechanobiology of Cell-Cell and Cell-Matrix Interactions 1.

224. Paszek, M. J., and V. M. Weaver. 2004. The tension mounts: Mechanics meets morphogenesis and malignancy. J Mammary Gland Biol 9:325-342.

225. Sarntinoranont, M., F. Rooney, and M. Ferrari. 2003. Interstitial stress and fluid pressure within a growing tumor. Ann Biomed Eng 31:327-335.

226. Yang, Y. F., A. Creeer, B. Jemiolo, and S. Trappe. 2005. Time course of myogenic and metabolic gene expression in response to acute exercise in human skeletal muscle. J Appl Physiol 98:1745-1752.

227. Bischoff, R. 1990. Interaction between Satellite Cells and Skeletal-Muscle Fibers. Development 109:943-952.

228. Hawke, T. J., and D. J. Geary. 2001. Myogenic satellite cells: physiology to molecular biology. (vol 91, pg 534, 2001). J Appl Physiol 91:Cp4-Cp4.

229. Bosse, Y., L. Y. Chin, P. D. Pare, and C. Y. Seow. 2010. Chronic activation in shortened airway smooth muscle: a synergistic combination underlying airway hyperresponsiveness? American journal of respiratory cell and molecular biology 42:341-348.

230. Bosse, Y., L. Y. Chin, P. D. Pare, and C. Y. Seow. 2009. Adaptation of airway smooth muscle to basal tone: relevance to airway hyperresponsiveness. American journal of respiratory cell and molecular biology 40:13-18.

231. Burridge, K., and M. ChrzanowskaWodnicka. 1996. Focal adhesions, contractility, and signaling. Annual Review of Cell and Developmental Biology 12:463-518.

232. Gittes, F., B. Mickey, J. Nettleton, and J. Howard. 1993. Flexural Rigidity of Microtubules and Actin-Filaments Measured from Thermal Fluctuations in Shape. Journal of Cell Biology 120:923-934.

233. Snyder, J. A., and J. R. Mcintosh. 1975. Initiation and Growth of Microtubules from Mitotic Centers in Lysed Mammalian-Cells. J Cell Biol 67:A409-A409.

234. Mucke, N., L. Kreplak, R. Kirmse, T. Wedig, H. Herrmann, U. Aebi, and J. Langowski. 2004. Assessing the flexibility of intermediate filaments by atomic force microscopy. Journal of Molecular Biology 335:1241-1250.

235. Georgatos, S. D., and G. Blobel. 1987. Lamin-B Constitutes an Intermediate Filament Attachment Site at the Nuclear-Envelope. J Cell Biol 105:117-125.

236. Bershadsky, A. D., N. Q. Balaban, and B. Geiger. 2003. Adhesion-dependent cell mechanosensitivity. Annual Review of Cell and Developmental Biology 19:677-695.

237. Jaalouk, D. E., and J. Lammerding. 2009. Mechanotransduction gone awry. Nature Reviews Molecular Cell Biology 10:63-73.

238. Burridge, K. 1997. Focal adhesions: Assembly and signaling. Faseb J 11:A1001-A1001.

239. Nobes, C. D., and A. Hall. 1995. Rho, Rac, and Cdc42 Gtpases Regulate the Assembly of Multimolecular Focal Complexes Associated with Actin Stress Fibers, Lamellipodia, and Filopodia. Cell 81:53-62.

240. Kiosses, W. B., S. J. Shattil, N. Pampori, and M. A. Schwartz. 2001. Rac recruits high-affinity integrin alpha v beta 3 to lamellipodia in endothelial cell migration. Nat Cell Biol 3:316-320.

241. Geiger, B., and A. Bershadsky. 2001. Assembly and mechanosensory function of focal contacts. Curr Opin Cell Biol 13:584-592.

242. Hinz, B., V. Dugina, C. Ballestrem, B. Wehrle-Haller, and C. Chaponnier. 2003. alpha-smooth muscle actin is crucial for focal adhesion maturation in myofibroblasts. Mol Biol Cell 14:2508-2519.

243. Gabbiani, G. 2003. The myofibroblast in wound healing and fibrocontractive diseases. J Pathol 200:500-503.

244. Zamir, E., M. Katz, Y. Posen, N. Erez, K. M. Yamada, B. Z. Katz, S. Lin, D. C. Lin, A. Bershadsky, Z. Kam, and B. Geiger. 2000. Dynamics and segregation of cell-matrix adhesions in cultured fibroblasts. Nat Cell Biol 2:191-196.

245. Ridley, A. J., M. A. Schwartz, K. Burridge, R. A. Firtel, M. H. Ginsberg, G. Borisy, J. T. Parsons, and A. R. Horwitz. 2003. Cell migration: Integrating signals from front to back. Science 302:1704-1709.

246. Beningo, K. A., and Y. L. Wang. 2002. Flexible substrata for the detection of cellular traction forces. Trends in Cell Biology 12:79-84.

247. Galbraith, C. G., K. M. Yamada, and M. P. Sheetz. 2002. The relationship between force and focal complex development. J Cell Biol 159:695-705.

248. Friedland, J. C., M. H. Lee, and D. Boettiger. 2009. Mechanically Activated Integrin Switch Controls alpha(5)beta(1) Function. Science 323:642-644.

249. Chu, P. Y., L. Y. Huang, C. H. Hsu, C. C. Liang, J. L. Guan, T. H. Huang, and T. L. Shen. 2009. Tyrosine Phosphorylation of Growth Factor Receptor-bound Protein-7 by Focal Adhesion Kinase in the Regulation of Cell Migration, Proliferation, and Tumorigenesis. J. Biol. Chem. 284:20215-20226.

250. Mitra, S. K., D. A. Hanson, and D. D. Schlaepfer. 2005. Focal adhesion kinase: In command and control of cell motility. Nat Rev Mol Cell Bio 6:56-68.

251. Clark, E. A., and J. S. Brugge. 1995. Integrins and Signal-Transduction Pathways - the Road Taken. Science 268:233-239.

252. Leavesley, D. I., G. D. Ferguson, E. A. Wayner, and D. A. Cheresh. 1992. Requirement of the Integrin-Beta-3 Subunit for Carcinoma Cell Spreading or Migration on Vitronectin and Fibrinogen. J Cell Biol 117:1101-1107.

253. Lippi, G., M. Franchini, and G. Targher. 2011. Arterial thrombus formation in cardiovascular disease. Nat Rev Cardiol 8:502-512.

254. Vincent, J. F. V. 1990. Structured biomaterials. Princeton University Press, Princeton, N. J.

255. Buck, C. A., and A. F. Horowitz. 1987. Cell Surface Receptors for Extracellular Matrix Molecules. Annual Review of Cell Biology 3:179-205.

256. Hynes, R. O. 1992. Integrins - Versatility, Modulation, and Signaling in Cell-Adhesion. Cell 69:11-25.

257. Streuli, C. 1999. Extracellular matrix remodelling and cellular differentiation. Current Opinion in Cell Biology 11:634-640.

258. Hynes, R. O. 2009. The Extracellular Matrix: Not Just Pretty Fibrils. Science 326:1216-1219.

259. Singh, P., C. Carraher, and J. E. Schwarzbauer. 2010. Assembly of Fibronectin Extracellular Matrix. Annual Review of Cell and Developmental Biology 26:397-419.

260. Galbraith, C. G., K. M. Yamada, and J. A. Galbraith. 2007. Polymerizing actin fibers position integrins primed to probe for adhesion sites. Science 315:992-995.

261. Partridge, M. A., and E. E. Marcantonio. 2006. Initiation of attachment and generation of mature focal adhesions by integrin-containing filopodia in cell spreading. Mol. Biol. Cell 17:4237-4248.

262. Hoffmann, B., and C. Scaeffer. 2010. Filopdial focal complexes direct adhesion and force generation towards filopodia outgrowth. Cell Adh Migr 4:190-193.

263. Sage, E. H. 2001. Regulation of interactions between cells and extracellular matrix: a command performance on several stages. J. Clin. Invest. 107:781-783.

264. Chan, W. C. W., D. J. Maxwell, X. H. Gao, R. E. Bailey, M. Y. Han, and S. M. Nie. 2002. Luminescent quantum dots for multiplexed biological detection and imaging. Curr Opin Biotech 13:40-46.
265. Giepmans, B. N. G., S. R. Adams, M. H. Ellisman, and R. Y. Tsien. 2006. Review - The fluorescent toolbox for assessing protein location and function. Science 312:217-224.
266. Shimomura, O., F. H. Johnson, and Y. Saiga. 1962. Extraction, Purification and Properties of Aequorin, a Bioluminescent Protein from Luminous Hydromedusan, Aequorea. J Cell Compar Physl 59:223-&.
267. Chalfie, M., Y. Tu, G. Euskirchen, W. W. Ward, and D. C. Prasher. 1994. Green Fluorescent Protein as a Marker for Gene-Expression. Science 263:802-805.
268. Felgner, P. L., T. R. Gadek, M. Holm, R. Roman, H. W. Chan, M. Wenz, J. P. Northrop, G. M. Ringold, and M. Danielsen. 1987. Lipofection - a Highly Efficient, Lipid-Mediated DNA-Transfection Procedure. P Natl Acad Sci USA 84:7413-7417.
269. Valeur, B., editor. 2001. Molecular Fluorescence: Principles and Applications. Wiley-VCH.
270. Jablonski, A. 1935. About the mechanism of photo-luminescence of dye phosphors. Z Phys 94:38-46.
271. Goeppert Mayeri, M. 1931. Elementary pro cesses with two-quantum transitions. Ann. d. Physik 9.
272. Muller, M., editor. 2002. Introduction to Confocal Fluorescence Microscopy. Shaker Publishing, Maastricht.
273. Stevens, J. K., L. R. Mills, and J. E. Trogadis, editors. 1994. Three-dimensional Confocal Microscopy: Volume Investigation of Biological Systems. Academic Press, San Diego.
274. Corle, T. R., and G. S. Kino. 1996. Confocal scanning optical microscopy and related imaging systems. Academic Press, San Diego.
275. Sheppard, C., and D. Shotton. 1997. Confocal laser scanning microscopy. BIOS Scientifc; Springer in association with the Royal Microscopical Society, Oxford, New York.

276. Stevens, J. K., L. R. Mills, and J. E. Trogadis. 1994. Three-dimensional Confocal Microscopy: Volume Investogation of Biological Systems. Academic Press, San Diego.

277. Barnes, H. A., J. F. Hutton, and K. Walters. 1989. An Introduction to rheology. Elselvier, Amsterdam.

278. Macosko, C. M. 1994. Rheology-Principles, Meausrements and Applications. John Wiley & Sons.

279. Plazek, D. J. 1968. Magnetic Bearing Torsional Creep Apparatus. J Polym Sci A2 6:621-&.

280. Benmouffok-Benbelkacem, G., F. Caton, C. Baravian, and S. Skali-Lami. 2010. Non-linear viscoelasticity and temporal behavior of typical yield stress fluids: Carbopol, Xanthan and Ketchup. Rheol Acta 49:305-314.

281. Altman, D. G., and J. M. Bland. 2005. Statistics notes - Standard deviations and standard errors. Brit Med J 331:903-903.

282. Altman, D. G., and J. M. Bland. 1995. The Normal-Distribution. Brit Med J 310:298-298.

283. Quinn, G. P., and M. J. Keough. 2002. Experimental Design and Data Analysis for Biologists. Cambridge University Press, Cambridge.

Appendix A: The Main Components for Cell Adhesion

Cytoskeleton

The cytoskeleton is composed of several molecules and protein assemblies of which are outlined below. These include the filamentous structures which are largely involved in regulating the mechanical dynamics of the cell (*Actin*, *Microtubules* and *Intermediate Filaments*). In addition to these structural components, there are protein complexes which allow the cell to adhere and attach to its surroundings and transmit mechanical forces in and out of the cell (known as FAs).

Actin Filaments: Actin is formed by the polymerization of monomeric actin (G-actin), which is globular in-shape into filamentous strands of F-actin containing a structural polarity with ‘barbed’ and ‘pointed’ ends. Generally, the monomers consist of 375 amino acids with a molecular weight of about 43 kDa. When adenosine tri-phosphate (ATP) attaches to the barbed end, additional monomers are added which leads to the growth of the filament. At the pointed end, depolymerization takes place. Moreover, tertiary structures can be formed including fiber bundles (stress fibers (SF)) or a three dimensional lattice-like structure formed from the actin filaments with the involvement of various actin-binding proteins as Arp2/3, fimbrin and α-actinin (231). Actin is believed to be the primary structural component of most cells such that it responds actively to external forces and is crucial during the migration process in the formation of the leading-edge lamellipodium protrusions (Fig. A1a).

Microtubules (MTs): They are the second major ingredient of the filamentous cytoskeleton. They primarily consist of polymerized filaments from α- and β-tubulin monomers and form a helical arrangement. Moreover, both peptides have a molecular weight of 55 kDa and they arrange themselves into a small hallow cylinder. The outer diameter of the cylindrical tube is about 25 nm and interestingly microtubules have the same effective Young’s Modulus as actin (1-3 $\times\ 10^9$ Pa); in addition these filaments have a persistence length of about 6 mm (232). During mitosis, microtubules extend outward from the centrosomes to form mitotic spindles which are responsible for the allocation of chromosomes to daughter cells (233), (Fig. A1b).

Intermediate Filaments: These filaments are part of a subfamily of proteins containing more than fifty different members. The most common structure they share is the central α-helical domain, which consists of over 300 residues that form an entangled coil. The dimers assemble themselves into a staggered array forming tetramers that connect end-to-end forming protofilaments. These in turn organize into rope-like structures, where each contains eight protofilaments with an average persistence length of about 1 µm (234). Interestingly, intermediate filaments unlike actin and microtubules form with the need of energy (GTP or ATP). Intermediate filaments are relatively stable and they are involved in providing tensile strength for the cell. In addition they may be involved in specialized cell-cell junctions (147). For example, lamins, one of the various types of intermediate filaments form filamentous support inside the inner nuclear membrane; therefore, they are vital to the re-assembly of the nuclear envelope after cell division (147, 235), (Fig. A1c).

The three protein structures that constitute the cytoskeletal network are not independent of one another but interconnected between each other, organelles and the external environment. Extensive binding proteins modulate these principal members. Some of these secondary proteins serve regulatory functions, such as capping and sequestering proteins, and some serve structural functions, such as bundling and crosslinking. Particular cytoskeleton associated proteins which cannot be ignored are motor proteins. Myosin-II contains two actin-binding domains, which are capable of ‘walking’ along actin fibers towards the plus-end following the hydrolysis of ATP. Generally, in order to provide tension or contraction inside the cell, adjacent parallel bundles of actin must have opposite polarity for myosin-II in order to pull the fibers toward each other. Kinesin and dyneins, which are transporter molecules are often found as a complex in MTs. One end is bound to the MT and the other end is bound to that which is being transported to; these molecules ‘walk along the MT, bringing necessary materials to where they are needed in the cell. Myosin-V acts like kinesins and dyneins, where they not also ‘walk’ along the actin filaments but also transport molecules in a similar manner.

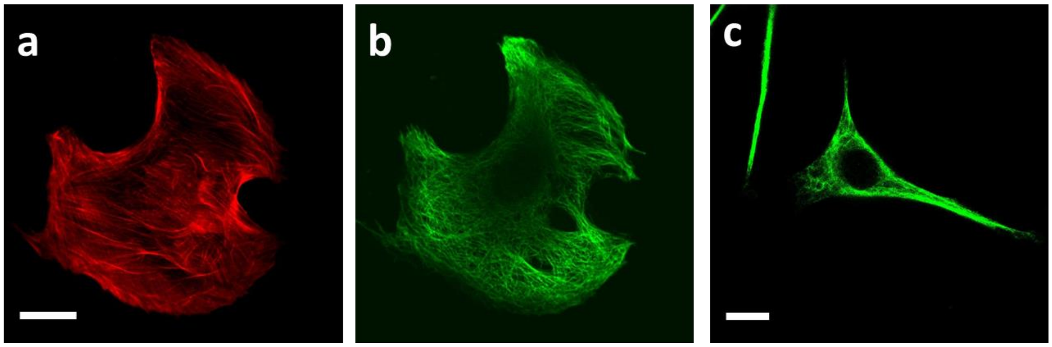

Figure A1 Filamentous networks of the CSK. Confocal images of the individual filamentous networks of the cytoskeleton for NIH 3T3 cells, where (a) is filamentous actin, (b) are MTs and (c) are intermediate filaments from a separate cell. Images were obtained using confocal microscopy (Section 2.1.3), and cells were stained (Section 3.2) for each particular component. Scale bar: 34μm for a & b. Scale bar: 21μm for c.

Focal Adhesions (FAs)

Cytoskeletal (internal) and external mechanical forces are applied to the anchor sites known as focal adhesions (FAs), (Fig. A2a & b”box”). Specific heterodimeric (α-β) transmembrane receptors of the integrin family link the ECM to the cytoskeleton. This transmembrane interaction is mediated by a complex network of adhesion proteins that form a submembrane plaque (231, 236, 237). FAs are an assembly of ECM proteins, transmembrane receptors or ligands, and cytoplasmic structural and signaling proteins, including $\alpha_v\beta_3$ and $\alpha_5\beta_1$ integrins, vinculin, paxilin, talin, zyxin, protein tyrosine kinases and phosphatases (231, 236, 238, 239). FAs are small punctate contacts known as focal complexes (FCs) which are precursors of mature FAs. Focal complexes develop after cultured cells come into contact with a compliant surface (239). These complexes are generally small and located at the boundary of a spreading cell or at the leading edge of a migrating cell (73, 240). Large, mature FAs are elongated streak-like structures that link stress fibers (SFs) at their ends (236, 237, 241). These FAs can develop into ‘supermature’ FAs, which appear as elongated cylindrical assemblies of proteins. FAs are a result of the fusion of several large FAs and are also associated with α-SMA-positive bundles of SFs (242), which are found in cells that are cultured on rigid surfaces as glass or plastic or when fibroblasts differentiate into myofibroblasts during wound healing (243). Zamir et al. (244) found that cells expressing genetically engineered FA proteins linked to green fluorescent protein (GFP) evolve into FAs as more adhesion proteins and actin are recruited to the adhesion sites. Balaban et al. (202), investigated the relationship between the local forces that the cell exerts on the substrate and the assembly of proteins at the focal adhesion sites by combining micropatterning of elastomer substrates and fluorescence imaging. There was a strong correlation between the applied cellular traction forces and FA area. The magnitude of forces at FAs was cell type dependent and was found to range from ~20nN in fibroblasts to ~70nN in cardiac myoblasts. Furthermore, this observed linear dependence between force and area of the FA suggests that a uniform stress is applied to the various FAs of the cell. Therefore, the growth of large FAs appears to require the application of sufficient mechanical force to the adhesions (202, 245).

More recent studies suggest that the mechanical forces have a direct role in the formation of FAs. Studies using elastic micropatterned substrates (202) and flexible substrates (67, 68, 77, 78, 246) demonstrated that deformations were produced as a result of the cell's attachment to the substrate, which produced local distribution of forces at their adhesion sites. Studies using this approach have demonstrated that the size of the individual FAs may be correlated with the distributed forces produced as result of cell adhesion (218). In another approach, studies have been performed in which external forces are directly applied to cell (34, 128, 203, 247). It was found that applying external forces with micropipette aspiration or micropatterned post with nanowires directly to cells led to FA remodelling, an increase in cell adhesion, and the direct observation of force-induced FA remodelling. These results suggest that intracellular tension against the ECM is necessary for the development of FAs. In addition the application of an external force causes FAs to increase in size and to strengthen their adhesion to the substrate.

Adhesions also provide the coordination of important biochemical signals which initiate changes in cell behaviour. For example, signalling through basic fibroblast growth factor receptors in endothelial cells requires ligation of the growth factor receptors $\alpha_v\beta_3$ and $\alpha_v\beta_5$, and since both receptors bind to different ECM proteins the response will depend on the underlying ECM. Increasing intracellular tension or applying external forces to living cells leads to increases in the growth of focal contacts and the activation of focal adhesion kinase

(FAK) (248). FAK appears to be one of the earliest markers of FA signalling whose activity changes with tension (218). Recent studies have shown that applying mechanical stretch increases phosphorylation of FAK and subsequently causes cells to increase in their proliferation (249, 250). These findings suggest that cytoskeletal tension may be transduced into a biochemical signal, possibly by changes in the activity of FAK, representing an important component of adhesion dependency in cells.

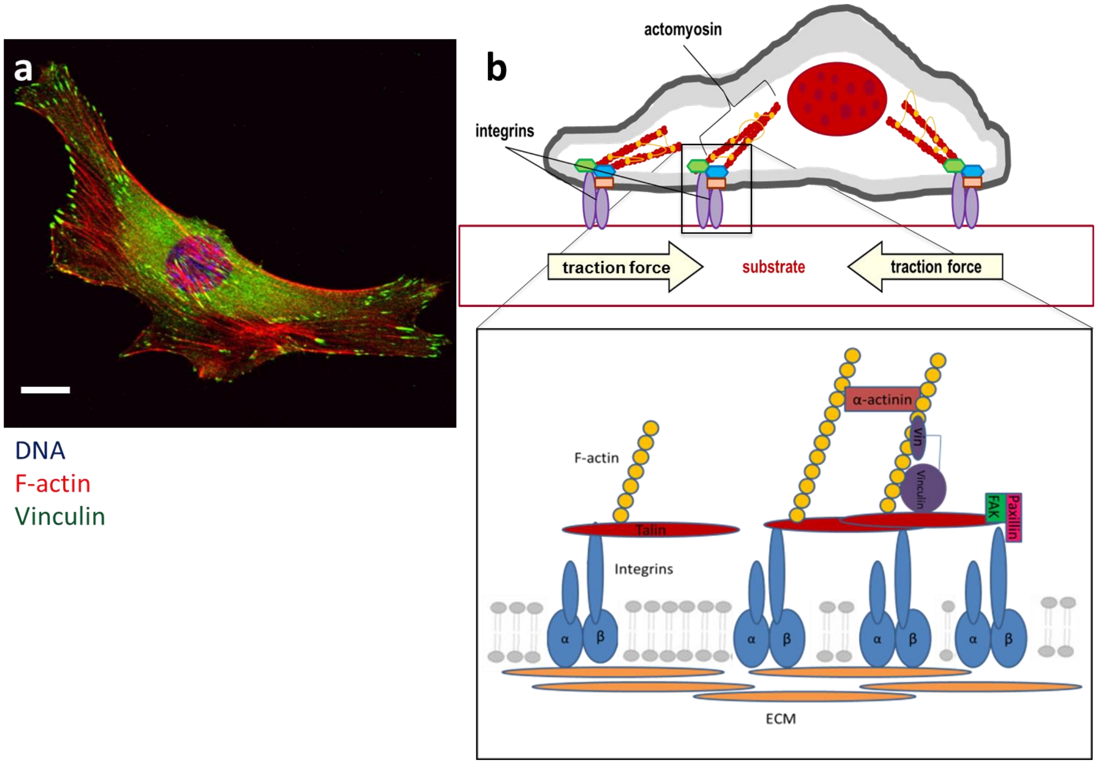

Figure A2 A Confocal and schematic representation of cellular attachment. (a) A triple stain of a C2C12 myoblast cell stained for F-actin (red), vinculin (green) and DNA (blue). Scale bar: 21µm. A schematic presentation of a cell on a flexible substrate is given in (b), the box shows how the FAs connect the ECM to the actin cytoskeleton in a complex including integrins, talin, vinculin and paxillin. Cell-substrate attachments are formed when filamentous actin are connected to a flexible substrate via FAs sites as vinculin, talin and integrin.

Integrins

Integrins are the major family of cell surface receptors which mediate attachment to the ECM and cell-cell interactions (Fig. A2b). Moreover, integrins are a family of structurally related glyocproteins. They are all α-β heterodimers. So far fifteen different α subunits and eight different β subunits have been identified. These subunits selectively heterodimerize to form one of twenty-one complexes and these complexes functionally behave as receptors for different ECM proteins (251). The β_1 integrin subfamily is the largest and most widely distributed. The β_1 subunit can form β heterodimers with nine different α subunits ($\alpha_{1\text{-}8}$ and α_v) and form the receptors for fibronectin, lamimin various collagens and vitronectin (252). The second subfamily is composed of one of the four α subunits ($\alpha_{L,}$ $\alpha_{M,}$ $\alpha_{X,}$ α_D) complexed with the β_2 subunit. The β_2 integrins mainly mediate cell-cell rather than cell-matrix interactions by binding specific ligands on other cells. The cyto-adhesions ($\alpha_{IIb}\beta_3$, $\alpha_v\beta_3$) form the third subfamily of integrins. They are found in a variety of cells, including blood platelets, and they bind several matrix proteins, including fibrinogen and play an important role in hemostasis and thrombosis (253).

Integrins function as transmemebrane linkers which mediate the interaction between the cytoskeleton and the ECM, which is required for cells to adhere to the matrix. The interaction of cells with the ECM regulates cell shape, motility, growth, differentiation and gene expression, through integrin-mediated signal transduction (251). Therefore, integrins function as signal transducer and regulators of cellular behaviour.

Extracellular Matrix (ECM)

Our understanding of both the structure and function of the extracellular matrix (ECM) has evolved from the early concept of a static “connective tissue” that ties everything together to one of a dynamic biomaterial that provides strength and elasticity (254), interacts with cell-surface receptors (255, 256) and controls the availability of growth factors (257). The ECM contains generally insoluble mature proteins, where some contain unique crosslinks, some have high amounts of sulphated polysaccharides, some are designed to be ‘sticky’ in terms of interacting with cells and others form complex adhesion surfaces and diffusion barriers between different cell layers (257-259) (Fig. A3). The macromolecules that make up the ECM are mainly produced locally by cells embedded in the matrix. These cells help to organize the matrix. In most connective tissues, the matrix macromolecules are secreted largely by cells called fibroblasts. Two main classes of extracellular macromolecules make up the matrix: (1) glycosaminglycans (GAG) or proteoglycans and (2) fibrous proteins, including elastin, collagen, fibronectin and laminin. The proteoglycan molecules in connective tissue form a highly hydrated gel-like material in which the fibrous proteins are embedded. The gel resists compressive forces while allowing the rapid diffusion of nutrients, hormones, and metabolites between the blood and tissue cells. The collagen fibers give strength and organize the matrix. The elastin fibers give it flexibility. Usually, proteoglycans amount to less than 10% of the weight of the fibrous proteins, but they form porous hydrated gels. The proteoglycans fill up most of the extracellular space, providing mechanical support to the tissue.

A special kind of extracellular matrix called basal lamina or basement membrane needs more attention. The lamina lie between two cell sheets (connective tissue and epithelial tissue) and act as a highly selective filter for proteins diffusing from connective tissue to epithelial tissue or vice versa. The basal lamina are also able to determine cell polarity, influence cell metabolism, organize the proteins in adjacent plasma membranes, promote cell survival, proliferation, or differentiation, and serve as specific highways for cell migration. Basal laminas are also important in tissue regeneration after injury.

As the cell binds to the components of the ECM, this action mediates the assembly of cell-matrix adhesions during locomotion. Filopodia attach to the ECM components through integrin receptors, allowing these structures to probe the rigidity or stiffness of the environment around them in order to promote the movement of cells (260). Integrin molecules accumulate within filopdia to mediate the initial cell-matrix adhesions (261).

The tension which is generated between the cytoskeletal network (via the action of contractile SFs), the linked ECM and the FAs, controls the cells ability to migrate and protrude filopodia. Cell-matrix adhesion therefore functions as a molecular ‘clutch’ to convert intracellular cytoskeletal assembly into protrusion and movement (262). Cells also interact with and modify ECM components mechanically, as well as chemically, to alter their alignment and composition in ways that influence cell fate, movement, polarization, and shape. For example, it is through the secretion of matricellular proteins that alter ECM composition, which in turn affects cell morphology (263).

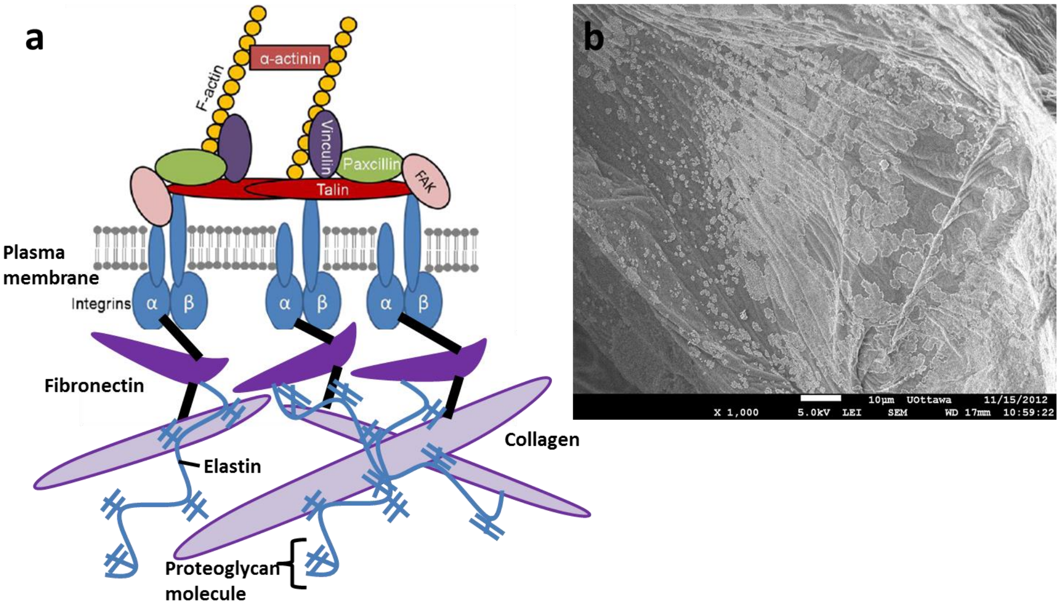

Figure A3 A schematic representation of ECM and an SEM image of ECM of an apple. (a) A schematic presentation of how the FAs connect connect the internal cytoskeleton to the ECM. The ECM is composed of proteoglycans and fibrous proteins: elastin, collagen, fibronectin and laminin. The proteoglycans are gel-like, which act to resist compressive forces while allowing the rapid diffusion of nutrients, hormones, and metabolites between the blood and tissue cells. The collagen fibers give strength and organize the matrix. The elastin fibers give it flexibility. (b) An SEM image of the ECM of a slice of apple where cells were de-cellularized by SDS, courtesy of Daniel Modulevsky (Pelling Lab member). Scale bar: 10µm.

Appendix B: Microscopy Techniques

In this section, I will describe in detail the advanced microscopy and imaging techniques used in the experiments performed in this thesis.

Phase Contrast Microscopy

The phase contrast microscope is widely used for examining specimens as biological tissues. It is a type of light microscopy that enhances contrasts of transparent and colorless objects by influencing the optical path of light. The phase contrast microscope is able to show components in a cell or bacteria, which would be very difficult to see in an ordinary light microscope. Using an ordinary (bright-field) transmitted-light microscope, the produced images of very thin transparent objects, like living cells of biological tissues, usually suffer from weak contrast, which makes it difficult and in most cases impossible to recognize and distinguish structures or image details in the sample. This is primarily due to the fact that light absorption of such objects is too low to provide sufficient amplitude changes of the transmitted light (bright-dark contrast). Nevertheless, individual sample structures as the cell nucleus or organelles show little density differences leading to small differences of the refractive indices and for this reason to different optical paths lengths. If light waves pass those structures, they experience a certain path phase shift that corresponds to the respective optical path lengths. The phase contrast technique is intended to convert such phase shifts into amplitude differences that are detectable by the human eye (bright-dark contrasts).

Basically light passes through an object that is more optically dense than the background; this causes the wave-fronts to be retarded with respect to the untouched, bypassing background light. The phase shift of the ‘object light’ is assumed to be 90º, which corresponds to an optical path difference of 1/4, as it is for most biological samples. To visualize the phase shifts in the object light, what one must do change the phase of the background light in such a way that the background and object light cancel each other out. Therefore, the object would appear dark against the background. In order to do that, the background light must be manipulated in such a way that it doesn’t affect the object light (which is already phase-shifted due to the object). This is can be done by placing an annular aperature (light ring) in the front focal plane of the condenser and a matching phase ring in the back focal plane of the objective.

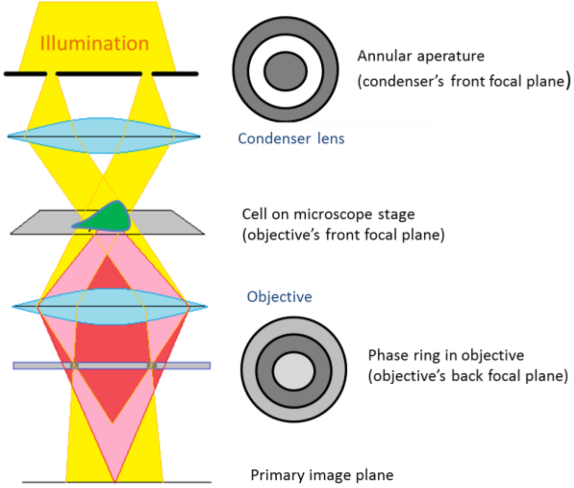

Figure B1 Schematic of phase contrast microscopy. A simplified assembly of a phase contrast microscope containing an annular aperature (light ring) in the condenser and an phase ring in the objective. The background light is colored rose and the object light is red.

This phase ring reduces the intensity of the background light by 90 % like a neutral density filter and it also adds a constant phase shift by 90º (1/4) like a quarter-wave plate. It is important to reduce the amplitude, because the object light is much less intense than the bright direct light. If the object is placed in the light path, the object light gets deflected, only slightly passing through the phase ring. Most of the object light passes by and remains unaffected as desired. By recombining the background and object light in the primary image plane, this ends up with an effective phase shift of about 180º (1/2). Moreover, to achieve the best contrast, this means that both phase shifts should complement one another as well as possible to 180º. For this reason, the properties of the phase ring must take into account the refractive index and the thickness of the samples. Therefore, phase contrast microscopy is a great tool for looking at cells, however it lacks specificity, therefore, to eliminate such a problem, epi-fluorescent microscopy is used.

Fluorescence Microscopy

Fluorescence microscopy is one of the most important techniques developed for in-vivo studies of living cells. Fluorescent probes are extremely useful for biological research, because they allow the study of the inner workings of cells with single molecule detection sensitivity and high specificity. The trick is to attach the fluorescent label to the macromolecule you are interested in studying. Researchers have developed several ways to fluorescently label macromolecules for live or fixed cell imaging including many types of fluorescent organic dyes that can be attached to antibodies for tagging purposes. More recently developed approaches use fluorescent probes that are either naturally fluorescent proteins or semi-conductor nanocyrstals (quantum dots) (264, 265).

There are several kinds of naturally fluorescent proteins that are used to label macromolecules, each with its own absorption and emission spectra, quantum yield and fluorescence lifetimes. The most commonly used naturally fluorescent protein is the green fluorescent protein (GFP). GFP is naturally found in a jellyfish (*Aequorea Victoria*, (266)). The jellyfish contains a bioluminescent protein, aequorin that emits blue light. The green fluorescent protein converts this light to green light, which is what we actually see when the jellyfish lights up. The cloning of the gene that encodes GFP was a breakthrough for live cell imaging because it became possible to genetically splice GFP codon within the genetic codes for other proteins (267) and thus have the cell synthesize the protein of interest with an attached GFP fluorescent marker. To attach these fluorescent proteins to the molecule of interest the genetic technique is called transfection (268). Transfections, involves cellular insertion of DNA plasmid (essentially a circular loop of DNA) that carries the genetic code for the protein of interest immediately followed by the genetic code for the fluorescent protein. Hence when this new DNA is incorporated into the cell nucleus, the cell starts its transcription, where it will produce the native protein fused to the fluorescent protein, effectively generating a protein with a built-in fluorescent tag.

Fluorescence and Jabłoński Energy Diagrams

To understand the principles of fluorescence imaging, it is important to first understand the fluorescence phenomenon. Analogous to the excited states of an atom, fluorescence can be explained using the Jabłoński energy diagram for the molecule where different energy states for the electrons in the system are arranged according to their energy-like rungs of a ladder (269).

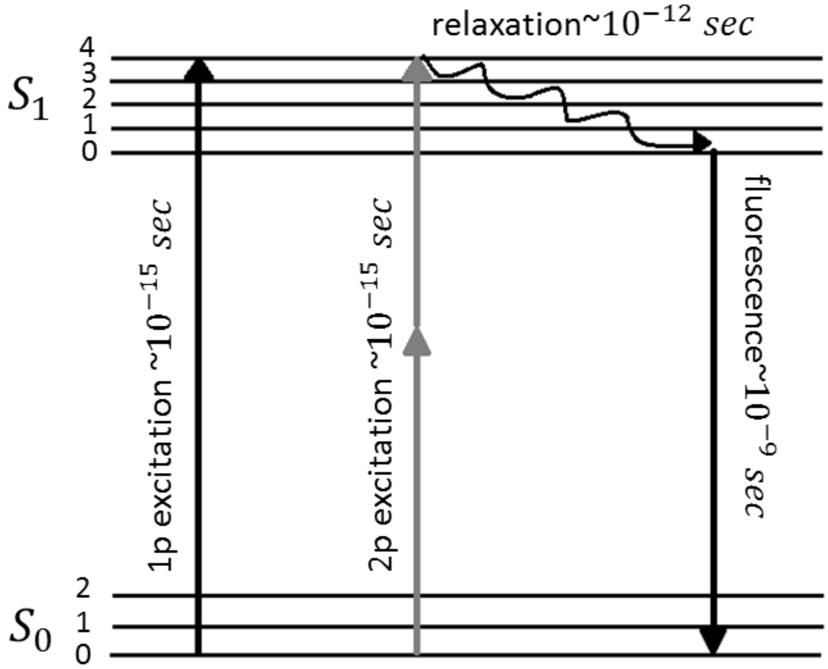

Figure B2: The Jabłoński energy diagram. S_o is the electronic ground state, S_1 is the excited singlet state, bars 0,1,2,3,4 represent vibrational energy levels in each electronic energy level.

The fluorescence excitation-emission process is illustrated in Fig. B2. Initially the molecule is in the singlet ground state S_o, and upon excitation an electron can be promoted to an excited singlet state S_1. The excitation source we are concerned with is light, and the energy needed to jump to an excited state is absorbed in a quanta-manner either in a single photon (270) (one photon absorption) or with two or more photons (N-photon absorption) whose energy quanta sum to equal the difference in energy between the ground and excited states (271). Two-photon absorption is a non-linear effect produced by the quasi-simultaneous absorption of two excitation photons of exactly half the energy of an allowed transition (271). One needs to tightly focus ultra-short pulsed lasers in order for the density of photons to be high enough to achieve non-linear excitation. After the rapid (~fs) absorption event, the fluorophore is usually in a high vibrational level of the first excited singlet state, which quickly (~ps) decays to the lowest excited singlet state vibrational energy level through non-radiative decay in a process called internal conversion. The fluorescence photon is emitted when the molecule drops from the lowest vibrational excited singlet state energy level back to the ground state. The lifetime of the excited state in this level is orders of magnitude longer (~ns) than the internal conversion step and if the electron decays back to the ground state from this level, a photon will be emitted by fluorescence emission. Due to the internal conversion, energy is lost so the fluorescence photon is red-shifted when compared to the (total) excitation energy. This shift in the emission wavelength, called the Stokes shift, is essential for fluorescence microscopy. The greater the Stokes shift, the easier it is to separate the excitation light from the emitted light. This separation is the basis of the sensitivity of fluorescence microscopy. Since the light intensity required to excite the molecules is much greater than the emitted light intensity, filters are needed to efficiently block out the excitation light and detect the weaker fluorescence emission

General Instrumentation of the Microscope

The optical microscope is the basic instrument used to image fluorescent molecules within the cells (Fig. B3).

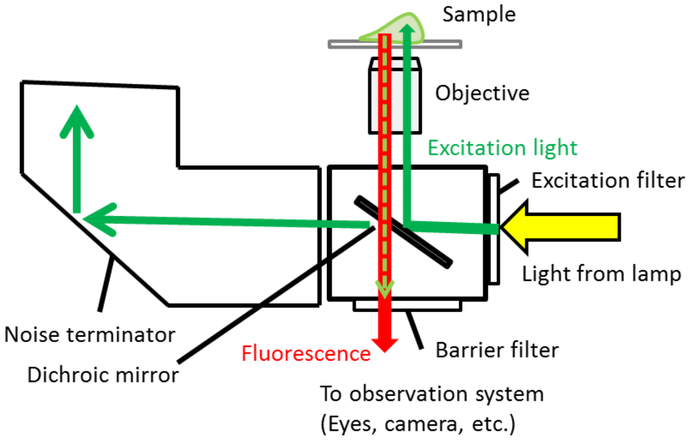

Figure B3. Schematic of epi-fluorescecen microscopy. Epi-fluorescence microscopy refers to microscopes that are designed to observe fluorphores. Optical systems contain a light source for excitation (usually mercury lamps) and a filter block to separate the excitation light from the fluorescence. The excitation light excites the fluorophore emitting the fluorescence which can be seen through the eye-piece or camera.

Multiple laser lines are combined and focused on the sample through the microscope objective lens. The fluorescence photons are emitted into a solid angle of 4π (in all directions in space) and a fraction are collected back through the same objective lens, and split by wavelength through an emission dichroic filter and focused on different detectors for multiple channel (wavelength) imaging. A majority of the excitation light reaching the specimen passes through without interaction and travels away from the objective, and the illuminated area is restricted to that which is observed through the eyepiece. The sample is placed on a stage above the objective lens (for an inverted microscope scheme, as illustrated in image) and coupled to the objective through an index matching medium (oil, water or air). The focus is adjusted manually by controlling the height of the objective relative to the sample. For the epi-fluorescent case, the emitted light is focused to the detector by the same objective that is used for the excitation. Since most of the excitation light is transmitted through the specimen, only reflected excitation light reaches the objective together with the emitted light and this method therefore gives an improved signal to noise ratio. An additional filter between the objective and the detector can filter out the remaining excitation light from fluorescent light. This epi-illuminator has several advantages. The fluorescence microscope objective serves first as a well-corrected condenser and secondly as the image-forming light gatherer. Being one single component, the objective/condenser is always in perfect alignment. Therefore, the epi-fluorescent microscope is great because of its detection sensitivity and high specificity; however it has a few drawbacks. Fluorescently-tagged cells are susceptible to photo-bleaching and photo-toxicity and lacks 3D stack rendering; therefore a more powerful tool is needed to be used to maintain that high specificity and decrease the light intensity.

Laser Scanning Confocal Microscopy (LSCM)

Confocal microscopy has emerged as a powerful imaging technique due to its optical sectioning capability, which enables construction of three-dimensional images. In conventional wide-field microscopy, light is collected from the entire sample volume, including the focal plane as well as all other planes. In confocal microscopy, light is generally collected from the focal plane only. This is achieved by using a pinhole in front of the photomultiplier tube (PMT) detector that blocks the incoming light from all other planes. As depicted in (Fig. A1), the solid line represents light reflected or emitted from the focal plane, while the dashed lines represent light from the out-of-focus planes. The overall contrast and resolution of the image is significantly increased as compared to conventional wide-field microscopy where the image is blurred by out-of-plane light. Consequently, the inherent optical sectioning of the specimen in confocal microscopy allows the assembly of three-dimensional image volumes by stacking together individually acquired planar slices. In an LSCM system, a laser with a single-diffraction limited spot size is used to sequentially scan a selected focal plane. Thus, the image is not formed using a CCD camera as in conventional microscopy but rather the image is a result of the lights interaction with successive areas of the specimen, i.e., the image is recorded pixel by pixel. Therefore, the resulting image is generally superior in resolution to images recorded by conventional optical microscopy as described above. The spatial resolution of a confocal microscope is determined by the three-dimensional point spread function (PSF) since a point emitter (sub-diffraction limit size emitter) maps as a PSF in the image space due to diffraction. In the focal plane, the diffraction pattern is proportional to the first order Bessel function, which can be well approximated by a Gaussian (272). Thus, the obtained confocal image is the convolution of actual intensity distributions using the point spread function as a kernel or an optical impulse response function.

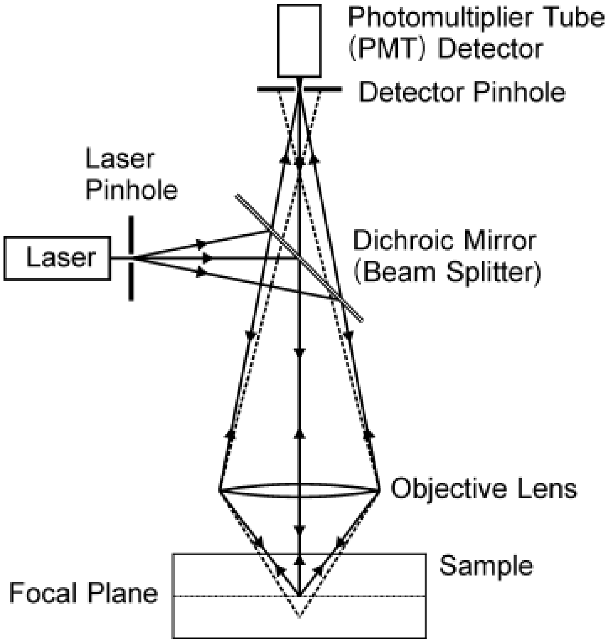

Figure B4 Schematic illustration of the confocal imaging principle. The excitation light is reflected off the dichromatic mirror, through the objective and onto the sample, which then fluoresces. All of the light emitted from the sample, whether in-focus or otherwise, travels back up through the dichroic mirror, but only the in-focus light is able to pass through the detector pinhole (solid lines: focus light and dashed lines: out-of-focus light).

A given point spread function will depend on each imaging situation but is typically a function of the imaging wavelength, λ, refractive index surrounding the lens, n, the numerical aperture of lens, NA, and the image magnification. The numerical aperture of a lens can be expressed as $NA = nsin\theta$, where θ is the half angle of the light cone collected by the microscope lens. Following the derivations given by Stevens et al. (273), a representative expression for the intensity distribution of the point spread function along the lateral and optical imaging axis (u, v) gives

Figure A2 shows a typical line intensity plot of the above point spread function expression both along the lateral and optical imaging axis. The lateral intensity profile of the point spread function in the focal plane, gives the known line profile of the Airy disk, (the interference pattern created from light diffracting through a circular aperture is known as the

Airy disk). Estimates on the typical lateral and axial resolutions can be formulated by using the generally adopted Rayleigh criterion. This criterion states that the ultimate lateral resolution of the optical system is determined by the first zero of the Airy pattern. Therefore, the lateral resolution limit can be estimated as

$$Resolution_{lateral} = 0.61\frac{\lambda}{NA} \text{ , } [B1]$$

The advantage of using a confocal microscope is that the Airy disks are much thinner, owing to its unique pinhole design, and so the distance required to resolve them is smaller. This slightly changes the numerator, leading to a smaller lateral resolution of,

$$Resolution_{lateral} = 0.41\frac{\lambda}{NA} \text{ , } [B2]$$

Clearly, the resolution is still dependent on the wavelength and numerical aperature, but the same degree of contrast can be achieved with a confocal microscope at a smaller separation distance, with comparable wavelength and numerical aperatures as with conventional wide-field fluorescence microscopes. Typical values for the NA of a lens range from 1.0-1.4, depending on whether the lens used is air (n=1.00), water (n=1.33) or oil (n=1.51). As a typical light source used 400-500 nm in wavelength, this means that the diffraction limit is approximately 200 nm for a conventional microscope, which is much larger than the distance between most structures within the cell. Similarly, the axial resolution of a confocal microscope is also improved, due to the tightening of the Airy disks in the axial direction, where the axial resolution can be estimated to be

$$Resolution_{axial} = 1.4\frac{n\lambda}{NA^2} \text{ . } [B3]$$

The axial resolution depends on the refractive index of the specimen n, the wavelength λ, and the square of the numerical aperature (NA). This result is shown graphically in Fig. 2.1.3b by the width of both lateral and axial intensity peaks. Further details describing the confocal principle, including a more rigorously mathematical treatment of confocal imaging and the current applications of confocal microscopy, are well documented and can be found elsewhere (274-276).

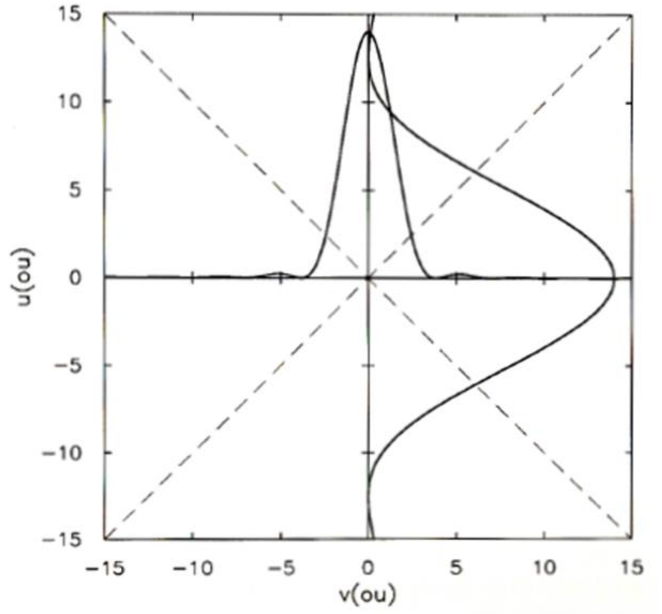

Figure B5 Intensity profile of the PSF. The profiles of the PSF for u = 0 (lateral) and v = 0 (vertical) from Stevens et al. (273). The units of u and v are arbitrary optical units (ou). The peak widths determine the resolution.

Appendix C: Optical Flow Registration Algorithim

Local search implementation

Generally, in tracking algorithms, individually isolated points are tracked and measured within an entire system, but in our case this technique is not robust because we are interested in obtaining the information of the overall substrate motion. This makes it easier because now we are not interested in determining the movement at each pixel within our region-of-interest but only at nodes of a sample m_x x m_y lattice whose coordinates can be expressed as (x_j, y_k) where $j = 1, 2, ..., m_x$ and $k = j -= 1, 2, ..., m_y$. Once this lattice is created, our next task is to determine the displacement of the substrate at each lattice node to within integer precision. To do this, we need to create a window B_0 around each of the points (x_j, y_k) in I_0 and find its corresponding integer pixel coordinates $(u_{jk}{}^{*}, v_{jk}{}^{*})$ in I_1 by testing correlation windows B_1 at various positions (u, v) in I_1 and figuring out where the function $R(x_j, y_k, u, C)$ is a maximum. The maximum value obtained from the cross-correlation at a given lattice site is denoted $R_{jk}{}^{*}$. The best way to find the coordinates $(u_{jk}{}^{*}, v_{jk}{}^{*})$ is to perform an iterative search

Determining Subpixel Resolution

The best interpolative scheme that Marganski et al. (75) establied was the five-point quadratic method, this allowed for much refined estimates of for the coordinates of the maximum $R(x_j, y_k, u, C)$:

$$u_{jk}^{**} = u_{jk}^{*} + \frac{0.5\left[R\left(x_j, y_k, u_{jk}^{*}+1, v_{jk}^{*}, C\right) - R\left(x_j, y_k, u_{jk}^{*}-1, v_{jk}^{*}, C\right)\right]}{2R\left(x_j, y_k, u_{jk}^{*}, v_{jk}^{*}, C\right) - R\left(x_j, y_k, u_{jk}^{*}-1, v_{jk}^{*}, C\right) - R\left(x_j, y_k, u_{jk}^{*}+1, v_{jk}^{*}, C\right)}. \quad [C1]$$

$$v_{jk}^{**} = v_{jk}^{*} + \frac{0.5\left[R\left(x_j, y_k, u_{jk}^{*}, v_{jk}^{*} + 1, C\right) - R\left(x_j, y_k, u_{jk}^{*}, v_{jk}^{*} - 1, C\right)\right]}{2R\left(x_j, y_k, u_{jk}^{*}, v_{jk}^{*}, C\right) - R\left(x_j, y_k, u_{jk}^{*}, v_{jk}^{*} - 1, C\right) - R\left(x_j, y_k, u_{jk}^{*}, v_{jk}^{*} + 1, C\right)}. \quad [C2]$$

When the correlation window undergoes motion with minimal internal deformation then the accuracy of this interpolation is about 0.1 pixels.

The Detection and Correction for the Correspondence Failures

The optical flow algorithm that has just been described above assumes that there exists a unique pixel coordinate (u_{jk}^{**}, v_{jk}^{**}) in I_1 that maximizes the function $R\left(x_j, y_k, u, C\right)$ for any given pixel coordinate in I_0. Typically, this holds true, because inside the correlation window there will be many marker beads and the probability of two correlation windows having the same intensity pattern of a marker bead is minimal, however there is a finite probability that it happens. Usually, this 'correspondence failure' as it's called can happen if the radius of the correlation window is low, which means that the density of the marker beads in the substrate is generally low, the signal-to-noise ratio of the images is poor or the substrate displacements are very large. In addition, the optical flow algorithm fails if there is a feature in I_0 that is absent in I_1, as auto fluorescence of the cell. Such a problem can cause suspicious results by the local search algorithm. Generally, we can avoid these 'correspondence failures' by looking for artefactual displacements and hence either removing or recalculating them. A more sophisticated way of identifying these suspicious displacements are by considering the physical characteristics of the displacements of an elastic substrate. The displacements are generally continuous functions of position, whereas 'correspondence failures' result in discontinuous and random displacements, which can be detected by examining the relationship among the magnitudes of neighbouring displacements. If $\left\|\epsilon_{jk}\right\| > \epsilon_{max}$ (some limiting value), then the pixel coordinates (u_{jk}^{*}, v_{jk}^{*}) in I_1 are considered suspicious. The exact threshold for ϵ_{max} is generally on the order of 1 but can be adjusted by trial and error depending on the nature of the user and problem.

Correcting for Image Registration Artifacts

Sometimes movements of the microscope stage occur in between acquisition recordings of I_1 and I_0, which can cause a systematic displacement of all the fiduciary marker beads by a constant (d_x, d_y). This ‘registration artefact’ needs to be corrected for and it is possible to correct for this artifact as long as the lattice covers a substantial area outside the cell. A simple way of correcting this problem is to define a correlation window far away from the cell in the reference region and to calculate the substrate displacement at this location. This displacement is treated as a registration artefact and is subtracted from the subsequent calculations.

Appendix D: Rheological Methods

Rheology has been accurately defined by Prof. Bingham (277), as the study of the flow and deformation of materials. In flow, elements of the liquids are deforming and adjacent points in the liquids are moving relative to one another. Moreover, there are two principal types of flow with relative movement of adjacent particles of liquids; they are called shear and extensional flows. In shear flows, liquids elements flow over or past each other, while in extensional flow, adjacent elements flow towards or away from each other (Fig. D1). In this thesis, controlled stress rheometry was used, where it enabled us to study shear flow.

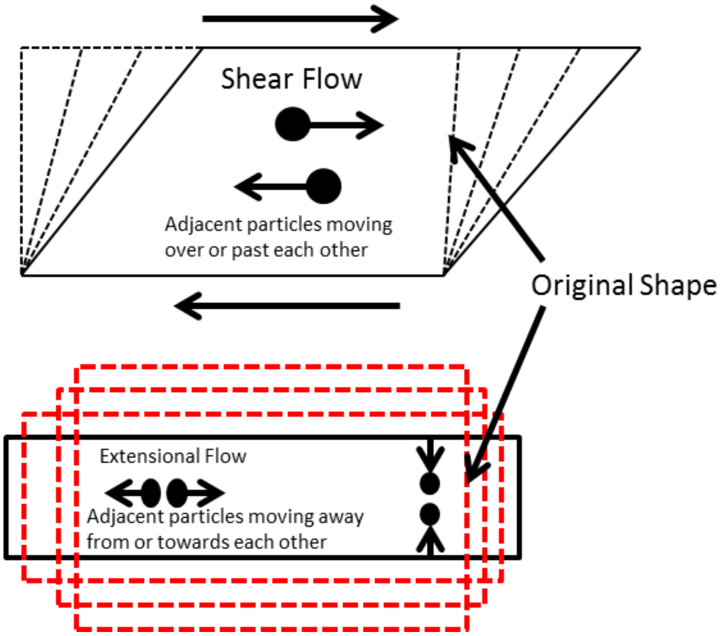

Figure D1: Schematic of the types of flow: shear and extensional flows. The motion of particles in shear and extensional flows.

Basic Rheology

Viscosity is the internal friction of a fluid or its tendency to resist flow. Liquids are made to flow by imparting a velocity by applying a force. For a given velocity the resulting force increases when the viscosity is increased. In Fig. D2, the shear flow is visualized as the movement of hypothetical layers of fluid sliding over each other. The material between the two plates is separated by a distance h. If the top plate is subjected to a shear stress (σ) triggering the movement of the top plate as the bottom plate remains stationary, the material touching the top plate will move a distance Δx in the same direction due to frictional forces.

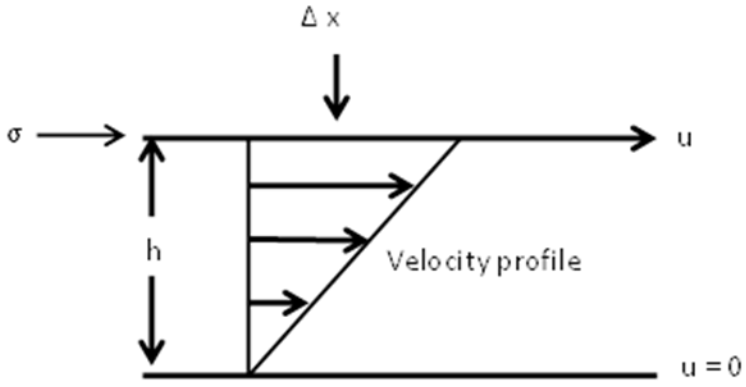

Figure D2: Shear flow. A material between two plates seperated by a distance h. If the top plate is subject to a stress σ, both the plate and material touching the top of the plate will move a distance covered by the Δx.

Moreover, the strain (γ) of the sample is defined as,

$$\gamma = \frac{\Delta x}{h} \; [D1]$$

While the strain rate ($\dot{\gamma}$) is

$$\dot{\gamma} = \frac{d\gamma}{dt} \; [D2]$$

If the material is a perfectly Newtonian fluid, we may say that the stress imparted on the material is

$$\sigma = \eta \cdot \dot{\gamma} \; [D3]$$

where η is said to be the viscosity of the liquid. If the material is a linear elastic solid, then the stress is

$$\sigma = G \cdot \gamma \; [D4]$$

where G is the shear modulus of the material. Interestingly, some materials cannot be definitely called a solid or liquid because they display both qualities and hence exist in a phase. These types of materials are said to be viscoelastic.

All deformed materials possess what is called a strain history. This term describes how the deformation of a material at time *t* is dependent upon all previous deformations it has undergone. Keeping this in mind, the total stress placed upon a material may be calculated. When a material is subject to different kinds of individual step strains, $\delta\gamma_i$, over a period of time t_i, the overall stress on the material may be defined as a linear superposition by

$$\sigma(t) = \sum_i G(\,t - t_i)\,\delta\gamma_i = \sum_i G(t - t_i)\dot{\gamma}_i\,\delta t_i \;\; [D5]$$

Where γ_i is the strain rate, $G(t - t_i)$ is the relaxation modulus of the material and t_i is the time the *i*-th event takes place. This relationship can be changed from a discrete form to an integral form in order to take into account all strain deformations of the material over a time $t^{'}$ to determine the stress of the material ($\sigma(t)$) at time *t*,

$$\sigma\,(t) = \int_{-\infty}^{t} G(t - t')\dot{\gamma}(t')dt' \; [D6]$$

Complex Rheology: Oscillatory Shear Flow

In small amplitude oscillatory shear experiments, a sinusoidal oscillating stress or strain with a frequency ω is applied to the material, and the phase difference between the oscillating stress and strain, as well as the amplitude ratio is measured.

If the applied stress varies as a function of time according to $\sigma = \sigma_0 sin\omega t$ where ω is the angular frequency (2π times the frequency in Hz), the strain for an elastic material obeying

Hooke's law would vary in a similar manner as $\gamma = \gamma_0 sin\omega t$. For a perfect, Newtonian fluid, the strain is therefore out of phase with the stress by π/2. However, for a viscoelastic material the strain lags somewhat behind the stress and the result is that when a sinusoidal stress is applied to the sample, the strain varies in a sinusoidal manner, but is out-of-phase with the applied stress. The variation of the stress and strain with time, can then be written as

$$\gamma = \gamma_0 sin\omega t \ [D7] \qquad \text{and} \qquad \sigma = \sigma_0 \sin(\omega t + \delta) \ [D8]$$

Where δ is the phase angle. Moreover, the equation for stress can be expanded and rewritten as

$$\sigma = \sigma_0 \sin \omega t cos\delta + \sigma_0 \cos \omega t sin\delta \ [D9]$$

The stress can therefore be considered as being resolved into two components; one of $\sigma_0 \cos \delta$ which is in phase with strain and another $\sigma_0 sin\delta$ which is π/2 out of phase with the strain. Hence, it is possible to define two dynamic moduli: G, ' which is in phase with the strain and G'', which is π/2 out-of-phase with the strain. Since $G' = (^{\sigma_0}/_{\gamma_0})cos\delta$ and $G'' = (^{\sigma_0}/_{\gamma_0})sin\delta$, the equation for the stress can then be expressed as

$$\sigma = G'\gamma_0 sin\omega t + G''\gamma_0 cos\omega t \ [D10]$$

G' is called the storage modulus and it expresses the magnitude of the energy that is stored in the material and recovered per cycle of deformation. *G''* is called the loss or viscous modulus and it measured the energy lost per cycle through viscous dissipation.

The phase angle δ is then given by:

$$tan\delta = {}^{G''}/_{G'} \ [D11]$$

A complex notation is often favoured for the representation of the dynamic properties of viscoelastic materials. The stress and strain are given as:

$$\gamma = \gamma_0 e^{i\omega t} \ [D12] \qquad \text{and} \qquad \sigma = \sigma_0 \mathrm{e}^{(i\omega t + \delta)} \ [D13]$$

The overall complex modulus $G^* = {}^{\sigma}/_{\gamma}$ is given by

$$G^* = \frac{\sigma_0}{\gamma_0} e^{i\delta} = \frac{\sigma_0}{\gamma_0}(cos\delta + isin\delta) \; [D14]$$

It then follows that

$$G^* = G' + iG'' \; [D15]$$

Additional frequency dependent material functions in addition to the complex modulus (G^*) are the complex viscosity (η^*), dynamic viscosity ($\eta^{'}$), out-of-phase component of the complex viscosity ($\eta^{''}$),

$$|G^*| = \sqrt{G'^2 + G''^2} \; [D16]$$

$$\eta^* = \frac{G^*}{\omega} = \sqrt{\eta'^2 + \eta''^2} \; [D17]$$

$$\eta' = \frac{G'}{\omega} \text{ and } \eta'' = \frac{G''}{\omega} \; [D18]$$

Rheometry

To experimentally investigate the viscoelastic properties of a material, rheometry is commonly used. For typical rheometry experiments, this involves a stress or strain applied to the material using a specific geometry in order to measure the response of the material.

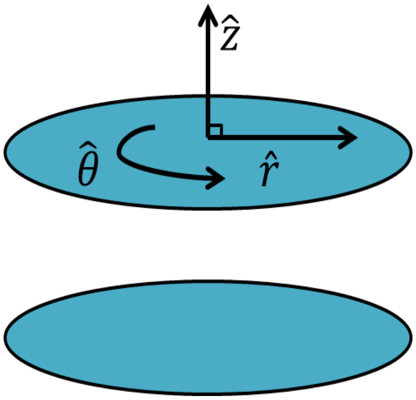

Figure D3: A plate-plate geometry. A diagram of the plate-plate geometry that can be used to apply a stress in the $\hat{\theta}$ −direction.

This system allows for either the strain to be measured as a function of stress or the other way around. Moreover, the measurements obtained makes it possible to calculate the storage and loss moduli ($G^{'}$ and $G^{''}$ respectively as seen in the next section) of the material. To determine the complex modulus, the material is subjected to an oscillatory shear stress through plate-plate geometry as shown in Fig. D3. The material of interest is typically positioned in between the two plates and by moving the top plate in the $\hat{\theta}$ $-$direction while keeping the bottom plate stationary, a shear stress is applied.

Generally, tensors must be used to express stresses and strains in order to consider all possible deformations in a three-dimensional object. We initially define the stress tensor σ_{ij} as

$$\sigma_{ij} = \begin{vmatrix} \sigma_{xx} & \sigma_{xy} & \sigma_{xz} \\ \sigma_{yx} & \sigma_{yy} & \sigma_{yz} \\ \sigma_{zx} & \sigma_{zy} & \sigma_{zz} \end{vmatrix} \; [D19]$$

Here each component of σ_{ij} represents a force applied to the surface in the *i*-direction with a normal in the *j*-direction. Essentially, the stress tensors are symmetric if $\sigma_{ij} = \sigma_{ji}$, which is referred to as the Cauchy rule. If we consider the geometry of fig. D1, where a force is imparted in the $\hat{\theta}$ $-$direction, then the stress tensor (in cylindrical coordinates) can be simplified to

$$\sigma_{ij} = \begin{vmatrix} 0 & 0 & 0 \\ 0 & 0 & \sigma_{\theta z} \\ 0 & \sigma_{z\theta} & 0 \end{vmatrix} \; [D20]$$

where $\sigma_{\theta z}$ is the stress component in $\hat{\theta} -$ direction which is being imparted to the surface in in $\hat{z} -$ normal.

The ‘magnitude’ of the tensor can be determined by using the double dot product. This particular technique enables us to decompose a matrix into two multiplying vectors, where they are then scalar multiplied to create a scalar value. Therefore, for an n x n matrix $\boldsymbol{A} = \vec{b}\vec{c}$, where $\vec{b}$ is an nx1 matrix and $\vec{c}$ is an 1xn matrix, the double dot product is then defined as

$$\boldsymbol{A}:\boldsymbol{A} = \left(\vec{b}\vec{c}\right):\left(\vec{b}\vec{c}\right) = \left(\vec{b}\cdot\vec{c}\right)\left(\vec{b}\cdot\vec{c}\right) = \left(\vec{b}\cdot\vec{c}\right)^2 \; [D21]$$

Therefore, the magnitude of a tensor is then defined as,

$$|\boldsymbol{A}| = \sqrt{\frac{1}{2}\boldsymbol{A}:\boldsymbol{A}} \; [D22]$$

From the above equation [2.56] the magnitude of the stress tensor from equation [D20] can be calculated, which will give us the following relation,

$$\left|\boldsymbol{\sigma}_{ij}\right| = \sqrt{\frac{1}{2}\boldsymbol{\sigma}_{ij}:\boldsymbol{\sigma}_{ij}} = \sigma_{\theta z}. \; [D23]$$

In addition, the strain can also be presented as a three-dimensional tensor γ_{ij}, which we can define in cylindrical coordinatesas

$$\gamma_{ij} = \begin{vmatrix} \gamma_{rr} & \gamma_{r\theta} & \gamma_{rz} \\ \gamma_{\theta r} & \gamma_{\theta\theta} & \gamma_{\theta z} \\ \gamma_{zr} & \gamma_{z\theta} & \gamma_{zz} \end{vmatrix} \; [D24]$$

where the component $\gamma_{ij}$is the deformation in the j-direction of the surface with a normal in i-direction. In our case, the stress is only occurring at the top plate in the $\hat{\theta} -$ direction, therefore the only deformation that occurs must also be in the $\hat{\theta} -$ direction on the surface with normal $\hat{z}$ or $\gamma_{\theta z}$.Using the equations [D21] and [D23] on [D24], the final magnitude of the strain tensor then becomes

$$\left|\boldsymbol{\gamma}_{ij}\right| = \gamma_{\theta z} \; [D25]$$

From Subsection 2.3.2 and equation [2.43], the stress and strain components can be rewritten as,

$$\sigma_{\theta z} = \gamma_{\theta z}[G' \sin(\omega t) + G'' \cos(\omega t)] \; [D26]$$

where an oscillatory stress is assumed. Equation [D26 implies that by using the plate-plate geometry, we may arrive to a simple relationship between stress and strain on a material, allowing both the storage and loss moduli to be measured.

In reality, it is difficult for a rheometer to measure the exact stress imparted to a material in a plate-plate geometry as it is a function of radius. Instead, the torque T_{tor}, is measured due to its relationship to the applied stress and because it is quite simple to measure. Considering circular disks of radius *R*, the relation becomes

$$T_{tor} = 2\pi \int_0^R r^3 \sigma(r) dr = 2\pi \int_0^R r^3 G^* \gamma dr \ [D27]$$

where *σ(r)* is the applied stress on the material with radius *r*. The strain of the material for this particular geometry at distance *r* from the middle with an angular displacement *θ* is

$$\gamma = \frac{\theta_r}{h} \ [D28]$$

where the distance between the two plates is *h*. The maximum strain possible on the material will take place at the maximum disk radius *R*, provided that $\gamma_R = \frac{R}{r}\gamma$ and that its derivative $d\gamma_R = \frac{R}{dr} d\gamma$. Now by replacing all these factors in equation [D26] we get the following,

$$T_{tor} = 2\pi \int_0^{\gamma_R} (\frac{R}{\gamma_R})^3 G^* \gamma^3 d\gamma \ [D29]$$

Equation [D29] can be simplified once applying Leibniz' rule and differentiating with respect to γ_R, which gives

$$G^* = \frac{T_{tor}}{2\pi R^3 \gamma_R}\left[3 + \frac{dlnT_{tor}}{dln\gamma_R}\right] \ [D30]$$

Here, the complex modulus for viscoelastic materials is a function of both strain and angular frequency. At low strain amplitudes, the complex modulus no longer depends on the strain. Moreover, the range of strain at which the complex modulus is independent of strain is called the linear viscoelastic region. At these strains the $\frac{dlnT_{tor}}{dln\gamma_R}$ term in the equation [D30] converges to 1 as the torque becomes independent of strain. This leads to the reduction of equation [D30], where the complex modulus now becomes

$$G^{*} = \frac{2T_{tor}}{\pi R^{3}\gamma_{R}} = \frac{2T_{tor}h}{\pi\theta R^{4}}\ [D31]$$

Where only the amount of strain at radius R must be measured for an applied torque, T_{tor}, to determine G^{*}. Since $G' = (^{\sigma_0}/_{\gamma_0})cos\delta$ and $G'' = (^{\sigma_0}/_{\gamma_0})sin\delta$ then the given expressions for the storage and loss moduli become,

$$G' = \frac{2T_{tor}h}{\pi\theta R^{4}}cos\delta\ [D32]$$

$$G'' = \frac{2T_{tor}h}{\pi\theta R^{4}}sin\delta\ [D33]$$

Where δ is the phase difference between the stress and strain response.

Controlled Stress Rheometry

Controlled stress rheometers measure the strain as a function of stress (278). The most common way of controlling the applied stress is simply by controlling the torque applied to a sample via what is called a drag cup motor, which is described as follows (278, 279). For our particular geometry: the plate-plate geometry, the top plate is attached to a long, cylindrical shaft while the bottom plate is held in place. The top part of the cylindrical shaft is attached to an air bearing, which supports either a copper or aluminum cup. The torque is applied to the system by generating a rotating magnetic field around the cup, which will attempt to follow the created field (278, 279). The torque that was created is proportional to the square of the voltage (278). A of variety of methods including an optical lever, capacitance transducers, or optical encoders (278) can be used to measure the strain. The latter system is the most commonly employed technique. In that case, a light source is used, where it is shined through a disc composed of many transparent and opaque areas, which will allow for the precise measurement of the angular position, θ. For oscillating torques, the phase difference, δ may be calculated by determining the time difference between the oscillating maxima of θ and the torque.

It is important to precisely determine the instrument inertia when using the controlled stress rheometer. The induced torque on the drag cup is countered by the air bearing friction, the rotor inertia and the reluctance torque in addition to the viscosity of the sample. It is important to point that the for low viscosity samples the largest effect comes from the rotor inertia for samples (278). The torque which is applied, T_{app} differs from the actual torque which is experienced by the sample, T_{exp} through the following relation

$$T_{exp} = T_{app} - I \cdot \ddot{\theta} \; [D34]$$

where I is the motor inertia, and $\ddot{\theta}$ is the second derivative of the angular displacement with respect to time (280). We can correct for the torque simply by subtracting the inertial term, which can be done with the software. In order to determine the motor inertia, a standardized test using air as the sample medium can be used. In that case the motor inertia can be deterimined by subtracting the calculated torque experienced by the air, which is determined by the strain from the torque applied to the air at a certain angular acceleration.

To control strain on a sample using a controlled stress rheometer, typically the software will attempt several low torque (and therefore stress) values and will measure the strain. An algorithm will allow the rheometer to approach the required stress in order to obtain the strain. This is achieved either by reducing the torque by a small interval if the measured strain is too high, or increasing the torque by a small interval if it is too low. Therefore, before a measurement of the moduli may be considered, a small amount of time must be spent by the controlled stress rheometer as it approaches the desired strain.

Appendix E: Statistical Analysis

Statistics is a field of mathematics that involves data analysis. Statistical methods and equations can be applied to a data set in order to analyze and interpret results, explain variations in the data, or predict future data. However, it is important to note that presenting results of biological systems in their native environments differs immensely than an arbitrarily designed system or a computational simulation. This section will explain the various methods used in explaining the variations in results in this thesis and also clarify as to why the presentation of the results through the standard error of the mean (SEM) is the primary convention used throughout the experimental fields in biology and the related sciences. Therefore, throughout this thesis all results are presented as the average mean ± Standard Error of the Mean (SEM) unless specified otherwise.

Generally, when working with live cells in their native environments, the sample number is typically small due to several constraints that may affect the natural environment of cells, such as a change in pH, over-exposure of cells to the laser beams leading to photo-bleaching and photo-toxic effects and most importantly time constraints. Therefore, the practical nature of working with cells limits the sample number and hence imposes less stringent statistical methods in statistically interpreting the results. In addition, because of such difficulties it is very difficult to take into account any of the systematic errors since we are randomly choosing the cells from the petri dish. Given the nature of the experiments conducted for the purposes of this thesis, it was not possible to perform measurements on each member of the population (e.g. obtaining the traction forces, cell elasticity, FA area of all the cells in dish); instead, I took representative samples (i.e. indicated throughout the thesis as an n-value) and analyzed only the data produced from these samples. This was done on multiple dishes and not just one petri dish; this ensured the reproducibility of our data collection and unbiased selection of our samples. As is the case in general, employing proper statistical techniques enables us to use sample data in order to make broader conclusions that apply to the population about any trends observed.

The Sample Mean

The mean, which is also known as the average is obtained by dividing the sum of observed values by the number of observations, N. The formula for the mean is given by

$$\bar{X} = \sum_{i=1}^{N} \frac{X_i}{N}, \ [E1]$$

where X_i are the observed values and N is the number of observations.

The Standard Deviation (SD)

The standard deviation (SD) gives us an idea of how close the entire set of data is to the average value ($\bar{X}$). Data sets with a small SD have tightly grouped, precise data. Data sets with large SDs have data spread out over a wide range of values. The formula for standard deviation is given

$$SD = \sqrt{\frac{\sum_{i=1}^{N}(X_i - \bar{X})^2}{N}}, \qquad [E2]$$

The SD is a measure of how closely the individual data points vary around the mean (281). When we measure the SD of a sample we are using this index as an estimate of the variability of the population from which the sample was drawn. If the data is a normal distribution, where about 95% of the individual observations will have values within 2 SDs of the mean, the other 5% will be equally scattered above and below these limits (282).

The Standard Error of the Mean (SEM)

When we calculate the mean of a sample we are usually interested not in the mean of this particular sample but in the mean for the individuals of this type of sample-in statistical terms, of the population from which the sample occurs. We usually collect data in order to generalise from them and so we use the sample mean as an estimate of the mean for the whole population. Now the sample mean will vary from sample to sample; the way this variation occurs is described by the ‘sampling distribution’ of the mean. We can estimate how much sample means will vary from the standard deviation of this sampling distribution, which we call the standard error of mean (SEM) (281).

The SEM depends on both the SD and the sample size, N by the following relation:

$$SE = \frac{SD}{\sqrt{N}}. \; [E3]$$

The SE becomes smaller as the sample size increases, as the extent of chance variation is reduced. By contrast the SD will not decrease as we increase the size of our sample. The SE is most useful as a means of calculating confidence interval.

Therefore, if we want to state how widely scattered some measurements are, we use the SD. If we wish to indicate the uncertainty around the estimate of the mean measurement, we quote the SEM.

Statistical Hypothesis Testing

Statistical hypothesis tests are concerned with using a sample statistic from a small subset (sample) of the total population to estimate the long run probability that a population parameter is equal to a particular value, often zero (283).

In statistical hypothesis testing, the P-value is the probability of obtaining a value of the test statistic as extreme as or more extreme than that observed by chance alone, if the null hypothesis is true. Moreover, the null hypothesis represents a theory that has been put forward, whether because it is believed to be true or because it is to be the default position for an argument, but has not yet been proved. The null hypothesis is given special consideration as it relates to the statement being tested, whereas the alternative hypothesis relates to the statement to be accepted if or when the null hypothesis is rejected. Therefore, the p-value is equal to the significance level of the test for which we would only just reject the null hypothesis. The P-value is compared with the actual significance level of our test and if it is smaller, the result is significant. That is if the null hypothesis were to be rejected at the 5% significance level, this would be reported as ‘P < 0.05’. Small P-values suggest that the null hypothesis is unlikely to be true. The smaller it is the more convincing is the rejection of the null hypothesis. Hence, it indicates the strength of evidence for rejecting the null hypothesis.